$ZnGeP_2$ heterocontact with layered III-VI semiconductors

V. Yu. Rud' and Yu. V. Rud'

St. Petersburg State Technical University, A. F. Ioffe Physicotechnical Institute, Russian Academy of Sciences, St. Petersburg

(Submitted November 27, 1996)
Pis'ma Zh. Tekh. Fiz. **23**, 1–5 (June 12, 1997)

The photoelectric properties of heterojunctions fabricated by clamping wafers of ternary p-$ZnGeP_2$ and InSe and GaSe layered semiconductors onto an optical contact have been studied for the first time and results are reported. The photosensitivity in these structures is greatest when they are illuminated from the side with the $ZnGeP_2$ wafer, and reaches 150 V/W at $T = 300$ K. In InSe/$ZnGeP_2$ heterostructures, a window effect is observed in the range 1.2–2 eV, whereas for GaSe/$ZnGeP_2$ structures, the photovoltaic effect has a maximum near 2 eV because of the proximity of the band gaps in the contacting semiconductors. © *1997 American Institute of Physics.* [S1063-7850(97)00106-7]

The method of clamping onto a direct optical contact is used as an effective method of fabricating energy barriers on semiconductors that retain their conductivity type, which now includes bulk single crystals of the ternary compound $ZnGeP_2$ (Ref. 1). In the present paper, we report the fabrication of the first photosensitive heterocontacts of this potentially useful semiconductor for highly efficient, nonlinear optical radiation converters[2,3] using layered crystals of various direct-gap III–VI semiconductor compounds (InSe, $E_g = 1.2$ eV and GaSe, $E_g = 2.0$ eV at $T = 300$ K (Ref. 4)). For $ZnGeP_2$ the chosen method of forming the energy barrier is also interesting because the ternary phosphide needs no treatment, and for this reason conditions do not arise for the formation of additional lattice point defects due to changes in the composition of the compound.

Single-crystal wafers of p-type $ZnGeP_2$ with average dimensions of $5 \times 5 \times 0.5$ mm were used to fabricate the heterojunctions. The single crystals were grown by directional crystallization from stoichiometric and nonstoichiometric melts.[1] The mirror planes were prepared by mechanical treatment followed by chemical treatment of the $ZnGeP_2$ surface. The free hole concentration in these samples varied in the range 10^9–10^{12} cm^{-3} at $T = 300$ K.

No surface treatment of the layered n-type InSe and GaSe semiconductors was required to obtain perfect planes, and wafers of these compounds, having average dimensions of $5 \times 5 \times 0.5$ mm, were prepared by splitting the ingot along the cleavage plane. The free electron concentration in these InSe and GaSe crystals was approximately 10^{14} cm^{-3} at $T = 300$ K. Single crystals of the layered semiconductors were grown by directional crystallization of nearly stoichiometric phases of the melts without intentionally introducing any additional chemical impurities.

The heterojunctions were fabricated by bringing into contact the ''pure'' surfaces prepared as above and then clamping them together mechanically in a special holder, to ensure that the heterocontact remains stable with time.

As a result of various investigations, it was established that when the n-InSe/p-$ZnGeP_2$ and n-GaSe/p-$ZnGeP_2$ heterocontacts were illuminated by full-spectrum radiation on the side with the narrow-gap component (InSe and GaSe) and on the $ZnGeP_2$ side, they exhibit a photovoltaic effect with the positive polarity photovoltage corresponding to p-$ZnGeP_2$. When the energy of the incident photons was varied over the entire range of photosensitivity of these heterojunctions, no reversal of the photovoltage polarity was observed, and the direction of rectification matched the polarity of the photovoltage. In all these heterojunctions, the photosensitivity is greatest when the structures are illuminated on the $ZnGeP_2$ side, and for the best structures reaches 100–150 V/W at $T = 300$ K. It should also be stressed that the photosensitivity of these $ZnGeP_2$ heterojunctions fabricated by clamping onto an optical contact does not exhibit any degradation.

Figure 1 shows typical spectral dependences of the relative photoconversion quantum efficiency, defined as the ratio of the short-circuit photocurrent to the number of incident photons, for heterojunctions made up of the same p-$ZnGeP_2$ wafer but different layered semiconductors: InSe or GaSe. Both heterojunctions are illuminated by unpolarized radiation on the side with the $ZnGeP_2$ wafer.

For the InSe/$ZnGeP_2$ heterojunction, the long-wavelength exponential edge has a slope $s = 20$–50 eV^{-1} for different heterocontacts, which may reflect the influence of the quality on the separation of the photogenerated pairs. The energy position of the step at the end of the long-wavelength increase in the photosensitivity corresponds to the band gap of InSe (Ref. 4). For this reason, the long-wavelength edge of the photosensitivity in these heterojunctions will be associated with interband absorption in the narrow-gap component of the structures. It can be seen from Fig. 1 (curve *1*) that in the range between the band gaps of InSe and $ZnGeP_2$ (Refs. 1 and 4), the photosensitivity remains high, which indicates the appearance of a window effect[5] in these InSe/$ZnGeP_2$ heterojunctions fabricated by clamping onto an optical contact. The beginning of the short-wavelength descending section of η for $\hbar\omega > 2$ eV corresponds to the onset of interband absorption in $ZnGeP_2$ and is a consequence of the optical absorption of radiation in the bulk of the wide-gap component of the heterojunction.

When InSe is replaced by the wider-gap semiconductor GaSe, the long-wavelength exponential edge of η is shifted

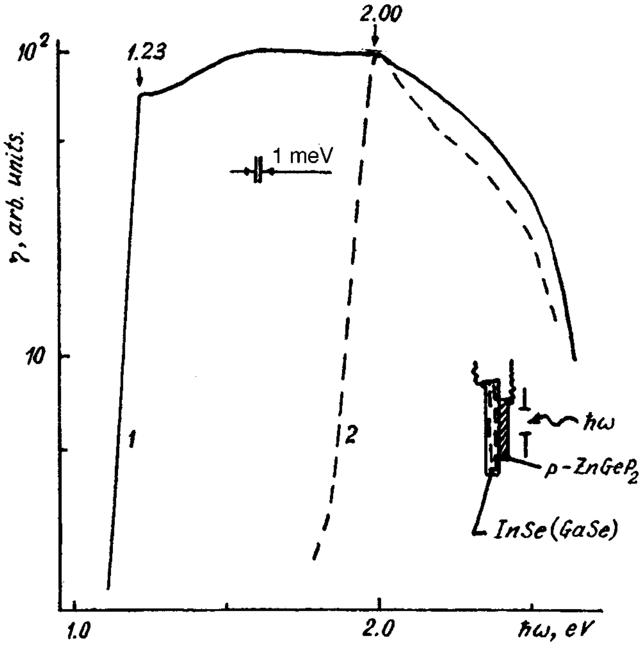

FIG. 1. Spectral dependences of the relative photoconversion quantum efficiency in *n*-InSe/*p*-$ZnGeP_2$ (*1*) and *n*-GaSe/*p*-$ZnGeP_2$ heterojunctions (*2*) at $T = 300$ K (the inset shows the illumination of the heterojunction).

toward shorter wavelengths in accordance with the increase in Eg (Ref. 4). The slope of the long-wavelength photosensitivity edge in these heterojunctions varies in the range 30–40 eV^{-1}, which corresponds to the direct interband transitions in GaSe. The maximum photosensitivity of these heterojunctions is observed near $\hbar\omega = 2$ eV, which is consistent with the band gap. For GaSe/$ZnGeP_2$ (curve *2*), this behavior should be attributed to increased optical losses of radiation in the bulk of the $ZnGeP_2$ with increasing $\hbar\omega > 2$ eV when the structure is illuminated on the $ZnGeP_2$ side.

To sum up, these InSe/$ZnGeP_2$ and GaSe/$ZnGeP_2$ heterojunctions fabricated by the straight-forward method of clamping onto an optical contact can be used as photodetectors for natural radiation in the 1.2–2 eV spectral range. The energy position of the long-wavelength exponential edge of the photosensitivity in these detectors can be shifted smoothly in this range by controlling the atomic composition of the layered semiconductor, by virtue of the continuous series of solid solutions in the InSe–GaSe system. It should also be noted that the high photosensitivity of InSe/$ZnGeP_2$ heterojunctions in the 1.2–2 eV range can also be used for rapid quality control of crystals of the ternary compound, which is a critical factor for achieving highly efficient conversion of radiation in nonlinear optical elements utilizing these structures.[2,3]

This work was partially supported by the University of Cincinnati, USA.

[1] Yu. V. Rud', Fiz. Tekh. Poluprovodn. **28**, 1105 (1994) [Semiconductors **28**, 633 (1994)].

[2] N. P. Barnes, Int. J. Nonlinear Optical Phys. **1**, 639 (1991).

[3] P. A. Budni, P. G. Schunemann, M. G. Knights, T. M. Pollak, and E. P. Chicklis, *OSA Proceedings on Advanced Solid State Lasers*, edited by L. Chase and A. A. Pinto (Optical Society of America, Washington, DC, 1992). Vol. 13. p. 380.

[4] *Handbook of Physicochemical Properties of Semiconductors* [in Russian], Nauka, Moscow (1978).

[5] B. L. Sharma and R. K. Purohit, *Semiconductor Heterojunctions* (Pergamon Press, Oxford, 1974) [Russ. transl., Sov. Radio, Moscow, 1979].

Translated by R. M. Durham

Spatial anisotropy of anomalous acoustic damping and thermal conductivity in La_2MCuO_4 high-temperature superconductors

S. V. Gushchin

Institute of Nuclear Physics, Uzbek Academy of Sciences, Tashkent

(Submitted December 26, 1996)
Pis'ma Zh. Tekh. Fiz. **23**, 6–9 (June 12, 1997)

Low-temperature thermal properties of superconductors have been studied. It is shown that the symmetry group influences the thermal conductivity and the anomalous acoustic damping, and the directions of maximum thermal conductivity and acoustic damping factor are indicated. For crystals, the general conclusion is reached that the absence of a center of symmetry is a necessary condition for the existence of these properties. *© 1997 American Institute of Physics.* [S1063-7850(97)00206-1]

Anomalous temperature dependences of the low-temperature specific heat, thermal conductivity, and acoustic damping,[1] have been observed in high-temperature superconductors such as La_2MCuO_4 and $LnBa_2Cu_3O_7$. A model of small-radius polarons, having a double-well interaction potential, was proposed in Ref. 2 to explain these properties. The theory of such potentials, developed in Ref. 3 for the low-temperature properties of glasses and generalized to high temperatures in Ref. 4, provides an explanation of the anomalous thermal properties. A configuration containing a copper atom at the center of a square of oxygen atoms, symmetry group C_{4v}, and a transition to a double-well potential with the lower symmetry group C_{2v} was investigated in Ref. 2. In a previous study,[5] the authors analyzed the conditions for the existence of a double-well potential in La_2MCuO_4 for a configuration formed by a quadrilateral of oxygen atoms without a copper atom at the center, and the corresponding reduction in symmetry from D_{4h} to D_{2h}. These results explain the anomalous behavior of the specific heat — a structurally independent characteristic. The same cannot be said of the anomalous thermal conductivity and acoustic damping. In the present paper, the spatial characteristics of the thermal conductivity and the acoustic damping are investigated.

It was shown in Refs. 3 and 4 that the low-temperature properties associated with phonon transport, such as the propagation of sound and heat conduction, depend on the asymmetry of the double-well potential. This situation arises when the interaction potential contains a term with cubic anharmonicity. The ensuing asymmetry determines the deformation potential at which phonon damping occurs. In Ref. 6, the deformation potential is defined as

$$\gamma = 1/2(\partial\Delta/\partial\varepsilon + \partial\Delta_0/\partial\varepsilon), \tag{1}$$

where ε is the deformation, Δ is the asymmetry of the double-well potential, and Δ_0 is the difference between the levels as a result of tunnel splitting. Then the second term is much smaller than the first and the deformation potential is determined only by the first term in the equation.

For glasses a similar potential with cubic anharmonicity occurs as a result of fluctuations, and the cubic term of the potential is symmetric because there is no preferred direction in glasses. For crystals this anharmonicity can only arise in noncentrosymmetric systems.

For the La_2MCuO_4 high-temperature superconductor under study, this condition is satisfied by the superconducting plane formed by a square of oxygen atoms with a copper atom at the center. The conditions for the appearance of asymmetry in the double-well potential can easily be determined. Let us consider the anharmonic potential for C_{2v} symmetry

$$K_{00}Q_0^2 + K_{11}Q_1^2 + K_{000}Q_0^3 + K_{011}Q_0Q_1^2 + K_{111}Q_1^3 + K_{0000}Q_0^4 + K_{0011}Q_0^2Q_1^2 + K_{1111}Q_1^4, \tag{2}$$

using the notation from Ref. 5. The form of the potential is determined by the existence of only two normal vibrations for C_{2v} symmetry: Q_0 — completely symmetric and Q_1 — incompletely symmetric. Minimizing with respect to Q_0 and making the transformation

$$X = Q_0 + K_{000}(4K_{0000}),^{-1} \tag{3}$$

we can obtain a solution of the cubic equation:

$$X_{1,2} = K^{1/3}(2 \pm 1/2(d - 3/4K^{2/3})), \tag{4}$$

where

$$d = \{3/16(K_{000}/K_{0000})^2 - 1/2(K_{00}/K_{0000}) - 1/2(K_{011}Q_1^2/K_{0000})\}, \tag{5}$$

$$k = \{1/32(K_{000}/K_{0000})^3 + 1/2(K_{00}K_{000}/K_{0000}^2) + K_{000}K_{0011}Q_1^2/K_{0000}^2 + K_{0011}Q_1^2/K_{0000}\} \tag{6}$$

for the condition

$$dk = 0. \tag{7}$$

It can be seen from the solution (4) that in this case the potential has nonzero asymmetry. For the configuration considered in Ref. 5, corresponding to a layer joining superconducting planes, the deformation potential is determined by the substantially lower tunnel splitting or by including the highest anharmonic terms of the interaction potential.

In this context the following conclusion can be drawn: the coefficient of relaxation absorption of sound, which is uniquely determined in Refs. 3 and 4:

$$l_{\mathrm{rel}} = \vartheta^{-1} \sum D^2 (\rho v^3 4kT \cosh(E/kT))^{-1} \omega^2 \tau (1+\omega^2\tau^2)^{-1}, \tag{8}$$

in the notation of Ref. 4, with $D = 2\Delta\gamma/E$, depends strongly on the direction of propagation. Sixth-order anharmonic terms must be taken into account to allow for damping in the layer between superconducting planes.

The low-temperature thermal conductivity can be analyzed similarly. It follows from Refs. 7 and 8 that this thermal conductivity is determined by

$$\begin{aligned}\varkappa(T) &= (24\pi)^{-1} (\rho\eta^{1/2}) (h\omega G_1 b^2)^{-1} (v_l/d_l^2 + 2v_t/d_t^2) \\ &\quad \times (Tt\ln(w/T))^2 [1 + 9G_{11}/b^2 G_T (\ln n(w/T))^2]^{-1},\end{aligned} \tag{9}$$

where $d = \lll \gamma \ggg$ is the ensemble average over two-level systems; i.e., a large anisotropy is again observed in the propagation of heat along the superconducting plane and along the layers joining these planes.

To sum up, this investigation has shown for the first time that the low-temperature thermal conductivity and acoustic damping observed in high-temperature La_2MCuO_4 superconductors exhibit spatial anisotropy. These properties depend on the profile of the double-well potential, and their direction of propagation is determined by the symmetry of the propagation plane. The generalization can thus be made that in crystals possessing anomalous thermal properties a necessary condition for the existence of anomalous thermal conductivity and acoustic damping is the lack of a center of symmetry in the propagation plane. This is a necessary but not sufficient condition, since additional conditions of asymmetry of the double-well potential exist in this case, such as condition (7). It should be noted that this conclusion does not apply to the anomalous temperature dependence of the specific heat at low temperatures.

These results may be used to study the thermal and acoustic properties of new superconductors.

[1] V. B. Lazarev, K. S. Gavrichev, V. E. Gorbunov, Ya. Kh. Grinberg, and P. Z. Slutskiĭ, Zh. Neorg. Khim. **35**, 3 (1990).

[2] K. H. Szymzak, Z. Ganzel, and A. Wittin, Int. J. Mod. Phys. **4**, 1369 (1990).

[3] G. W. Anderson, B. J. Halperin, and C. M. Varma, Philos. Mag. **25**, 1 (1972).

[4] D. A. Parshin, Fiz. Tverd. Tela (St. Petersburg) **36**, 1809 (1994) [Phys. Solid State **36**, 991 (1994)].

[5] S. V. Gushchin and S. Dzhumanov, Pis'ma Zh. Tekh. Fiz. **21**(21), 1 (1995) [Tech. Phys. Lett. **21**, 861 (1995)].

[6] V. L. Gurevich and D. A. Parshin, Zh. Éksp. Teor. Fiz. **83**, 2301 (1982) [Sov. Phys. JETP **56**, 1334 (1982)].

[7] V. L. Gurevich, *Kinetics of Phonon Systems* [in Russian], Nauka, Moscow (1980).

[8] V. G. Karpov and D. A. Parshin, Zh. Éksp. Teor. Fiz. **88**, 2212 (1985) [Sov. Phys. JETP (1985)].

Translated by R. M. Durham

Acceleration of the wall of a conducting cylinder undergoing thermal expansion in a strong magnetic field

G. A. Shneerson

St. Petersburg State Technical University

(Submitted February 5, 1997)
Pis'ma Zh. Tekh. Fiz. **23**, 10–16 (June 12, 1997)

Calculations are made of the abrupt acceleration of the wall of a cylinder undergoing heating in a strong magnetic field. It is shown that the expansion of a thin-walled liquid-metal cylinder resembles an ''explosive instability''; in the model used, the velocity of the boundary and the azimuthal current increase without bound in a finite time. It is noted that this effect may also be observed for an elastic shell, and the influence of the electromagnetic retarding forces does not eliminate the singularity in the solution, but merely shifts the time when it appears. © *1997 American Institute of Physics.* [S1063-7850(97)00306-6]

The thermal expansion of a conducting medium during an electrical explosion in an axial magnetic field is accompanied by an induced azimuthal current. This causes additional heating of the conductor and increases the expansion velocity. Under certain conditions the process tends to build up, which may result in heating and acceleration of the explosion products.

Computer modeling has shown that this process may accompany the electrical explosion of a wire.[1] In the present paper, another case of independent interest is considered, involving the expansion of a condensed-phase conductor, comprising a thin-walled cylinder of radius R_0. Let us assume that the wall thickness h and the radius increment ΔR are much smaller than the initial radius: $h,\ \Delta R \ll R_0$. Simple estimates show that as the wall is heated, it may be accelerated to a high velocity in a short time as a result of thermal expansion. For example, even for a temperature increment $\Delta T = 1000$ K this velocity is of the order of 10^4 m/s if the initial radius is $R_0 \approx 10^{-2}$ m and the temperature jump takes place in $\sim 10^{-8}$ s. It is easy to show that a current density of the order of 10^{12} A/m^2 must be induced in the conductor to achieve these conditions. In an ultrastrong magnetic field the wall may be heated by a different mechanism as a result of ''self-excitation'' of an azimuthal current which is induced in the wall as the latter moves and increases as the velocity increases.

This model assumes that the azimuthal voltage σ_φ is related to the increase in the bulk thermal energy density $\Delta q'$ and the radius ΔR by:

$$-\sigma_\varphi = \Gamma_0 \Delta q' - E\frac{\Delta R}{R_0}, \tag{1}$$

where Γ_0 is the Grüneisen constant and E is the elastic modulus. Equation (1) is derived from the two-term equation of state of the medium. The equation of motion for the wall is

$$R_0 \gamma \frac{d^2 \Delta R}{dt^2} = -\sigma_\varphi + f_r, \tag{2}$$

where γ is the density of the medium and f_r is the radial component of the electromagnetic force. If we assume that the azimuthal component of the current density δ_φ and the axial component δ_z are constant over the wall thickness, then $f_r = (\delta_\varphi B_z - \delta_z B\varphi)h$, and in a strong axial field the second term is negligible.

The induction law yields an equation for the azimuthal current density

$$\delta_\varphi = -\frac{1}{2\pi R\rho}\frac{d}{dt}(\pi R^2 B_i), \tag{3}$$

where ρ is the resistivity of the material (in the model ρ=const) and B_i is the magnetic field inside the cylinder. The value of B_i is slightly smaller than the external field B_e:

$$B_i = B_e + \mu_0 h \delta_\varphi, \tag{4}$$

where $\delta_\varphi < 0$. We transform Eq. (3) to

$$\delta_\varphi = -\frac{1}{\rho}\left(B_e \frac{dR}{dt} + \frac{R}{2}\frac{dB_e}{dt} + \frac{\mu_0 h}{2R}\frac{d}{dt}(\delta_\varphi R^2) \right). \tag{5}$$

We further assume B_e=const and $B_0 - B_i = -\mu_0 h \delta_\varphi \ll B_0$, which allows us to retain only the first term on the right-hand side of Eq. (5).

The bulk heat dissipation is determined by both components of the current density and by the resistivity ρ of the conductor:

$$\frac{d\Delta q'}{dt} = \rho(\delta_\varphi^2 + \delta_z^2). \tag{6}$$

After differentiating Eq. (2) with respect to time, we obtain the following relation for the azimuthal component of the current density (δ_z is assumed to be constant):

$$\frac{1}{\rho}\frac{d^2(\delta_\varphi \rho)}{dt^2} + \frac{d\delta_\varphi}{dt}\frac{B_0^2}{\gamma\rho} + \frac{E\delta_\varphi}{\gamma R^2} + \frac{\Gamma_0 B_0}{\gamma R_0}\delta_\varphi^2 = -\frac{\Gamma_0 B_0}{\gamma R_0}\delta_z^2. \tag{7}$$

In its simplest form, the acceleration of the shell and self-excitation of an azimuthal current can be demonstrated for a liquid-metal cylinder, neglecting electromagnetic retarding forces. Under these assumptions, the second and third terms on the left-hand side of Eq. (7) can be neglected. Let us assume that as a result of the passage of a short-lived

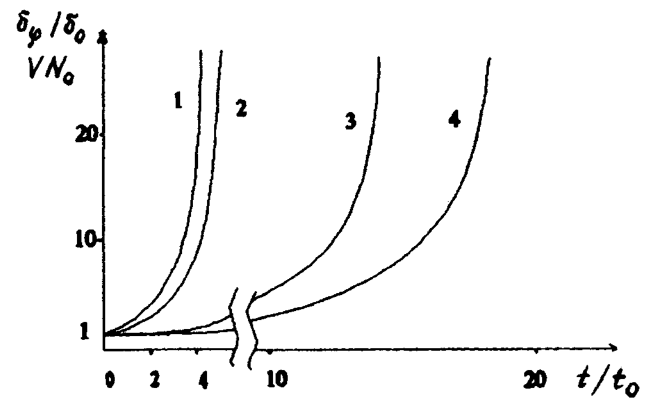

FIG. 1. Curves describing the self-excitation of azimuthal current and motion of the wall of a liquid-metal cylinder undergoing thermal expansion in a strong magnetic field: *1* — $\beta=0$, *2* — $\beta=1$, *3* — $\beta=10$, and *4* — $\beta=20$.

current pulse the cylinder wall instantaneously acquires the initial velocity V_0. The right-hand side of Eq. (7) can then be taken as zero and the conditions $\delta_\varphi(0)=-(B_0/\rho)V_0$ and $(d\delta_\varphi/dt)=0$ can be taken as the initial conditions. Thus, instead of Eq. (7), we obtain

$$\frac{d^2\delta_\varphi}{dt^2}+\frac{\Gamma_0 B_0}{\gamma R_0}\delta_\varphi^2=0. \tag{8}$$

The solution of Eq. (8) with these boundary conditions has the form of a relation linking the dimensionless time $x=t/t_0$ and the dimensionless current $y=\delta_\varphi/\delta_\varphi(0)$. This relation is given by

$$x=\sqrt{\frac{3}{2}}\int_1^y\frac{dy}{\sqrt{y^3-1}}, \tag{9}$$

and the characteristic time is $t_0=B_0^{-1}(\gamma\rho R_0/\Gamma_0 V_0)^{1/2}$. The dependence $y(x)$ may be expressed in terms of the Weierstrass function and is plotted in Fig. 1 (curve *1*), showing an abrupt increase in the azimuthal current. In this model a singularity — an unbounded increase in current — is observed at $t_1=2.97t_0$. Near this time, the variation in current is described by

$$\delta_\varphi=-\frac{6\gamma R_0}{\Gamma_0 B_0(t_1-t)^2}. \tag{10}$$

The current density and the wall velocity increase from $2\delta_\varphi(0)$ and $2V_0$ to $20\delta_\varphi$ and $20V_0$, respectively, over the time interval between 1.5 and $2.4t_0$. For aluminum ($\rho\approx10^{-7}\,\Omega\cdot\mathrm{m}$ and $\gamma\approx3\times10^3$ kg/m^3), we obtain $t_0\approx0.6$ μs if $R_0=3$ cm, $B=100$ T, and $V_0=1$ km/s. In this example, the increase in radius over the time taken to accelerate the wall to $20V_0$ is around 2.5 mm. This example shows that the thermal expansion of a shell in a strong field is accompanied by the buildup of a particular type of instability: the faster the expansion, the greater the current induced in the shell and the more intense the Joule heating causing the expansion. Obviously, when the current increases without bound near the point t_1, the role of the last term in Eq. (5) ceases to be small. The influence of this term needs to be analyzed separately, and gives an asymptotic solution describing the limiting case $h\rightarrow0$. It can be shown that the shell heating comes from the magnetic field energy: this energy decreases, since for a constant external field $B_e\approx B_0$, the region of weaker field $B_i<B_e$ increases. The action of the electromagnetic retarding force, taken into account by the second term on the left-hand side of Eq. (7), does not eliminate the self-excitation of the azimuthal current but merely shifts this process in time. This is shown by the series of curves *2*, *3*, and *4* (Fig. 1) plotted for different values of the dimensionless parameter $\beta=B_0(R_0/\gamma\cdot\rho\cdot r_0V_0)^{1/2}$, which characterizes the retarding effect.

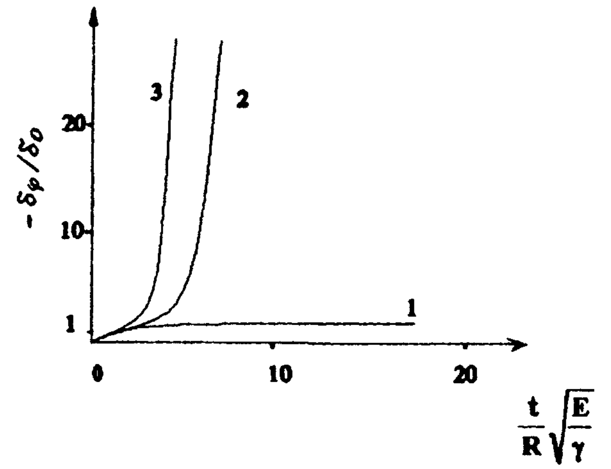

FIG. 2. Time-dependent behavior of the azimuthal current excited during the heating and expansion of an elastic cylinder in a strong magnetic field: *1* —$\alpha=(B_0/\rho)\sqrt{2R/E\gamma}=2$, $\delta_z/\delta_0=1$, *2* — $\alpha=2$, $\delta_z/\delta_0=1.2$, and *3* — $\delta_z/\delta_0=2$.

The influence of a strong axial magnetic field on the thermal expansion of a solid conductor may be described by a model which describes the expansion of a cylinder wall exhibiting the properties of an elastic solid (under the assumptions E = const, ρ = const). In this case, the complete equation (7) should be used. We confine ourselves to the case where the current δ_z is initiated by a pulse and then does not change with time. This equation may have a steady-state solution when δ_φ = const and dR/dt =const; it describes the asymptotic form of $\delta_\varphi(t)$. This behavior is observed in the steady-state regime after the transient process has decayed. In this case, we obtain the equation

$$\delta_\varphi^2+\frac{E\delta_\varphi}{B_0\Gamma_0R_0}+\delta_z^2=0, \tag{11}$$

whose solution has the form

$$\delta_\varphi=\delta_\infty=-\frac{E}{2B_0\Gamma_0R_0}\pm\sqrt{\left(\frac{E}{2B_0\Gamma_0R_0}\right)^2-\delta_z^2}. \tag{12}$$

Here, only the positive root of the equation is physically meaningful, since in the limit $B_0\rightarrow0$, it yields $\delta_\infty=0$. This solution shows that for given δ_z, the azimuthal current density increases with the field B_0. In the asymptotic regime, the electromagnetic force compensates for the azimuthal voltage, the radius increases with constant velocity

$d(\Delta R)/dt = -\rho\delta_\infty/B_0$, and the azimuthal current density does not depend on the conductivity. It follows from Eq. (12) that this regime can only be achieved provided that the axial current density does not exceed

$$\delta_0 = \frac{E}{2B_0\Gamma_0 R_0}. \qquad (13)$$

To determine the value of this parameter is outside the scope of this example. It is characteristic of the acceleration of an elastic cylindrical shell in an axial field. If $\delta_z > \delta_0$, no asymptotic regime is established and a time-dependent process occurs in which the velocity and current δ_φ increase without bound within a finite time within the framework of this model. The final stage of the process is described by Eq. (8) and the solution near the point of discontinuity is described by formula (10).

Figure 2 shows three examples of a numerical solution of the complete equation (7), one (curve *1*) describing the asymptotic regime and the other two (curves *2* and *3*) describing continuous acceleration. Note that a singularity appears in this example, as in the previous one, despite the electromagnetic retarding force. The self-excitation of the azimuthal current is interesting because, despite the counteraction of the elastic and electromagnetic forces, this regime can accelerate the shell to a state where the acceleration of the wall is limited only by the inertia of the material. For a given current δ_z this regime, which is a manifestation of the instability described above, is established if

$$B > B_1 = \frac{E}{2\Gamma_0 R_0 \delta_z} = \frac{\pi E h}{\Gamma_0 i_z}, \qquad (14)$$

where i_z is the axial current in a metal foil cylinder of thickness h. It follows from this condition that for copper foil ($E \approx 2\times10^{11}$ Pa, $\Gamma_0 \approx 2$) of thickness $h = 0.1$ mm with the current $i_z \approx 3\times10^5$ A, we have $B_1 \approx 100$ T. This example indicates that a very strong magnetic field must be used to achieve self-excitation of the azimuthal current and abrupt acceleration of the walls of the cylindrical shell.

This work was supported by the Russian Fund for Fundamental Research (Grant No. 96-02-19185a).

[1] S. N. Kolgatin and G. A. Shneerson, Pis'ma Zh. Tekh. Fiz. **20**(5), 67 (1994) [Tech. Phys. Lett. **20**, 207, 1994)].

Translated by R. M. Durham

Synthesis of a $Bi_2Sr_2CaCu_2O_y$ high-temperature superconducting phase with T_c° above 100 K

Zh. M. Tomilo, N. A. Prytkova, E. M. Gololobov, and D. M. Turtsevich

Institute of Solid-State and Semiconductor Physics, Belarus Academy of Sciences, Minsk

(Submitted December 2, 1996)
Pis'ma Zh. Tekh. Fiz. **23**, 17–22 (June 12, 1997)

A high-temperature superconductor with the $Bi_2Sr_2CaCu_2O_y$ structure and a superconducting transition temperature $T_c^{\circ}=102-107$ K has been synthesized. The synthesis conditions are described and results of a phase analysis, and of resistive and inductive measurements are reported. © *1997 American Institute of Physics.* [S1063-7850(97)00406-0]

Against the background of the numerous studies dealing with the properties of superconducting phases in bismuth-containing high-temperature superconductors (BSCCO), there have been several reports of a highly interesting experimental result — a superconducting phase has been synthesized with T_c° greater than 100 K and having the crystal structure of the $Bi_2Sr_2CaCu_2O_y$ phase (Bi-2212) (Refs. 1–3). It is fairly difficult to explain these results, first because the experimental observations were obtained for samples with different cation ratios and different additives, and second, because there are too few results. Some authors, who observed an increase in T_c to 110–120 K for Bi-2212 superconductors doped with mercury[3] and silver,[4] attributed this observation to a change in the oxidation state of the copper.

In the present paper we report the results of a study of the phase composition and superconducting properties of $BiSrCaCu_2O_y$ (Bi-1112) superconductors, where the cupric oxide normally used for synthesis is partially replaced by metallic copper. The role of copper atoms in the establishment of high-temperature superconductivity has always attracted the close attention of researchers. According to Ref. 5, the maximum value of T_c for oxide superconductors should be expected for a copper state with a valence close to $+2.2$. The composition Bi-1112 was chosen because it contains an excess of calcium and copper cations relative to the stoichiometry of $Bi_2Sr_2CaCu_2O_y$, which is conducive to obtaining Bi-2212 materials with superior superconducting parameters.[6–11] The initial components used to prepare the samples were $SrCO_3$ and $CaCO_3$ carbonates, Bi_2O_3 and CuO oxides, and finely disperse copper. The cupric oxide was replaced by copper in accordance with the cation ratio: $Bi^{3+} : Sr^{2+} : Ca^{2+} : Cu^{2+} : Cu = 1 : 1 : 1 : 2(1-x) : 2x$, where $x = 0.0$, 0.1, 0.2, 0.3, and 0.4. The samples were synthesized in air in three stages: stage I involved short-term holding (1–10 min) at relatively high temperatures (900–980 °C), while stages II and III involved annealing at 860 ±15 °C and 810 °C, respectively, for between one and several days. After each synthesis stage, the samples were ground up and pressed into pellets 1–2 mm thick and 10 mm in diameter. The phase composition was studied by x-ray diffraction analysis (DRON-3 diffractometer, CoK_{α} -radiation) and microstructural analysis. The superconducting phases were identified as in Refs. 12 and 13. The superconducting transition temperatures were determined from resistance and magnetic measurements.

Our investigations revealed that the superconducting properties of the materials thus synthesized depend on the quantity of metallic copper replacing the cupric oxide in the initial mixture, and on the synthesis conditions. An increase in temperature and hold time at stage I reduces the effect of partially replacing CuO with Cu. Samples having a superconducting transition temperature higher than 100 K and consisting almost entirely of a single $Bi_2Sr_2CaCu_2O_y$ phase were obtained under specific synthesis conditions. Figure 1

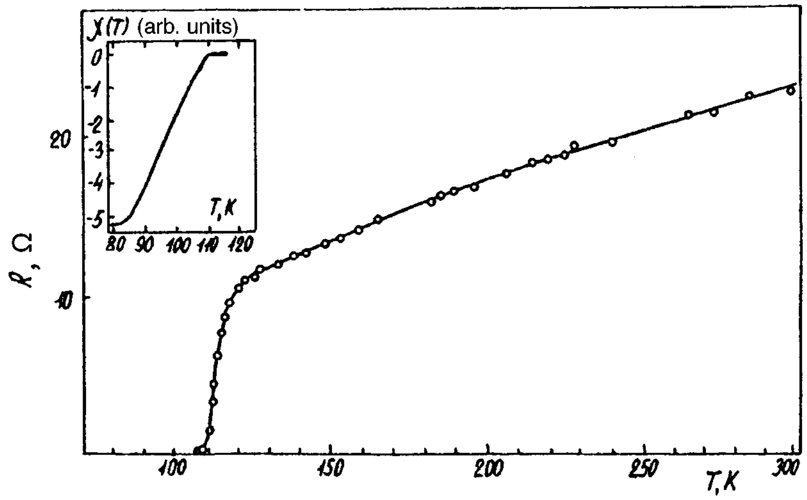

FIG. 1. Temperature dependence of the electrical resistance of sample No. 673 ($x=0.3$) with $T_c^{\circ}(R=0)=107$ K. The inset shows the magnetic measurements for this sample at temperatures of 77.4–120 K.

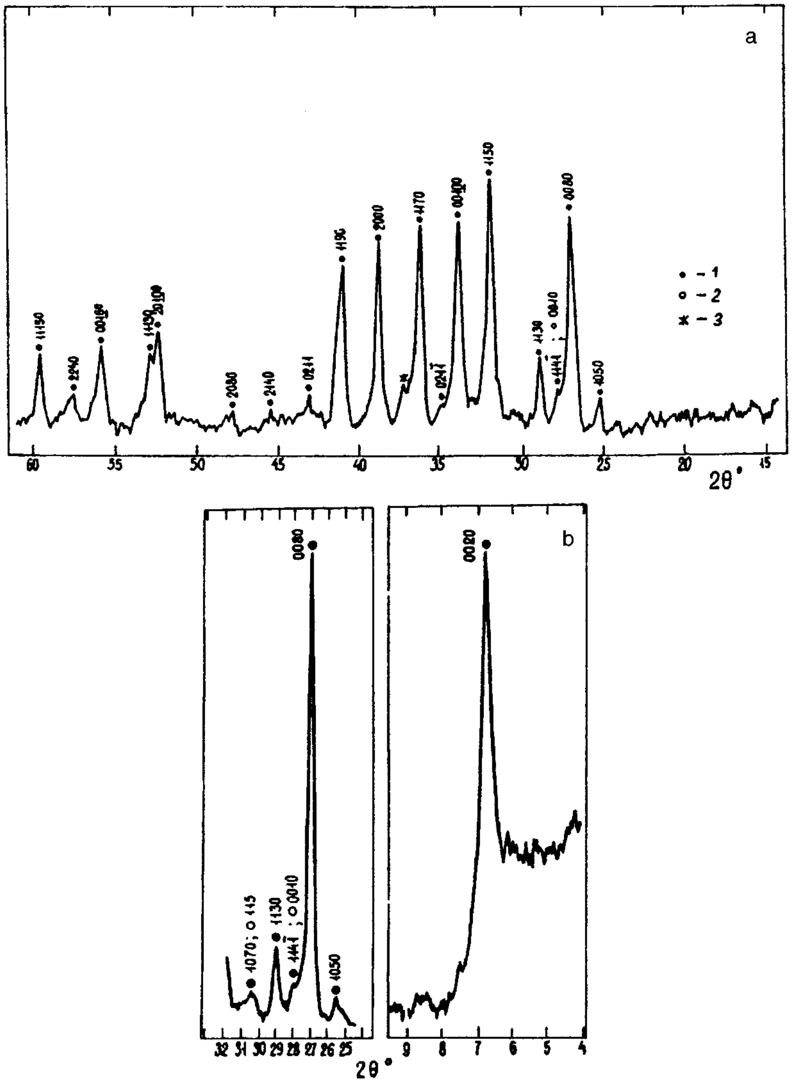

FIG. 2. a — Diffraction pattern of ground up sample No. 673 ($x=0.3$) with $T°_c(R=0)=107$ K (CoK$_\alpha$ radiation); b — portions of the diffraction pattern for reflection angles of 4–9° and 25–32°. Notation: *1* — Bi-2212 phase, *2* — Bi-2223 phase, and *3* — "yellow phase."[14,15]

shows the temperature dependence of the electrical resistance $R(T)$ for a sample with $x=0.3$ (sample No. 673) and $\overset{\circ}{T}_c(R=0)=107$ K. The inset gives the inductive measurements for this sample, which show that the values of $\overset{\circ}{T}_0$ determined from the resistance and magnetic measurements are the same, 107–108 K. For samples in this series containing metallic copper with x = 0.0, 0.1, 0.2, and 0.4, the values of $\overset{\circ}{T}_c$ were appreciably lower and did not exceed 77.4 K. The samples in this series were synthesized under the following conditions: stage I — 900 °C, 10 min, stage II — 800 °C, 24 h, and stage III — 810 °C, 24 h.

A phase analysis of sample No. 673 revealed that it consists of small, light-gray blocks, comprising the superconducting $Bi_2Sr_2CaCu_2O_y$ phase, and uniformly distributed black regions, which are pores. There is also a small quantity of nonsuperconducting "yellow phase."[14,15] The presence of the superconducting $Bi_2Sr_2Ca_2Cu_3O_y$ (Bi-2223) phase was scrutinized with particular care. Figure 2a shows a diffraction pattern of the ground up sample No. 673 and Fig. 2b shows portions of the diffraction pattern in the ranges of reflection angles 2θ: 4–8°, 27–28°, and 30–31°, recommended for identifying the Bi-2223 phase.[13] According to this analysis of the phase composition of the sample having $\overset{\circ}{T}_c(R=0)=107$ K, it may be presumed that if the Bi-2223 phase is present in this sample, the amount is very negligible and is obviously insufficient to induce a superconducting transition with $\overset{\circ}{T}_c(R=0)$ at 107 K (Ref. 16).

To conclude, we have shown that in a BSCCO system with the cupric oxide partially replaced by metallic copper, superconducting samples with $\overset{\circ}{T}_c \sim 110$ K and a $Bi_2Sr_2CaCu_2O_y$ crystal phase structure can be synthesized under certain conditions. Disagreement between the characteristic superconducting transitions and the phase composition was observed not only for the $Bi_2Sr_2CaCu_2O_y$ phase,[1–3] but also the for $Bi_2Sr_2CuO_y$ phase.[17–19]

The authors would like to thank L. A. Kurochkin for performing the magnetic measurements.

[1] V. N. Konev, T. B. Popova, and N. B. Petrunovskaya, Sverkhprovodimost' (KIAE) **6**, 412 (1993).
[2] Y. -R. Li and Y. -M. Li, Chin. Sci. Bull. **36**, 835 (1991).
[3] S. Lahiry, Y. S. Reddy, B. Sarkar *et al.*, Physica C **225**, 207 (1994).
[4] Y. Yu, Y. Jin, S. Y. Din *et al.*, Phys. Status Solidi A **151**, K9 (1995).
[5] R. J. Cava, A. W. Hewat, E. A. Hewat *et al.*, Physica C **165**, 419 (1990).
[6] S. Zannella, A. M. Ricca, V. Ottoboni *et al.*, J. Less-Common Met. **150**, 39 (1989).

[7] S. Kobayashi and S. Wada, in *Proceedings of ISS′89, ISTES*, 1989, pp. 125–128.

[8] M. Aslan, H. Jaeger, M. Maric, and K. Scnulze, Mater. Sci. Eng. B **10**, 133 (1991).

[9] Y. Tanaka, T. Asano, K. Jikihara *et al.*, Jpn. J. Appl. Phys. **27**, L1655 (1988).

[10] E. M. Gololobov, N. A. Prytkova, V. F. Savchenko *et al.*, Vestn. Akad. Nauk BSSR Ser. Fiz. Mat. Nauk No. 4, 52 (1991).

[11] E. M. Gololobov, N. A. Prytkova, Zh. M. Tomilo *et al.*, Sverkhprovodimost' (KIAE) **5**, 2109 (1992) [Superconductivity **5**, 2001 (1995)].

[12] M. Onoda, A. Yamamoto, E. Takayama-Muromaki, and S. Takekawa, Jpn. J. Appl. Phys. **27**, L833 (1988).

[13] G. Calesstani, C. Rizzoli, G. D. Andreetti *et al.*, Physica C **158**, 217 (1989).

[14] L. N. Leonyuk, N. I. Leonyuk, and E. L. Belokoneva, Sverkhprovodimost' (KIAE) **2**, 36 (1989) [Superconductivity **2**, 48 (1989)].

[15] Y. Fujiwara, S. Hirata, M. Nishikubo *et al.*, IEEE Trans. Magnetics **MAG-27**, 1166 (1991).

[16] G. Paterno, Mater. Chem. Phys. **23**, 365 (1989).

[17] T. Ishida and T. Sakuma, Physica C **167**, 258 (1990).

[18] M. Tokano, Z. Hirai, M. Azuma, and Y. Takeda, Physica C **191**, 441 (1992).

[19] L. Wang, S. X. Shang, H. Wang *et al.*, Appl. Phys. A **58**, 75 (1994).

Translated by R. M. Durham

Direct photodesorption of ions from the surface of a crystal

V. N. Strekalov

“STANKIN” State Technical University, Moscow

(Submitted January 5, 1997)
Pis’ma Zh. Tekh. Fiz. **23**, 23–26 (June 12, 1997)

A model of the direct photodesorption of ions from the surface of a crystal, reminiscent of the ionization of an atom in the external photoelectric effect, is studied. The model is based on the concept of a quasiclassical ion, whose motion in a surface potential well is described by a wave packet. The choice of wave function in the form of a packet may be justified by a variational principle, by finding the parameters of the packet. These parameters may also be selected from known experimental data. These methods are standard in solid state physics and make it unnecessary to take into account the form and magnitude of the operator describing the interaction between the ion and the crystal surface. © *1997 American Institute of Physics.* [S1063-7850(97)00506-5]

A search through electronic data banks reveals an abundance of studies dealing with laser-induced inelastic processes in solids. These processes include photodesorption of impurities and intrinsic atoms from various surfaces, cold photoevaporation, photoablation, and other processes of a similar physical nature. Most of the publications have reported experimental results, while the theoretical description of these processes has so far attracted scant attention. It is not very difficult to formulate theoretical models of inelastic processes at a surface,[1] but complete and accurate quantum-mechanical calculations are not generally performed using these models for two main reasons.

1. The form of the operator describing the interaction between an ion and a crystal surface is unknown and model Hamiltonians are unable to provide a unified description of possible diffusion-like processes.

2. It has not been proven that a model Hamiltonian can be considered to be a small perturbation so as to allow perturbation theory to be applied.

An attempt to overcome some of these difficulties is as follows. Let us assume that the motion of a heavy ion is quasiclassical, i.e., the ion can be viewed as a wave packet. This valuable information can be used to select a trial wave function whose parameters (including not only the variances of the dimensions but also the energy eigenvalues and the depth of the potential well in which the ion is bound) are determined using a variational principle.[2] However, these parameters need not be calculated, which is a separate major problem, but rather can be determined experimentally. If we also assume that a packet with minimum indeterminacy has the same form regardless of the type and magnitude of the action on the particle,[2,3] the unperturbed “crystal + ion” problem can be considered to be solved without specifying the ion-crystal interaction operator.

Similar methods are frequently used in solid state physics. In this context, mention may be made of the choice of Bloch functions for quasielectrons, the use of experimental data on the permittivity, effective mass, band gap, and so forth.

Having the approximate “variational” wave functions of the unperturbed system, we can systematically allow for increasingly smaller perturbations and describe various diffusion-like processes. A similar method was used in Refs. 4 and 5.

Let us apply the proposed method to find the probability of direct photodesorption of ions in a laser field. We shall assume that desorption takes place as a result of an ion absorbing a photon of energy exceeding the binding energy ε_b of the ion to the surface, after which the ion is converted to the free state. The Hamiltonian corresponding to this system has the form

$$H=H_0+V_1+V_2. \qquad (1)$$

Here, H_0 is the kinetic energy operator of an ion having the mass M and effective charge Ze, and the ion momentum operator is denoted by $\hat{\mathbf{P}}$. The term V_1 is the potential energy operator of the ion, which takes into account all the interactions between the ion and the intrinsic atoms of the crystal. The magnitude and form of V_1 are unknown, but this operator determines the binding energy or the depth of the potential well in which the ion is bound, as well as the rms spread a_n associated with the wave packets, which indicates the dimensions of the ion in various states. These values are determined experimentally so there is no need to specify the form of V_1.

The operator describing the interaction between an ion and the electric field of a light wave has the usual form[6]

$$V_2\frac{Ze}{M\omega}\,\hat{\mathbf{P}}\cdot\mathbf{E}_0\cos\omega t, \qquad (2)$$

where the field is assumed to be nonresonant and acts on the ion as on a structureless particle, and E_0 and ω are the amplitude and frequency of the field.

Photodesorption may be accompanied by intra-ion electronic transitions and by charge transfer between ions. However, these processes are described by the leading orders of perturbation theory and are less probable than the direct photodesorption transition.

The operator (2) can be used to find the probability of a photodesorption transition in the first order of perturbation theory. As usual,[6] we have

$$dw_{kn}=\frac{2\pi}{\hbar}\left|\left\langle k\right|\frac{Ze}{2M\omega}\hat{\mathbf{P}}\cdot\mathbf{E}_0\left|n\right\rangle\right|^2 d\rho(E_n), \tag{3}$$

where

$$d\rho(E_n)=\frac{V}{(2\pi\hbar)^3}P_nMd\Omega. \tag{4}$$

Here $|n\rangle$ and $|k\rangle$ are the initial (bound) state of the ion and its final (free) state, Ω are the angular variables, and V is the normalization volume.

The wave function of the initial state allows for motion of the ion from inside the crystal to the surface with the momentum P_n, so that the packet corresponding to the initial state has the form

$$\Psi_n(\mathbf{R})=(2\pi a_n^2)^{-3/4}\exp\left\{\frac{i}{\hbar}\mathbf{P}_n\cdot\mathbf{R}-\frac{R^2}{4a_n^2}\right\}. \tag{5}$$

The ''incidence'' of the ion at the surface from inside the crystal is indicated by the sign of the product $\mathbf{P}_n\cdot\mathbf{R}$, which should be taken into account when integrating over the angles Ω.

After simple transformations, in fact repeating the calculations of the atomic photoionization probability,[6] we obtain the probability

$$w_k=\frac{2\pi}{\hbar}\frac{a_0^3}{(2\pi\hbar)^3}\frac{2(2\pi)^{5/2}(Ze)^2P_k^3}{3M\omega^2}E_0^2, \tag{6}$$

where P_k is the momentum of the ion in the final state. We also assume that the dimensions of the ion in different states are approximately the same and we introduce the average variance a_0.

To estimate w_k, we take $a_0\cong 3\times 10^{-8}$ cm, $M\cong 8\times 10^{-23}$ g, $Z=1$, and $\omega\cong 4\times 10^{15}$ rad/s. If $\varepsilon_k\cong 0.5$ eV, then $P_k\cong 10^{-17}$ g$\cdot$ cm/s, which gives $w_k\cong 10^7 E_0^2$ s^{-1}. In a laser field with $E_0\cong 3\times 10^5$ V/cm$=10^3$ esu, we have $w_k\cong 10^{13}$ s^{-1}. This high probability shows that this type of desorption may make a significant contribution to the experimentally observed values.

In the field E_1 corresponding to a single photon per unit volume (at this frequency $E_1\cong 10^{-5}$ esu), the probability is $w_1\cong 10^{-3}$ s^{-1}. It is useful to compare this value with the probability w_2 of the photoeffect from a molecule or dielectric, where an electron is localized in a volume $\sim a_0^3$. Replacing the ion mass by the electron mass in Eq. (6) gives $w_2\cong 3.4\times 10^{-6}$. However, the usual calculations of the atomic photoionization probability[2,6] for these conditions give $w_3\cong 8.9\times 10^{-7}$ s^{-1}. The results for w_2 and w_3 differ by approximately a factor of 4, which is quite reasonable if we bear in mind how much these models differ.

To sum up, the wave packet model gives reasonable results and can be used to make a theoretical study of the photodesorption of ions. This model is also suitable for describing other diffusion-like processes.

[1] T. Y. Chuang, Surf. Sci. Rep. **3**, 1 (1983).

[2] L. I. Schiff, *Quantum Mechanics*, 3rd ed. (McGraw-Hill, New York, 1968) [Russ. transl. of 2nd ed., IL, Moscow, 1957].

[3] W. H. Louisell, *Radiation and Noise in Quantum Electronics* (McGraw-Hill, New York, 1964) [Russ. transl., Nauka, Moscow, 1972].

[4] V. N. Strekalov, Fiz. Tekh. Poluprovodn. **20**, 1939 (1986) [Sov. Phys. Semicond. **20** 1218 (1986)].

[5] V. N. Strekalov, Poverkhnost', No. 11, 55 (1989).

[6] A. S. Davydov, *Quantum Mechanics* (Pergamon Press, Oxford, 1965) [Russ. original, Nauka, Moscow, 1963].

Translated by R. M. Durham

Magnetic hysteresis and dissipative losses in superconducting films

A. A. Elistratov and I. L. Maksimov

Nizhniĭ Novgorod State University

(Submitted December 23, 1996)
Pis'ma Zh. Tekh. Fiz. **23**, 27–33 (June 12, 1997)

An analysis is made of the response of thin-film superconductors to an oscillating magnetic field. The field strengths for defreezing and expulsion of the flux are determined. A hysteresis curve is plotted for the sample over the entire oscillation cycle of the magnetic field. The dissipative loss power is determined as a function of the amplitude of the alternating field.
[S1063-7850(97)00606-X]

The hysteretic behavior of the magnetization curves of low-dimension type-II superconductors is governed by the combined influence of bulk and edge pinning of Peierls-Abrikosov vortices, which is responsible for the establishment of metastable magnetic flux structures in these systems. It is known that hysteresis losses caused by bulk pinning occur in hard superconductors in an arbitrarily weak ac magnetic field.[1] At the same time, an edge barrier considerably delaying flux penetration/expulsion, leads to threshold-type dissipation in low-dimension superconductors.[2] The combined influence of both mechanisms of irreversibility on the electromagnetic characteristics of bulk superconductors were studied fairly comprehensively in Refs. 3 (using a local model) and 4 (using a nonlocal model of the critical state). However, this aspect has not been investigated in low-dimension superconductors characterized by the formation of nontrivial magnetic flux structures. An essentially nonlocal intervortex interaction, fundamentally altering the form of the Maxwell-London equations in these systems, makes it fairly difficult to analyze the response of the system to an ac magnetic field.

In the present paper we consider the response to an oscillating magnetic field by thin-film superconductors with edge bulk pinning of the flux. The field strengths for defreezing H_{df} and expulsion H_{ex} of the flux are determined. A hysteresis curve is plotted for the sample over the entire cycle of magnetic field oscillation between $+H_0$ and $-H_0$. The power of the dissipative losses is determined as a function of the amplitude of the alternating field.

We consider a superconducting film strip of thickness d $(0 \leqslant z \leqslant d)$ and width $2W$ $(|Y| \leqslant W)$ in a magnetic field $\mathbf{H}=(0,0,H)$ perpendicular to its surface. In fields greater than the penetration field H_1 of the first vortex (of the order of a few kilooersted for well-formed edges[2]), the flux penetrates from the edges into the bulk of the film and concentrates in the central region. The long-range nature of the intervortex repulsion combined with a high edge barrier leads to the establishment of a new type of critical state, whose structure differs substantially from the Bean model.[5,6] In this state, the region of flux concentration comprises two strips, symmetric about the center and oriented along the X axis.

As the external magnetic field decreases from its maximum H_0, the vortices will be ''frozen'' at their initial sites of attachment — in the region $\Theta_{10} \leqslant |y| \leqslant \Theta_{20}$ (Fig. 1), where $y=Y/W$ is a dimensionless coordinate, and the boundaries of the region occupied by the flux were determined in Ref. 5 (the notation from Ref. 5 will be used here and subsequently in the text; the subscript ''0'' corresponds to the distribution of the vortices and currents at $H=H_0$). The ''frozen'' flux state will persist until the resultant surface current density $i_t=j_t d$ (j_t is the bulk current density) in the region of the outermost vortices $(y \approx \Theta_{20})$ reaches $-i_p$ (i_p is the depinning current density for Peierl-Abrikosov vortices in a film with bulk pinning). The current distribution in this regime may be written using the superposition principle:

$$i_t(y,H)=i_t(y,H_0)+\frac{H-H_0}{H}i_M(y), \tag{1}$$

where $i_M(y)=Hy/(2\pi\sqrt{1-y^2})$ is the Meissner component of the total surface current density i_t. An expression for the latter was derived in Ref. 5 in the weak pinning approximation $(H_1/i_p \gg 1)$ and corresponding results for strong flux pinning will be published.

We find the magnetic field H_{df} for defreezing the magnetic flux by using Eq. (1), equating $i_t(\Theta_{20},H_{df})=-i_p$ (a necessary condition for the displacement of vortices located in the region $y \approx \Theta_{20}$ toward the edge of the film). Using the obvious equality $i_t(\Theta_{20},H_0)=i_p$, we obtain

$$H_{df}=H_0-4\pi i_p\sqrt{\frac{1-\Theta_{20}^2}{\Theta_{20}^2}}. \tag{2}$$

Note that this result holds for an arbitrary intensity of bulk vortex pinning. It can also be shown that for a small excess above the penetration field H_1 $(H_0-H_1 \ll H_1)$, we find $H_{df} \approx H_0-2H_1<0$ (Fig. 2).

As the field decreases further $(H \leqslant H_{df})$, the region of concentration of the frozen flux $(\Theta_{10} \leqslant |y| \leqslant \Theta_0)$ becomes narrower while the region of ''defrozen'' flux $(\Theta_0<|y| \leqslant \Theta_2)$ expands inside the film and toward the periphery $(\Theta_2>\Theta_{20}$; Fig. 1). In the region $\Theta_0<|y| \leqslant \Theta_2$, we find $i_t(y)=-i_p$, which corresponds to the formation of a critical state of vortex expulsion. For $H=H_{ex}$ the vortices reach the edge of the film $(\Theta_2 \approx 1)$ and then leave the film as the field decreases further. Physically, this corresponds to suppression of the flux expulsion barrier. The value of H_{ex} can be determined from the condition of conservation of the total flux $\Phi_t^{in}(H_0)=\Phi_t(H)$, for $H_{ex} \leqslant H \leqslant H_0$, which with the ''area rule'' (Fig. 1) reduces to

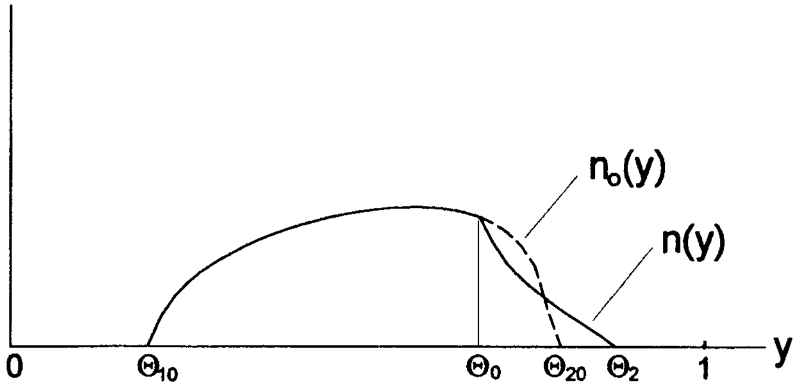

FIG. 1. Distribution of vortex density over the film width $(y>0)$ in the range of fields $H_{df}<H<H_0$ (dashed curve) and $H_{ex}<H<H_{df}$ (solid curve).

$$\int_{\Theta_0}^{\Theta_{20}} n_0(y)dy=\int_{\Theta_0}^{\Theta_2} n(y)dy, \tag{3}$$

where $n(y)$ is determined by solving an integral Maxwell–London equation by the method of forming of Cauchy integrals.[5] The magnitude of the flux penetrating into the film at $H=H_0$, $\Phi_t^{in}(H_0)$ was determined in Ref. 5:

$$\Phi_t^{in}(H_0)=2\mu_0W\{(H_0+4i_p\tanh^{-1}\Theta_{20})[E(\Theta_{20}) -(1-\Theta_{20}^2)K(\Theta_{20})]-4i_p\Theta_{20}K(\Theta_{20})\}, \tag{4}$$

where $E(z)$ and $K(z)$ are complete elliptic integrals of the first and second kinds, respectively, Solving Eq. (3) (with $\Theta_2=1$), using Eq. (4), and performing simple but cumbersome calculations, we can determine the dependence of H_{ex} on H_0 for the case of comparatively weak pinning $H_{1/i_p}=10$ (Fig. 2).

For $H\leqslant H_{ex}$, it is obvious that $\Theta_2\approx 1$ and Θ_0 decreases monotonically until (for $H\leqslant H_{en}^{(-)}$) vortices of opposite polarity — antivortices — begin to enter the film. As a result of the annihilation of vortices and antivortices, the trapped flux decreases abruptly with decreasing H (Fig. 3). In the range of fields $H_{ex}<H\leqslant H_0$, the change in the magnetization is obviously reversible and there are no dissipative losses (we neglect the viscous losses occurring in fields $H_{ex}<H\leqslant H_{df}$). Thus, as the field decreases, the main contribution to the energy dissipation caused by the magnetic reversal of the film and annihilation of vortices is made by the region of fields $-H_0\leqslant H\leqslant H_{ex}$. A similar analysis of the situation when the field increases from $H=-H_0$ to $H=+H_0$ yields the conclusion that the range of fields $H_{ex}^{(-)}\leqslant H\leqslant H_0$ (where $H_{ex}^{(-)}$ is the antivortex expulsion field) makes the dominant contribution to the hysteresis loss power. The behavior of the hysteresis curve $\Phi(H)$ under cyclic variation of the field in the range $-H_0\leqslant H\leqslant H_0$ is plotted in Fig. 3. Note that in films, the behavior of the curve $\Phi(H)$ in the upper half-plane $(\Phi>0)$, resembling an ''airplane-tail'' feature, differs fundamentally from the behavior (resembling a ''whale-tail'' feature) in bulk superconductors.[3] We stress that this unusual behavior of the function $\Phi(H)$ in films is attributable to edge flux pinning (see Ref. 2). Near the vortex expulsion field H_{ex} $(|H_{ex}-H|\ll H_{ex})$, we find $d\Phi_b/dH\approx 0$ (but $d^2\Phi_b/dH^2<0$) (Ref. 3) in bulk samples, whereas in films with an edge barrier we find $d\Phi_f/dH\approx 2\mu_0W>0$ (Refs. 2 and 8).

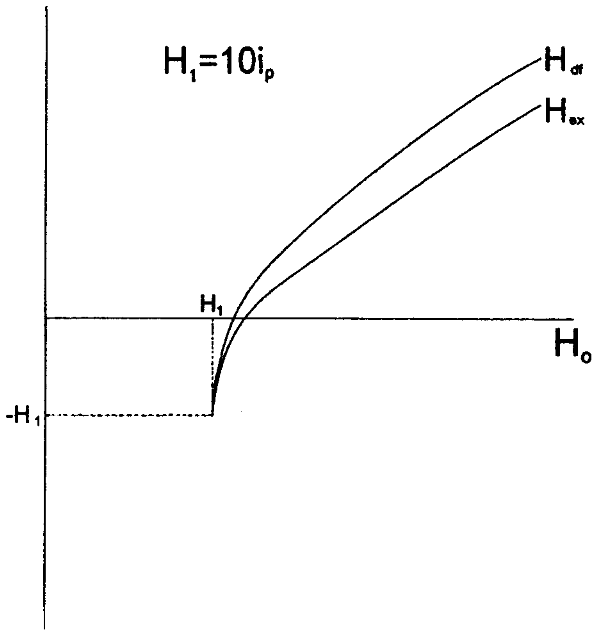

FIG. 2. Flux defreezing field H_{df} and vortex expulsion field H_{ex} as functions of the external magnetic field H_0.

The energy dissipated per unit length of the film over an entire cycle of quasi-steady-state oscillation of the field between $H=-H_0$ and $H=+H_0$ is given by

$$Q(H_0)=\frac{1}{4\pi}\oint Hd\Phi. \tag{5}$$

The dependence $Q(H_0)$ clearly has a threshold, since magnetization-reversal losses only occur when $H_0>H_1$, which reflects the specific characteristics of edge pinning.[2] For $H_0-H_1\ll H_1$, the curve $Q(H_0)$ is almost linear, exhibiting asymptotic behavior $Q(H_0)\propto(H_0-H_1)^1$ with $r\approx 0.7$ when $H_0\geqslant 3H_1$. A comparison between the calculated data and the results of Ref. 7, which demonstrate nonthreshold behavior of $Q(H_0)\propto H_0^q$ (where $q=4$ for $H_0\ll i_p$ and $q=1$ for $H_0\gg i_p$) in films without an edge barrier, reveals a fundamental difference between the irreversibility mechanisms under discussion.

To sum up, the existence of edge pinning can substantially reduce the dissipative losses caused by magnetization

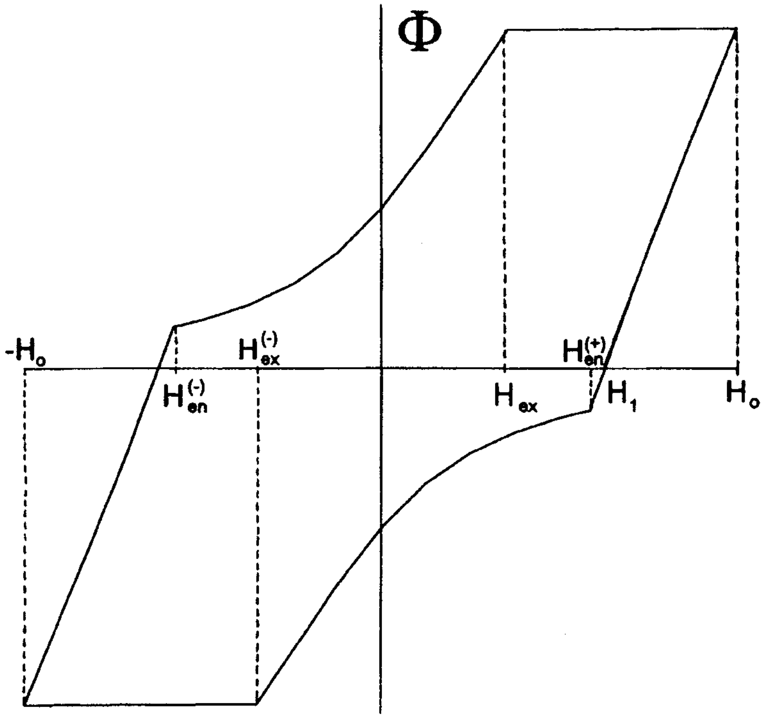

FIG. 3. Flux penetrating into film versus the external magnetic field for $H_1 = 10i_p$, $H_0 = 16i_p$.

reversal in thin-film superconductors, making them highly promising for various technical applications. The proposed analytic model provides a good basis for calculating the impedance of thin-film bridges in ac fields and for obtaining a quantitative description of the generation of higher-order magnetization harmonics.

The authors would like to thank G. M. Maksimova for useful discussions of this model, and also J. Clem for interest in this work and correspondence. This work was supported by the Government of the Russian Federation in conjunction with the International Science Foundation (Grant No. R8J300), the Ministry of Science of the Russian Federation (High-Temperature Superconductivity Project No. 95-057), and by the State Committee for Higher Education of the Russian Federation (Project No. 95-0-7.3-178).

[1] R. G. Mints and A. L. Rakhmanov, *Instabilities in Superconductors* [in Russian], Nauka, Moscow (1984).
[2] I. L. Maksimov, Pis'ma Zh. Tekh. Fiz. **22**(20), 56 (1996) [Tech. Phys. Lett. **22**, 845 (1996)].
[3] J. R. Clem, J. Appl. Phys. **50**, 3518 (1979).
[4] V. S. Gorbachev and S. E. Savel'ev, Zh. Éksp. Teor. Fiz. **109**, 1387 (1996) [JETP **82**, 748 (1996)].
[5] I. L. Maksimov and A. A. Elistratov, JETP Lett. **61**, 208 (1995).
[6] E. Zeldov, A. Larkin, V. B. Geshkenbein *et al.*, Phys. Rev. Lett. **73**, 1428 (1994).
[7] E. H. Brandt and M. Indenbom, Phys. Rev. B. **48**, 12 893 (1994).
[8] M. Benkraouda and J. R. Clem, Phys. Rev. B **53**, 5716 (1996).

Translated by R. M. Durham

Long-term relaxation of the photovoltage in a heteroepitaxial structure

L. V. Shekhovtsov, G. N. Semenova, E. F. Venger, A. V. Sachenko, and Yu. G. Sadof'ev

Institute of Semiconductor Physics, Ukrainian National Academy of Sciences, Kiev;
Scientific-Research Technological Institute, Ryazan

(Submitted December 17, 1996)
Pis'ma Zh. Tekh. Fiz. **23**, 34–41 (June 12, 1997)

The distribution of the transverse photovoltage has been investigated in samples of a Ge–GaAs heterostructure with an oxide layer ($\sim$15 Å) at the interface. A method of simultaneous excitation with modulated and unmodulated radiation is used to observe the long-term relaxation of the photovoltage in these heterostructures. The energy barriers responsible for this effect are localized at the surface of the Ge film and the GaAs substrate, adjacent to the interlying oxide. It is shown that the gradients of the dark carrier concentration in the film and in the substrate are in opposite directions. A transition layer is formed during the growth process and not as a result of the classical heterodiffusion of the components in the film and the substrate. It is noted that the photoconductivity signal observed at the modulation frequency in the field formed at the sample as a result of the unmmodulated illumination must be taken into account in the recorded voltage signal. © *1997 American Institute of Physics.* [S1063-7850(97)00706-4]

1. Studies of the spectral characteristics of the transverse photovoltage observed in a Ge–GaAs heteroepitaxial structure exposed to monochromatic light in the fundamental absorption region of Ge and GaAs, have yielded results which have allowed us to take a new look at the processes involved in forming the properties of thin films and transition layers grown by various methods.[1,2]

The most important result was that the dark carrier concentration gradients in the Ge film and the GaAs substrate are in opposite directions along the interface. This conclusion was indicated by the spectral characteristics of heterostructure samples grown by molecular-beam epitaxy and by vacuum evaporation. It was also observed that heterostructure samples grown by vacuum evaporation incorporate a system of drift and recombination barriers which are formed by cross doping of the film and the substrate during growth. These barriers are responsible for the nonmonotonic dependence of the amplitude of the photovoltage on the intensity of the exciting light and its long-term relaxation.

For heterostructure samples grown by vacuum evaporation and by molecular-beam epitaxy on GaAs substrates with an arsenic-stabilized surface, the amplitude of the transverse photovoltage was sufficient for reliable recording. For samples grown by molecular-beam epitaxy with an oxide layer on the substrate, the voltage was small at the optical intensities used ($I=10^{14}$ photon/cm$^2\cdot$s) and its spectral characteristics could not be measured.

Studies of the properties of these heterostructures are the most interesting from the technological point of view. The deposition of a buffer oxide layer on the substrate prior to epitaxy should permit the growth of purer, more homogeneous Ge films, i.e., the relative influence of the substrate and the film will be minimized. In the present paper we attempt to determine whether this is in fact the case by investigating the properties of the transverse photovoltage.

2. The samples were heterostructures with linear dimensions of $12\times2\times0.3$ mm, similar to those usually used for photoelectric measurements.[2] As has been noted, a thin ($\sim$15 Å) oxide layer was formed on the GaAs substrate before growing a p-type Ge film of thickness $d=0.5$ μm with a concentration of $(5–7)\times10^{15}$ cm^{-3}. The technology used to grow these structures by molecular-beam epitaxy has been described in detail in Refs. 2 and 3.

Measurements were made of the distribution of the transverse voltage generated by moving a 0.5 mm-wide modulated monochromatic light probe along the sample. The use of a narrow light probe allowed us to increase the optical intensity incident per unit area of the sample to 6×10^{15} photons/ cm$^2\cdot$s and thus increase the amplitude of the experimentally measured photovoltage. In the experiments the direction of motion of the probe could be reversed and its velocity could be varied between 0.01 and 0.025 mm/s, the wavelength of the modulated ($\lambda^{\sim}$) and unmodulated light (λ^{-}) incident on the sample could be varied between 0.4 and 2.0 μm, and its intensity could also be varied in the range $2\times10^{13}–1\times10^{16}$ photons/cm$^2\cdot$s.

3. A characteristic feature of these photovoltage distribution curves is the dependence of their amplitude on the direction of motion of the probe, which is observed without any auxiliary unmodulated illumination (curves *1* and *2*, Fig. 1; the optical intensity in the probe was 6×10^{15} photons/ cm$^2\cdot$s). This dependence can be identified particularly clearly on the distribution of the voltage generated by light near the GaAs absorption edge ($\lambda=0.88$ μm). The difference between the distribution curves of the voltage obtained for opposite directions of motion of the probe decreases with decreasing wavelength as far as 0.68 μm and with increasing wavelength up to $\lambda\geqslant0.38$ μm. The physical reasons for this difference are known and have been described in the literature.[4,5] They are associated with the long-term relaxation of the residual conductivity formed in the illuminated section of the sample and are caused by recombination drift

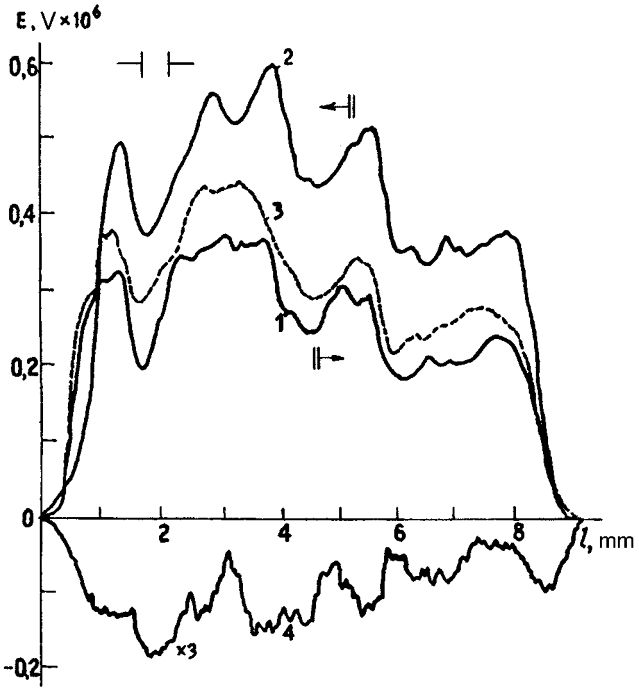

FIG. 1. Transverse photovoltage distribution in the sample when the probe is moved in one directions and then the other (the sample is illuminated on the side with the Ge film): *1, 2* — $\lambda^{\sim}=0.88$ μm (no unmodulated illumination), *3* — $\lambda^{\sim}=0.88$ μm, $\lambda^{-}=0.86\mu$m unmodulated illumination, and *4* — $\lambda^{\sim}=0.91$ μm, $\lambda^{-}=0.86\mu$m unmodulated illumination.

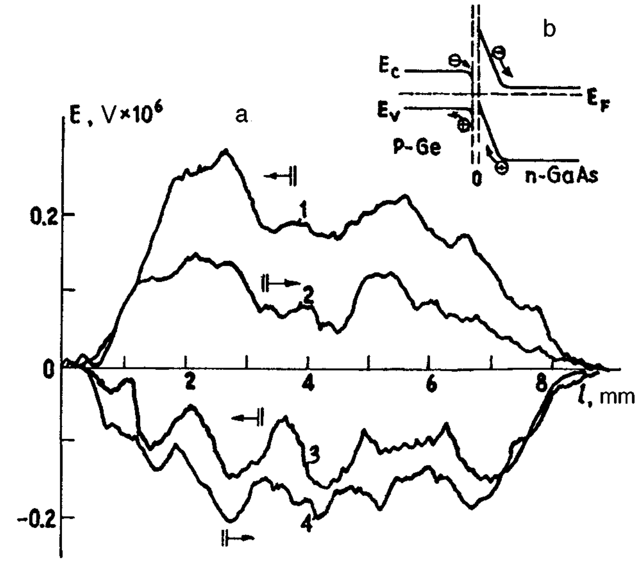

FIG. 2. Distribution of the transverse photovoltage in the sample (illuminated on the side with the GaAs substrate): *1, 2* — $\lambda^{\sim}=0.88$ μm, *3, 4* — $\lambda^{\sim}=0.91$ μm.

barriers for the nonequilibrium carriers, which may be localized on the surface or in the bulk of the semiconductor. In the present case, the characteristics of the voltage distribution described above indicate that the recombination-drift barriers responsible for the long-term relaxation of the voltage are localized in the GaAs substrate, and, more precisely, in the layer immediately adjacent to the Ge film. These characteristics are typically absent for heterostructure samples grown on substrates without oxides on the surface.

4. Curves *3* and *4* in Fig. 1 show the distributions of the photovoltage along a sample illuminated with both modulated and unmodulated light from the side with the germanium film. The entire sample was exposed to $\lambda^{-}=0.86$ μm unmodulated light with an intensity $N=4.1\times10^{15}$ photon/cm$^2\cdot$s. An optical probe of $\lambda^{\sim}=0.88$ μm modulated light was moved from one end to the other along a sample with darkened contacts at a velocity of 0.025 mm/s (curve *3*, Fig. 1). The distribution of the voltage remained the same when the direction of motion of the optical probe was reversed. However, changing the wavelength of the exciting modulated radiation to $\lambda^{\sim}=0.91$ μm caused a change in the distribution profile of the voltage and in its polarity (curve *4*, Fig. 1). In addition, the distribution of the voltage did not depend on the direction of motion of the probe. The voltage described by curve *4* is clearly generated in the Ge film because the energy of the exciting photons is less than the GaAs band gap. At the same time, curve *1* describes the distribution of a voltage generated preferentially in the GaAs, since its amplitude in the Ge is an order of magnitude lower and its contribution to the total voltage is small.

It has been noted that the mechanism for the generation of the photovoltage is associated with the presence of dark resistivity gradients in the film and the substrate. The reversal of the polarity of the voltage when the wavelength of the exciting light passes the GaAs absorption edge is a direct consequence of the fact that these gradients in the film and the substrate are in opposite directions. This conclusion was reached previously in analyses of the spectral characteristics of the transverse photovoltage measured for heterostructure samples grown by molecular-beam epitaxy on the arsenic-stabilized surface of a GaAs substrate (without an oxide layer), and also for samples grown by vacuum evaporation.

It is interesting to note that as λ decreases (and therefore the energy of the exciting photons and the absorption coefficient in Ge increase), the character of the voltage distribution changes, since it is essentially the algebraic sum of the voltages generated in the film and the substrate. In addition, the amplitudes of these voltages are equalized as a result of a reduction in the amount of light passing through the Ge film and being absorbed by the substrate, $I=I_0\exp(-\alpha d)$, and their contribution to the measured signal naturally changes.

5. Additional data indicating that the barriers are localized was obtained by studying the photovoltage distribution when the heterostructure sample was illuminated from the side with the GaAs substrate (Fig. 2a). These investigations showed that first, the polarity of the voltage is reversed when the wavelength of the modulated light changes from $\lambda^{\sim}=0.88$ μm (curves *3* and *4*, Fig. 2a) to $\lambda^{\sim}=0.91$ μm (curves *1* and *2*, Fig. 2a), as is observed when the sample is illuminated on the side with the Ge film. Second, the auxiliary illumination also leads to the disappearance of the long-term relaxation of the voltage and has a selective effect on the measured signal.

Compared with illumination on the film side, the amplitude of the voltage is five times greater at $\lambda=0.91$ μm, while the voltage generated by the $\lambda=0.88$ μm light is reduced by a factor of 3, mainly because of the increased amount of absorbed light in the Ge film and the reduced fraction in the GaAs substrate near their interface.[6–8] It should be stressed that most of the amplitude of the voltage is formed precisely in this place.

6. The heterostructure samples under study have a layer of oxide between the film and the substrate, which alters the band diagram of the heterojunction. This model assumes that a depletion layer (to the point of inversion) is formed in the GaAs at the boundary with the oxide layer, and on the other side, an accumulation or depletion layer is formed in the Ge Ref. 9 (Fig. 2b). The oxide forms a natural barrier for the charge carriers between the film and the substrate. The photogenerated electron-hole pairs are spatially separated in the band-bending regions in GaAs and Ge, respectively. The oxide partially impedes the transfer of excess carriers from the substrate into the film. This spatial separation of the nonequilibrium carriers is also responsible for the additional voltage generated in addition to the bulk-gradient voltage, as the light probe moves along the interface. If fairly strong depleting band bending occurs in the Ge, this voltage is generated in the film even at room temperature, as was observed experimentally (Fig. 2a, curves *3* and *4*). This voltage will obviously disappear in the presence of auxiliary illumination, which generates electron-hole pairs in the band-bending zone in GaAs and Ge, thereby screening it.

Mention should be made of another important characteristic deduced from a comparison of the amplitudes of curves *1* and *2* (Fig. 1) with curve *3* (Fig. 2). The amplitude of this last curve *3*, describing the distribution of the photovoltage at each point in the sample, should clearly equal the half-sum of the amplitudes of curves *1* and *2* (Fig. 1). This is because the amplitude of the voltage associated with the long-term relaxation of the nonequilibrium conductivity, which is algebraically added to the bulk-gradient voltage, does not change in magnitude but only in sign as the direction of motion of the probe is reversed (provided that its velocity remains constant). However, it can be seen that the amplitude of curve *1* (Fig. 2) describing the distribution of the voltage with auxiliary illumination is less than this half-sum.

This difference can be attributed to an additional voltage at the modulation frequency, induced by the photoconductivity in the sample. Continuous high-intensity illumination generates a bulk-gradient voltage that is constant in time (unmodulated) and thus creates an additional static field in the sample. When the sample is exposed to modulated light from the fundamental absorption region of Ge and GaAs, a voltage[10]

$$E^{-}-VR\Delta\sigma \tag{1}$$

will be generated in this field, where V is the voltage from the continuous illumination, R is the resistance of the illuminated part of the sample, and $\delta\sigma$ is the photoconductivity excited by the modulated radiation.

Thus, the experimentally measured amplitude of the voltage will be smaller and given by

$$E=E^{\sim}-VR\Delta\sigma, \tag{2}$$

where $E^{\sim}$ is the bulk-gradient voltage generated in the sample in the absence of unmodulated auxiliary illumination.

7. Various conclusions can be drawn from these experiments and results.

The gradients of the carrier dark concentrations along the interface are in opposite directions in the substrate and the film.

The presence of an oxide layer between the film and the substrate leads to spatially separated band bending in the Ge and GaAs, which is responsible for generating an additional voltage that relaxes slowly with time and depends on the velocity and direction of motion of the light probe.

It was noted initially that long-term relaxation of the photovoltage has also been observed in heterostructures grown by thermal vacuum evaporation. However, this behavior was attributed to the presence of recombination-drift barriers formed in adjacent layers of film as a result of their high doping. A similar voltage is observed in heterostructure samples with an oxide layer between the film and the substrate, but in this case, the barriers are localized on the surfaces of the film and the substrate on either side of the oxide.

The reason for the low amplitude of the photovoltage in these heterostructures is clear. Although the Ge films are purer than those grown on substrates without an oxide layer, the recombination velocity increases at the surface adjacent to the oxide, which significantly reduces the amplitude of the photovoltage in thin samples, even when the coefficients of absorption of light in the Ge are high.

This work was partly financed by the Ukrainian State Fund for Fundamental Research (Project No. 621/2-96)

[1] L. V. Shekhovtsov, A. V. Sachenko, and Yu. M. Shvarts, Fiz. Tekh. Poluprovodn. **29**, 566 (1995) [Semiconductors **29**, 293 (1995)].

[2] G. N. Semenova, T. G. Kryshtab, L. V. Shekhovtsov, and Yu. G. Sadof'ev, Pis'ma Zh. Tekh. Fiz. **22**(5), 75 (1996) [Tech. Phys. Lett. **22**, 215 (1996)].

[3] Yu. G. Sadof'ev, Pis'ma Zh. Tekh. Fiz. **19**(10), 5 (1993) [Tech. Phys. Lett. **19**, 296 (1993)].

[4] M. K. Sheĭnkman and A. Ya. Shik, Fiz. Tekh. Poluprovodn. **10**, 209 (1976) [Sov. Phys. Semicond. **10**, (1976)].

[5] N. P. Zhad'ko, A. D. Kucheruk, V. A. Romanov, B. K. Serdega, and L. V. Shekhovtsov, Ukr. Fiz. Zh. **27**, 622 (1982).

[6] M. D. Sturge, Phys. Rev. **127**, 768 (1962).

[7] W. C. Dash and R. Newman, Phys. Rev. **99**, 1151 (1955).

[8] D. E. Aspnes and A. A. Studna, Phys. Rev. B **27**, 985 (1983).

[9] F. C. Jain, J. Vac. Sci. Technol. B **1**, 661 (1983).

[10] S. M Ryvkin, *Photoelectric Effects in Semiconductors* [in Russian] (Fizmatgiz, Moscow, 1963).

Translated by R. M. Durham

Fresnel vector diffraction integral

Sh. D. Kakichashvili

Institute of Cybernetics, Academy of Sciences, Tbilisi, Georgia

(Submitted December 24, 1996)
Pis'ma Zh. Tekh. Fiz. **23**, 42–46 (June 12, 1997)

The Huygens-Fresnel principle modified for electromagnetic waves is used to achieve matching by generalizing the wave number to a complex value. In this way, it is possible to describe the field directly beyond a diffracting object. © *1997 American Institute of Physics.* [S1063-7850(97)00806-9]

A diffraction integral based on the Huygens-Fresnel principle modified for electromagnetic waves was analyzed in Ref. 1. In the present study, integration over a complex section in the direction of propagation of the initial wave is introduced to match the amplitude of the final expression with that of a freely propagating plane wave.

In this study, a modification of the Huygens-Fresnel principle is used to perform similar matching by generalizing the wave number to a complex value. By this means it is possible to describe the field directly beyond a diffracting object.

We write the coordinate part of this diffraction integral, also using a representation of the secondary spherical wave in the form ($\exp - i\varkappa r / - i\varkappa r$), used for the first time in Ref. 2

$$\vec{\mathbf{E}}(x,y,z) = k \int\int_{S_0} \mathbf{R}(l,m,n)\mathbf{P}(l,m,n)\mathbf{M}(x_0,y_0)\vec{\mathbf{E}}_0 \exp - i\varkappa z_0 \frac{\exp - i\hat{x}r}{-i\hat{\varkappa}r} dx_0 dy_0 . \tag{1}$$

Here, $k = 24/\pi^2$, $\varkappa = 2\pi/\lambda$, and $\hat{\varkappa} = \varkappa' + i\varkappa''$ is the complex wave number associated with the secondary wave. The values of the components $\varkappa' = 2\pi/\lambda'$ and $\varkappa'' = 2\pi/\lambda''$ are determined by solving a matching equation analyzed subsequently (see Eq. (4)), x, y, and z are the coordinates of the observation point, and x_0, y_0, and z_0 are the coordinates of the point on the diffracting object. Integration is performed over the region S_0 occupied by the object, $\vec{\mathbf{E}}(x,y,z)$ is the three-dimensional Jones vector[3] of the diffracted wave, $\vec{\mathbf{E}}_0$ is the Jones vector of the illuminating wave (to simplify the following analysis, the illuminating wave is taken as a plane wave propagating along the z axis), $\mathbf{M}(x_0,y_0)$ is the Jones matrix[3] of the diffracting object, $l = (x - x_0)/r$, $m = (y - y_0)/r$, and $n = (z - z_0)/r$ are the direction cosines of the diffracted beam, and $\mathbf{R}(l,m,n)$ and $\mathbf{P}(l,m,n)$ are the so-called rotation and projection matrices, whose combined action describes the evolution of the amplitude and polarization of the secondary wave as functions of the direction of diffraction. We write an expression for these matrices in a more compact and corrected form compared with Ref. 1:

$$\mathbf{RP} = \begin{pmatrix} n + \frac{m^2}{1+n} & -\frac{lm}{1+n} & l \\ -\frac{lm}{1+n} & n + \frac{l^2}{1+n} & m \\ -l & -m & n \end{pmatrix} \times \begin{pmatrix} \sqrt{1-l^2} & 0 & 0 \\ 0 & \sqrt{1-m^2} & 0 \\ 0 & 0 & \sqrt{1-n^2} \end{pmatrix} . \tag{2}$$

In accordance with the Huygens-Fresnel principle, each point on the initial wavefront is a source of a real secondary wave. This approach necessarily requires initial matching between the amplitudes of the secondary and initial waves. Then the total amplitude of the secondary wave in all directions in the absence of a diffracting object (the corresponding Jones matrix is $\mathbf{M}(x_0,y_0) = (\begin{smallmatrix} 1 & 0 \\ 0 & 1 \end{smallmatrix})$) must be equal to the amplitude at the corresponding point on the initial wavefront:

$$\int\int\int \mathbf{R}(l,m,n) \cdot \mathbf{P}(l,m,n)\vec{\mathbf{E}}_0 \frac{\exp - i\hat{\varkappa}r}{-i\hat{\varkappa}r} dl\,dm\,dn = \vec{\mathbf{E}}_0 . \tag{3}$$

At the front, where $r \rightarrow 0$, the real part of the secondary wave amplitude is $\mathrm{Re}[(\exp - i\hat{r})/-i\hat{\varkappa}r] \rightarrow 1$ regardless of the value of the components of the complex wave number $\hat{\varkappa}$. Under these conditions, the solution (3) shows that the threefold integrals of the corresponding elements of the matrix product **RP** are only nonzero for diagonal elements and are equal to $\pi^2/24$. Thus, it is found that the resultant amplitude of the secondary wave is not equal to the amplitude of the initial wave. The coefficient k introduced in Eq. (1) performs the necessary correction for this mismatch.

We determine the components of the complex wave number, $\varkappa'$ and $\varkappa''$, by solving Eq. (1) in the asymptotic approximation for a freely propagating plane wave. Selecting the critical points $x_0 = x$ and $y_0 = y$ (Ref. 4) allows us to calculate the asymptotic approximation in the form

$$\vec{\mathbf{E}} = \frac{2\pi k}{\varkappa' \hat{\varkappa}} \vec{\mathbf{E}}_0 \exp - i[\varkappa z_0 + \hat{\varkappa}(z - z_0)]. \tag{1'}$$

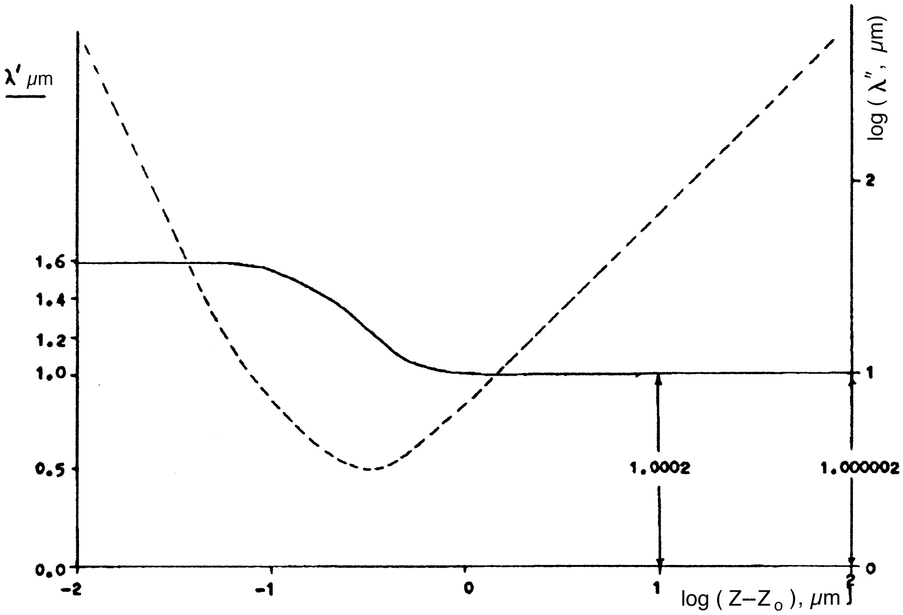

FIG. 1.

The left-hand side of Eq. (1′) is *a priori* equal to $\vec{\mathbf{E}}_0 \exp(-i\varkappa z)$, which allows us to construct a single complex equation for both components of the Jones vector $\vec{\mathbf{E}}_0$:

$$2\pi k \exp[\varkappa''(z-z_0)]\exp - i[(\varkappa'-\varkappa)(z-z_0)] - \varkappa'(\varkappa'+i\varkappa'')=0. \tag{4}$$

Dividing Eq. (4) by the real and imaginary parts, for given $\varkappa$ and k, we can express $\varkappa'$ and $\varkappa''$ as functions of the distance $(z-z_0)$.

Figure 1 shows the behavior of λ' as a function of $(z-z_0)$ for $\lambda = 1\,\mu$m. With increasing distance, λ' rapidly approaches λ and for $(z-z_0)\approx 10^2$–10^4 μm, they are accurately matched. It should be noted that λ' differs substantially from λ only in the immediate vicinity of the source, at distances much less than λ where, strictly speaking, the secondary wave is formed and the concept of wavelength loses some of its meaning. It is usually difficult to obtain a unique and adequate description of this region.[5] Generally speaking, it seems to the author that at present, it is questionable whether any difference between λ' and λ can be observed experimentally. However, a suitably designed experiment is obviously required to provide a clear substantiation of this complex wave number hypothesis. The imaginary part $\varkappa''$ of the complex wave number only plays an auxiliary role and clearly cannot be related to any real wave. In Fig. 1 the profile of λ'' is indicated by the dashed curve.

We also note that the complex equation (4) is satisfied by a whole system of other roots, whose meaning and physical content require further analysis.

If the asymptotic approximation is also used to describe the field at the diffracting object, then replacing $\vec{\mathbf{E}}_0$ with $\mathbf{M}(x_0,y_0)\vec{\mathbf{E}}_0$ and setting $(z-z_0)=0$, we obtain $\varkappa'=\sqrt{2\pi k}$ and $\varkappa''=0$, which after substituting into Eq. (1′), gives

$$\vec{\mathbf{E}}=\mathbf{M}(x_0,y_0)\vec{\mathbf{E}} \exp - i\varkappa z, \tag{1''}$$

which uniquely describes the amplitude-phase component of the vector field immediately beyond a diffracting object having an arbitrary anisotropic gyrotropic structure.

The need to generalize the wave number to a complex value, demonstrated in this study, is perhaps the only alternative in this scenario. For example, it has been known for some time that the Fresnel diffraction integral for a freely propagating wave gives rise to a factor of dimension length that prevents it from being assigned any real physical meaning. Similar reasoning also applies to the Kirchhoff diffraction integral if its accurate form, derived uniquely from Green's theorem and the wave equation,[6] is used rather than an approximate form. Fundamental difficulties are also involved in developing Young's diffraction idea.[7]

Under these conditions, it should be recognized that the systematic application of the Huygens-Fresnel principle asserts that the secondary wave is a real physical entity with specific characteristics of nucleation and formation, rather than as a virtual mathematical transform figuring in the theory.[8]

[1] Sh. D. Kakichashvili, Pis'ma Zh. Tekh. Fiz. **22**(5), 66 (1996) [Tech. Phys. Lett. **22**, 211 (1996)].

[2] A. Sommerfeld, *Partial Differential Equations in Physics*, transl. from the German (Academic Press, New York, 1964) [Russ. transl., IL, Moscow, 1950].

[3] W. A. Shucliff, *Polarized Light: Production and Use* (Harvard University Press, Cambridge, Mass., 1962) [Russ. transl., Mir, Moscow, 1965].

[4] M. Born and E. Wolf *Principles of Optics*, 4th ed. (Pergamon Press, Oxford, 1969) [Russ. transl., Nauka, Moscow, 1979].

[5] H. G. Schmidt-Weinmar, in *Inverse Source Problems in Optics*, edited by H. P. Baltes (Springer-Verlag, Berlin, 1978) [Russ. transl., Mir, Moscow, 1964].

[6] G. Kirchhoff, *Theory of Light Rays*, in *Selected Works of Gustav Robert Kirchhoff* [in Russian], Nauka, Moscow (1988).

[7] A. Rubinovich, *Thomas Young and Diffraction Theory. Creators of Physical Optics*, edited by V. I. Rodichev [in Russian], Nauka, Moscow (1973).

[8] A. Sommerfeld, *Optics*, transl. from the German (Academic Press, New York, 1954) [Russ. transl., IL, Moscow, 1953].

Translated by R. M. Durham

Influence of the magnetic self-field on the formation of a cathode plasma jet in steady-state vacuum arcs

I. A. Krinberg and E. A. Zverev

Irkutsk State University

(Submitted July 23, 1996)
Pis'ma Zh. Tekh. Fiz. **23**, 47–53 (June 12, 1997)

It is shown that magnetic pinching of a cathode plasma jet is initiated after various microjets have merged to form a single jet at a distance $r > 10^3 d$ from the cathode (d is the diameter of the cathode microspot). The plasma jet acquires the form of a paraboloid of revolution whose surface oscillates about the equilibrium position because of the inertia of the plasma transverse motion. At this point, cooling of the jet ceases. © *1997 American Institute of Physics.* [S1063-7850(97)00906-3]

1. It is known that a plasma formed in the cathode microspots of a vacuum arc discharge propagates toward the anode in the form of current-carrying plasma jets with a quite clearly defined lateral boundary.[1] It is usually assumed[1,2] that the plasma kinetic pressure $P = N_e T_e + N_i T_i$ is equalized at this boundary by transverse pinching of the cathode plasma jet by the magnetic self-field. In this case, the Bennett equilibrium condition[3] $\beta = 2c^2 \overline{P} S / I^2 = 1$, obtained for an arbitrary distribution of pressure and current in the cross section $S = \pi d^2/4$ of the plasma cylinder (where $\overline{P}$ is the average pressure, I is the current, and c is the velocity of light), should be approximately satisfied. However, near the cathode, where the diameter of the microjet is of the order of the size of the cathode microspot $d \simeq 1\,\mu$m, we find $\beta \geqslant 10^2$ (the kinetic pressure is substantially greater than the magnetic pressure), since measurements of the electron density and pressure near the cathode give $N_e \simeq 10^{21}$ cm^{-3}, $T_e \approx$ 5–10 eV (Refs. 4–6), $I/d \approx 10^5$ A/cm (estimated from the Zeeman effect[7]), and the ion parameters (with average charge Z) are estimated as $N_i = N_e / Z$ and $T_i < T_e$.

We show here that magnetic pinching only begins to have an influence after the various microjets have merged to form a single cathode plasma jet at a distance $r > 10^3 d$ from the cathode. Ultimately, the cathode plasma jet acquires the form of a paraboloid of revolution whose surface oscillates about the equilibrium position ($\beta = 1$) because of the inertia of the plasma transverse motion. At this point, cooling of the cathode plasma jet ceases, which explains the constant electron temperature observed at large distances (r = 5–40 cm) from the cathode.[1,8]

2. In the initial section of the jet, where $\beta \gg 1$, transverse expansion is impeded by friction between the plasma and the neutral gas surrounding the plasma and propagates mainly along the surface of the cathode.[9] We shall assume that when $\beta > 1$, the cathode plasma undergoes spherical expansion within a cone with the solid angle $\Omega_0 = 2\pi(1 - \cos\alpha_0) = \text{const}$ (whose size is determined by the interaction with the neutral gas) and the cross sectional area of the jet varies as $S(r) = \Omega_0 r^2$. Since the ratio of the electron and ion currents is $I_e / I_i = \gamma \approx 10$ (Ref. 9), under conditions of steady-state quasineutrality we have $V_e = \gamma V$ and $I \approx \gamma e N_e V S$, where V_e and V are the electron and ion radial velocities. Assuming $T_e \gg T_i$ (Ref. 10), we have $P \approx T_e N_e$ and $\beta = 2c^2 T_e / (\gamma e V I)$. It was shown in Refs. 6, 10, and 11 that as a current-carrying plasma undergoes spherical expansion, it is accelerated to supersonic velocity $V_* = (5ZT_*/3m)^{1/2}$ at a distance $\Delta r = r_* - r_0 \simeq d/4$ from the cathode, and for $r > 10^2 d$, the velocity reaches the limiting value $V_\infty \approx 5V_*$ (the asterisk subscript indicates the values of the variables are taken at the critical point r_*, r_0 is the position of the cathode surface, and m is the ion mass). Thus, the parameter β will decrease only as a result of cooling of the plasma. Since $\beta = \beta_* T_e V_* / (T_* V)$, for $\beta_* \simeq 10^2$ the value $\beta \simeq 1$ is achieved at a distance $r_1 \geqslant 10^3 d$, where $T_e / T_* \approx 0.1$ (Ref. 10). Further cooling of the plasma as a result of expansion causes the magnetic pressure to exceed the kinetic pressure ($\beta < 1$), and the plasma is accelerated toward the axis of the jet. The characteristics of this process depend to a great extent on the vertex half-angle α_0 of the jet and the parameter β_*.

3. We shall take into account the influence of the magnetic field starting from $r = r_1$. We use a one-dimensional approximation, considering the cathode plasma jet to be of variable cross section $S(r)$. We shall assume that $T_e(r)$, $V(r)$, and $j(r) = I/S$ are constant over the cross section, but that the particle density $N \equiv N_i = N_e / Z$ and the velocity $V_\theta = r\dot{\theta}$ depend on the polar angle θ (in the spherical coordinate system r, θ, φ), setting $N = 0$ at the boundary of the jet ($\theta = \alpha$). We shall also assume that $V_\theta \ll V$, i.e., that the lateral surface of the jet is nearly conical with a slowly varying vertex half-angle α. In this case, $d/dt = V d/dr$ and $\dot{\alpha} = V d\alpha / dr$.

Under these assumptions, the system of equations obtained in Ref. 10 for $V(r)$, $T(r)$, and the potential $\Phi(r)$ retain their form and should merely be supplemented by an equation for the cross sectional area $S(r) = 2\pi r^2 (1 - \cos\alpha(r))$. For this purpose, we consider the θ-projection of the equation of plasma motion

$$\frac{mNV}{r} \frac{\partial}{\partial r}(r^2 \dot{\theta}) = -\frac{1}{r} \frac{\partial P}{\partial \theta} - \frac{jB}{c}. \tag{1}$$

Since the compression rate $\dot{\theta}$ has a maximum and is equal to $\dot{\alpha}$ at the lateral boundary of the jet and $\dot{\theta} = 0$ on the axis, the

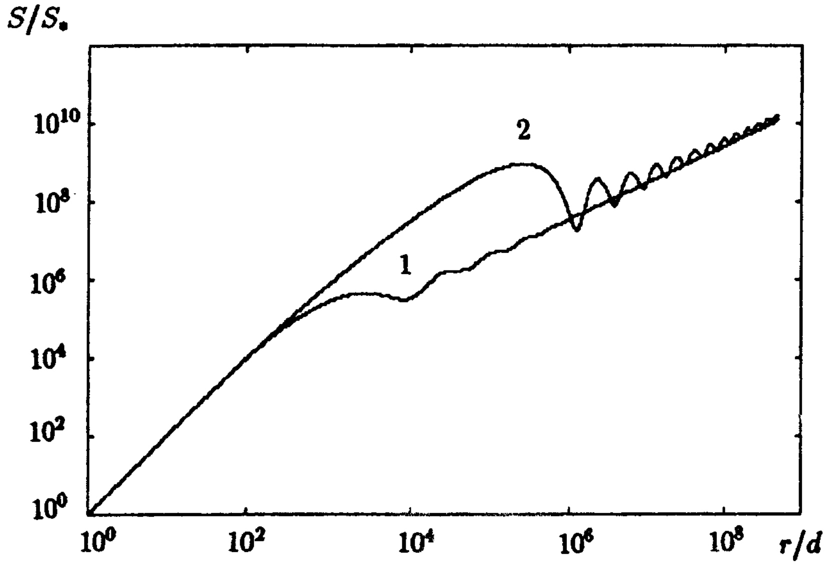

FIG. 1. Variation of the cross sectional area of a cathode plasma jet with distance along axis: *1* — calculated for $\alpha_0 = \pi/6$ and *2* — calculated for $\alpha_0 = \pi/3$.

extremely simple self-similar approximation $\dot{\theta} = \dot{\alpha}\theta/\alpha$ may be used. Then, multiplying Eq. (1) by $1-\cos\theta$ and integrating over θ between 0 and α, we find

$$f(\alpha) m \overline{N} V \frac{d}{dr}\left(r^2 \frac{\dot{\alpha}}{\alpha}\right) = \overline{P} = \frac{I^2}{2c^2 S} \tag{2}$$

where $f(\alpha) = \int_0^\alpha N(\theta)(1-\cos\theta)\theta d\theta / \int_0^\alpha (N(\theta)\sin\theta d\theta$, $\overline{P} = Z\overline{NT}_e$, and N is the average ion density. The last term in Eq. (2) was obtained using the Maxwell equation $\nabla \times \mathbf{B} = 4\pi \mathbf{j}/c$, where $j = j_r = I/S$, and it was also assumed that the condition $\sin^2\alpha/2 \ll 1$ is satisfied for $\alpha < \pi/3$. It can seen from Eq. (2) that the equilibrium condition $(\dot{\alpha} = 0)$ for a conical jet coincides with the Bennett condition $(\beta = 1)$ for a cylinder, but is subject to additional constraints ($j = \text{const}$ and constraints on the angle α).

Converting, as in Refs. 10 and 11, to the dimensionless variables $x = r/r_*$ (where $r_* \simeq d$) (Ref. 11), $s = S/s_* = x^2(1-\cos\alpha)/1(1-\cos\alpha_0)$, $v = V/V_*$, and $t = T_e/T_*$, we obtain

$$\frac{5}{3} f(\alpha) \frac{d}{dx}\left(\frac{x^2 v}{\alpha} \frac{d\alpha}{dx}\right) = \frac{t}{v} - \frac{1}{\beta_*}. \tag{3}$$

The function $f(\alpha)$ depends weakly on the relative particle density distribution $N(\theta)$ over the cross section of the jet and is close to the form $f \approx k\alpha^2$. For $N = \text{const}$ when $\theta < \alpha$ and $N = 0$ when $\theta \geqslant \alpha$, we have $k \approx 1/4$. For $N = N_0(1-\theta^2/\alpha^2)$ or $N = N_0(1-\sin^2\theta/\sin^2\alpha)$ we obtain $k \approx 1/6$, which was used in the following calculations.

Equation (3) is solved jointly with the equations for v and t (Ref. 10) subject to the boundary conditions $\alpha = \alpha_0$ and $d\alpha/dx = 0$ for $x = x_1$ (where $v(x_1)/t(x_1) = \beta_*$).

4. A solution was first obtained for an elementary cathode microjet transporting the current $I \simeq$ 1–10 A (Refs. 6, 7, and 12) with $d \simeq$ 0.3–3 μm (Refs. 4, 6, and 7) and $\beta_* \geqslant 10^2$. It was found that magnetic pinching of this jet only becomes appreciable for $r > 10^7$ μm $\simeq 10$ m, i.e., at unrealistically large distances. From this we conclude that the magnetic self-field does not play a significant role in low-current vacuum arcs with a total current $I_a \simeq$ 1–30 A.

At high currents I_a, the plasma is emitted from separate microspots, and at the initial stage $r \leqslant D$ there are $n = I_a/I$ independent current-carrying microjets (here $D \simeq$ (3–30)d is the distance between the microspots[12,13]). It may be assumed that the microjets merge to form a single cathode plasma jet with the current $I_a = nI$ and the total cross sectional area $S_a \simeq nS$ at the distance $r \simeq D$, where the plasma velocity is already close to the limiting supersonic velocity $V_\infty \approx 5V_* \simeq 10^4$ m/s, and the temperature has decreased only to $T \simeq 2/3T_*$ (Ref. 10). Since $\beta \sim S/I^2$, for the total jet we have $\beta_a \simeq \beta/n$.

By way of example, Figs. 1 and 2 give solutions of Eq. (3) (and the equations for v and t) with $\beta_* = \beta_a = 10$, which approximately corresponds to $n = 10$ and $I_a \simeq 30-100$ A. In the range $x < 30$, where $t/v \gg 1/\beta_*$, the solution gives the change in the parameters of an individual microjet with the dimensionless distance $x = r/d$. The range $x > 10^3$, where $t/v \approx 1/\beta_*$, corresponds to the solution for the complete cathode plasma jet. In the transition range of x values, the individual microjets merge to form a complete cathode plasma jet, which, naturally, is not described by Eq. (3). However, the plasma temperature and velocity vary comparatively little in this section, so that the overall pattern of variation in the parameters of the cathode plasma jet is conserved in this approximate method of calculation.

Figure 1 shows that magnetic pinching initially reduces the cross section of the jet, which then shows an average increase, which however, is not proportional to r^2 (spherical expansion) but to r, i.e., the lateral surface of the cathode plasma jet acquires the form of a paraboloid of revolution. It can be seen from Fig. 2 that a rapid fall in the electron temperature (corresponding to free spherical expansion) is replaced by a rise to an approximately constant value $T_e \approx 0.4T_*$. This change in the electron temperature agrees well with the experimental results, since according to estimates made using the ion composition (which yield values

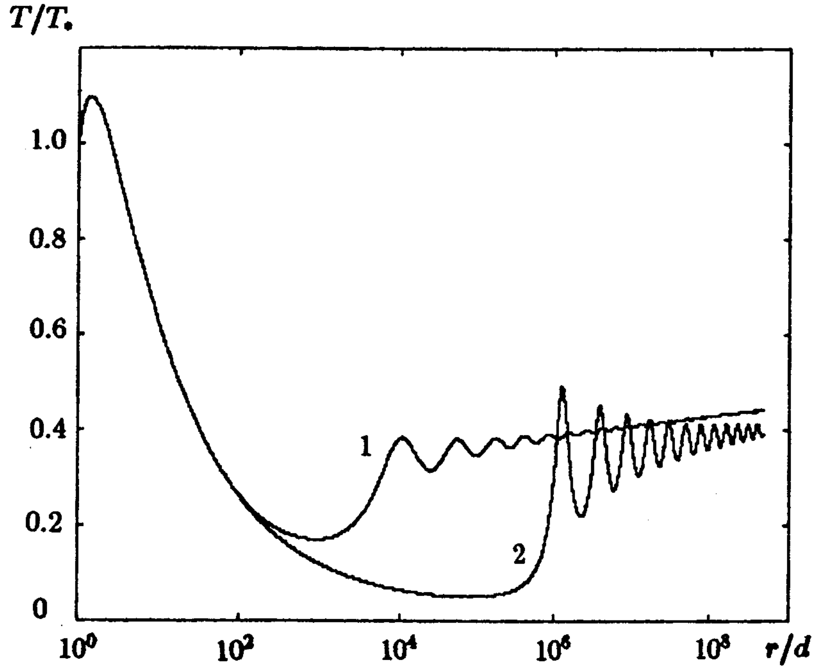

FIG. 2. Variation of the electron temperature along the axis of a cathode plasma jet (notation as in Fig. 1).

for the cathode region where $T_e \approx T_* \approx T_{\max}$) $T_e \approx 10$ eV (Mo) and $T_e \approx 4$ eV(Ti) (Ref. 6), whereas probe measurements far from the cathode give $T_e \approx 3$ eV (Mo, $r = 15–40$ cm) and $T_* \approx 1.3$ eV (Ti, $r = 5–40$ cm) (Ref. 8).

These model calculations have shown that when the magnetic pressure exceeds the gas pressure, the plasma is accelerated in the direction of the axis of the cathode plasma jet. The inertia of the transverse motion gives rise to periodic compression and expansion of the plasma, accompanied by temperature fluctuations. This process is similar to the radial oscillations of a cylindrical plasma in a Z-pinch.[14] Unlike the latter, the cathode plasma jet as a whole remains steady-state and transverse compression and expansion are observed only for individual sections of the plasma as they move along the jet. The electron temperature T_e and the longitudinal ion velocity V remain almost constant, increasing by only a few percent when the distance from the cathode varies by several orders of magnitude. Magnetic pinching causes appreciable acceleration of the ions only in the case of a non-steady-state cathode plasma jet with rising current I_a (Ref. 15).

[1] V. M. Lunev, V. M. Ovcharenko, and V. M. Khoroshikh, Zh. Tekh. Fiz. **47**, 1486 (1977) [Sov. Phys. Tech. Phys. **22**, 855 (1977)].

[2] V. P. Afanas'ev, Zh. Tekh. Fiz. **62**(11), 72 (1992) [Sov. Phys. Tech. Phys. **37**, 1081 (1992)].

[3] L. D. Landau and E. M. Lifshitz, *Electrodynamics of Continuous Media*, (Pergamon Press, Oxford, 1984) [Russ. original, Nauka, Moscow, 1982].

[4] A. Anders, S. Anders, B. Jüttner *et al.*, IEEE Trans. Plasma Sci. **PS-20**, 466 (1992).

[5] V. F. Puchkarev, J. Phys. D **24**, 685 (1991).

[6] I. A. Krinberg and M. P. Lukovnikova, J. Phys. D **28**, 711 (1995).

[7] N. Vogel and B. Jüttner, J. Phys. D **24**, 922 (1991).

[8] I. I. Aksenov, I. I. Konovalov, V. G. Padalka *et al.*, Fiz. Plazmy **11**, 1373 (1985) [Sov. J. Plasma Phys. **11** 787 (1985)].

[9] J. E. Daalder, Physica B+C **104**, 91 (1981).

[10] I. A. Krinberg, M. P. Lukovnikova, and V. L. Papernyĭ, Zh. Éksp. Teor. Fiz. **91**, 806 (1990) [Sov. Phys. JETP **70**, 451 (1990)].

[11] I. A. Krinberg Phys. Plasmas **1**, 2822 (1994).

[12] G. A. Mesyats and D. I. Proskurovsky, *Pulsed Electrical Discharges in Vacuum* (Springer-Verlag, Berlin, 1989) [Russ. original, Nauka, Novosibirsk, 1984].

[13] S. Anders, A. Anders, and B. Jüttner, J. Phys. D **25**, 1591 (1992) [*sic*].

[14] M. A. Leontovich and S. M. Osovets, At. Energ. No. 3, 81 (1956).

[15] I. A. Krinberg, J. Phys. D: Appl. Phys. **29**, 2049 (1996).

Translated by R. M. Durham

Local polarization reversal in $LiNbO_3$ crystals

S. O. Fregatov and A. B. Sherman

A. F. Ioffe Physicotechnical Institute, Russian Academy of Sciences, St. Petersburg

(Submitted February 10, 1997)
Pis'ma Zh. Tekh. Fiz. **23**, 54–58 (June 12, 1997)

Local polarization reversal has been investigated in a thin surface layer of a ferroelectric and preliminary results are presented for lithium niobate. The polarization reversal is accomplished by using a moving pointed electrode. © *1997 American Institute of Physics.* [S1063-7850(97)01006-9]

The aim of our investigations was to study local polarization reversal in a thin surface layer of a ferroelectric. Polarization reversal was achieved by using a moving pointed electrode, similar to the tip in a scanning tunneling microscope. An electric potential is applied to the tip, generating a local electric field sufficient for polarization reversal in a given region of the ferroelectric surface.

Single-domain lithium niobate crystals were selected for the investigations. Of the various ferroelectrics known to us, this uniaxial material has the strongest coercive field (≈ 20 kV/mm) and may incorporate domains with mutually opposed directions of spontaneous polarization, oriented along a specified axis (Z axis).

A single-crystal sample having characteristic dimensions of $3\times3\times0.5$ mm was placed on the surface of the first electrode — a conducting chromium film — deposited on the bottom of a shallow cell. A tungsten tip attached to a micromanipulator (the radius of curvature of the end of the tip did not exceed $1\,\mu$m), was brought close to the surface of the crystal. This tip serves as the second electrode and can be moved horizontally and vertically. To prevent electrical breakdown over the surface of the sample, the cell was filled with transformer oil.

This setup was used to study local polarization reversal for samples having different orientations of the Z axis. This was possible because in the immediate vicinity ($\approx 10\ \mu$m) of the end of the tip, the shape and position of the opposite electrode, positioned at a distance of hundreds of μm, have little influence on the structure of the electric field. The field lines in this region diverge from the tip in all directions within the solid angle $\approx 2\pi$.

The domain structures were revealed by chemical etching of the samples in a hot mixture of nitric and hydrofluoric acids (2:1). This method is based on the enhanced rate of etching near the domain wall.

Figure 1 shows one of the results of local polarization reversal in the surface region of a lithium niobate sample with the Z axis parallel to the surface. A uniformly polarized sample ≈ 1.5 mm thick with a polished surface was first etched using the above etchant to remove the damaged surface layer. As a result, the thickness of the sample was reduced by 20 μm. At room temperature the tip touching the surface of the sample was used to draw lines ≈ 1 mm long, with a specified spacing between them. The rate of displacement of the point of contact over the surface of the sample was ≈ 1 mm/s. Each line drawn corresponded to a particular potential difference (U) applied between the chromium layer and the tip. After the sample had been etched again, relief was revealed on the surface and was photographed in reflected light. Figure 1 shows the area of the surface adjacent to the line drawn at $U = 2750$ V.

Interference measurements of the depth of the etched regions indicated that each line drawn by the tip corresponds to a groove. At $U \geqslant 1550$ V it is noticeable that the groove bottoms are speckled with traces of needle-like domains, extending in a common direction. These needle-like domains

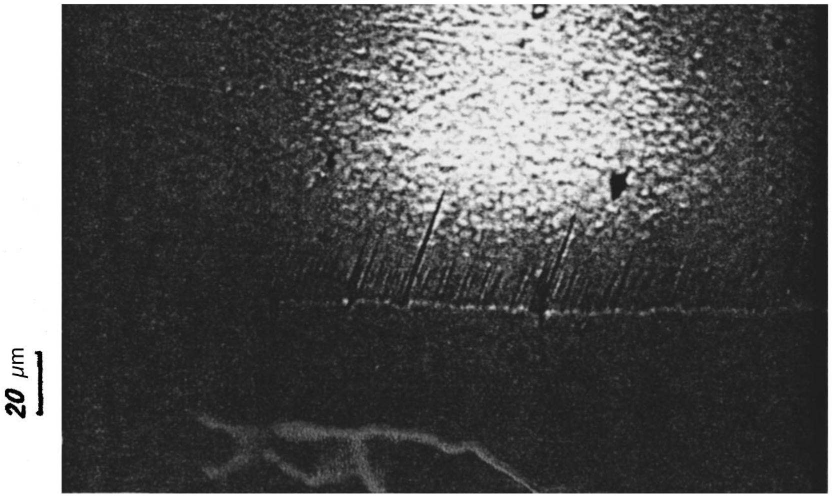

FIG. 1. Etched surface of sample at the point where a line is drawn at $U = 2750$ V.

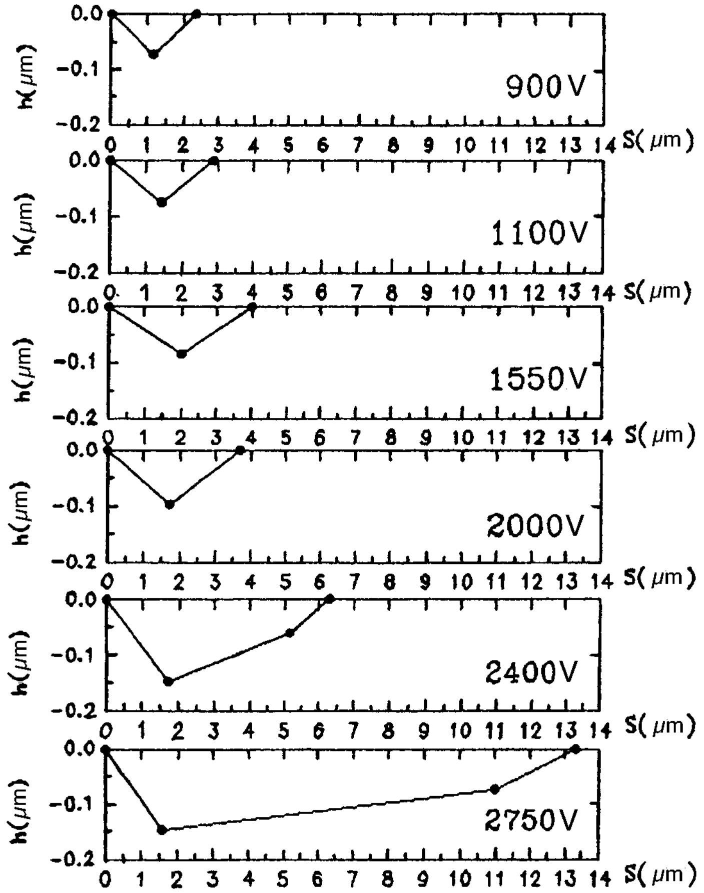

FIG. 2. Depth (h) of etched grooves versus distance (S) measured across grooves. Indicated on the diagrams are the values of U at which the lines were drawn.

were also recorded in experiments to study polarization reversal of MgO:LiNbO$_3$ in a uniform electric field.[1] The domains are oriented parallel to the Z axis. From the point of contact between the tip and the surface, the domains grow in the direction in which the planar component of the electric field of the tip induces polarization reversal of the ferroelectric. When the polarity of U is reversed, the domains grow in the opposite direction.

Figure 2 gives the depth h (in μm) of the etched regions as a function of the distance S (in mm) measured across the grooves. The origin for h is the level of the crystal surface and that for S is the edge of the groove facing the bases of the domains. An abrupt increase in the depth and width of the grooves is observed for potential differences $\geqslant$2400 V.

For these values of the potential difference, the depth of the etched regions did not exceed 0.15 μm. Polarization reversal evidently took place in a surface layer of around this thickness. The subsequent etching merely smooths the relief, negligibly influencing the depth of the grooves.

Different results were obtained for a lithium niobate sample with the Z axis perpendicular to the surface. In this case, local polarization reversal beneath the moving tip proceeds from the surface into the crystal. The etched surface clearly reveals regions of two parallel domain walls bordering on each domain formed along the trajectory of the moving tip. As the potential difference decreases from 2.75 to 0.9 kV, the domain width is reduced from $\approx$2 μm to less than 1 μm.

To sum up, these results have shown that by using a tip as one of the electrodes, local polarization reversal can easily be achieved even in a ''hard'' ferroelectric such as lithium niobate.

This effect can be as the basis to develop a microscale device that can write on the surface of ferroelectrics (''microplotter''). It can also be used to create domain structures in the surface region of a crystal for applications in nonlinear optics[2,3] (synchronization of second harmonic generation), acoustics[4] (electric-to-acoustic signal converters), and in other fields of solid-state physics.

The displacement of a tip over the surface of a ferroelectric can also be used for discrete recording of information. Unlike ferroelectric thin-film systems designed for use in various memory systems,[5] the ferroelectric medium in this case is homogeneous and its fabrication technology is simpler.

These results may be used as the basis for further research on the surface region of ferroelectrics and especially on the kinetics of domain formation and growth.

[1] A. Kuroda, S. Kurimura and U. Yosiaki, Appl. Phys. Lett. **69**, 1565 (1996).

[2] A. C. G. Nutt, V. Gopalan, and M. C. Gupta, Appl. Phys. Lett. **60**, 2828 (1992).

[3] Yong-yuan Zhu, Nai-ben Ming, Wen-hua Jiang, and Yong-an Shui, Appl. Phys. Lett. **53**, 1381 (1988).

[4] Shi-ning Zhu, Yong-yuan Zhu, Zhi-yong Zhang *et al.*, J. Appl. Phys. **77**, 5481 (1995).

[5] J. F. Scott and C. A. Paz de Araujo, Science **246**, 1400 (1989).

Translated by R. M. Durham

Hysteresis of the current-voltage characteristics of porous-silicon light-emitting structures

A. N. Laptev, A. V. Prokaznikov, and N. A. Rud'

Yaroslavl' State University

(Submitted November 27, 1996)
Pis'ma Zh. Tekh. Fiz. **23**, 59–65 (June 12, 1997)

A new hysteresis effect is described in metal–porous-silicon–p-type silicon structures and a new model is proposed to describe current flow in these structures. © *1997 American Institute of Physics.* [S1063-7850(97)01106-3]

Porous silicon has come to be regarded as a highly promising material for optoelectronics following the observation of intense visible photoluminescence[1] as well as electroluminescence from porous silicon structures.[2] However, the electroluminescence quantum efficiency of porous silicon structures is still fairly low (no higher than 10^{-3}), and thus in order to enhance this parameter it is important to gain a deeper understanding of the characteristics of the physical processes involved in current flow in electroluminescent cells, including metal–porous-silicon–crystalline-silicon (Me–PS–c-Si) structures.

In the present paper we report results of an investigation of current flow and photosensitivity in the 0.4–1.3 μm wavelength range in light-emitting Pd–PS–p-Si structures at room temperature.

The porous silicon structures were fabricated from (100)-oriented p-Si (KDB-10) wafers. Layers of porous silicon several μm thick were prepared by anodic electrochemical treatment in a 50% aqueous solution of HF. The porous silicon surface of the samples then underwent plasma-chemical treatment to remove the surface amorphized film before being covered with a semitransparent layer of Pd (20 nm thick). The Ohmic contacts were formed by an Al layer several μm thick, which partially covered the Pd layer and was deposited on the back side of the crystalline silicon (see inset to Fig. 1).

The static current-voltage characteristics of these structure exhibited well-defined rectifying behavior. The ratio of the forward and reverse currents (the forward current corresponded to the application of a positive potential to the c-Si) at a 2 V bias varied from one sample to another between a few units and 10^2. Typical current-voltage characteristics for our structures are plotted in Fig. 1. It should be noted that no saturation of the reverse current was observed for any of the structures. Moreover, for most structures the reverse current increased linearly with increasing bias. Likewise, no saturation of the reverse current was observed in Refs. 3 and 4 in an investigation of the current-voltage characteristics of Al–PS–p-Si structures. The authors of these studies analyzed their results in terms of a two-barrier model (a Schottky barrier at the Al–porous-silicon contact and a heterojunction at the porous-silicon–p-Si interface) connected in opposition. This model cannot be applied to our structure because it is unclear whether a rectifying contact is established at the Pd–porous-silicon interface. If we assume that in our structures the porous silicon is p-type, then under the conditions of a simple model which neglects the influence of the electronic states at the interface, the Pd–porous-silicon contact is Ohmic whereas the Al–porous-silicon contact is rectifying. For this reason we assume that the current-voltage characteristics of our structures will be determined by the isotypic p–p heterojunction between the crystalline p-Si and the wider-gap porous silicon.[5] The properties of this heterojunction have been little studied, but it is known[6] that the energy band diagrams and current-voltage characteristics of isotypic heterojunctions vary substantially depending on the doping level of the initial semiconductors and the presence of charge states at the interface. It was shown in Ref. 6 that Ge–Si n–n heterojunctions with donor concentrations of 10^{14} cm^{-3} and 5×10^{15} cm^{-3} in Si and Ge, respectively, exhibit current-voltage characteristics similar to the experimental data for our structures. Following Ref. 7, the current through an isotypic heterojunction is due to thermionic emission of carriers in opposite directions and is determined by the following expression:

$$J=J_0(1-V_B)[\exp(qU/kT)-1], \tag{1}$$

where V_B is the barrier potential of the heterojunction and J_0 is given by

$$J_0=qA^*TV_B\exp(-qV_B/kT)/k. \tag{2}$$

In this case, the reverse heterojunction current does not saturate but increases linearly for large U ($qU\gg kT$). The dependence of the forward current on qU/kT can be approximated by an exponential function, i.e., $J\propto\exp(qU/nkT)$.

An analysis of the current-voltage characteristics of our structures using the isotypic p–p heterojunction model shows that the dependence of the reverse current on the bias is accurately described by expression (1) for $V_B=0.7$–1 V for various samples. The forward branch of the experimental current-voltage characteristics at low bias with allowance for the base resistance of the porous silicon layer (600–1000 Ω) is extrapolated by the exponential function $J\propto\exp(qU/nkT)$. An analysis of the logarithmic dependence of the forward current on the bias allowed us to determine V_B and the ideality factor n for these structures. For the effective Richardson constant $A^*=8\times10^5$ A$\times$m$^{-2}\cdot$K^{-2} (Ref. 7), the barrier potential V_B varied in the range 0.6–0.8 V with the ideality factor $n=8$–14. The same values of the ideality factor for the current-voltage characteristics of Me–PS–p-Si structures were obtained in Refs. 2, 3, 8, and 9. The

1063-7850/97/060440-03$10.00

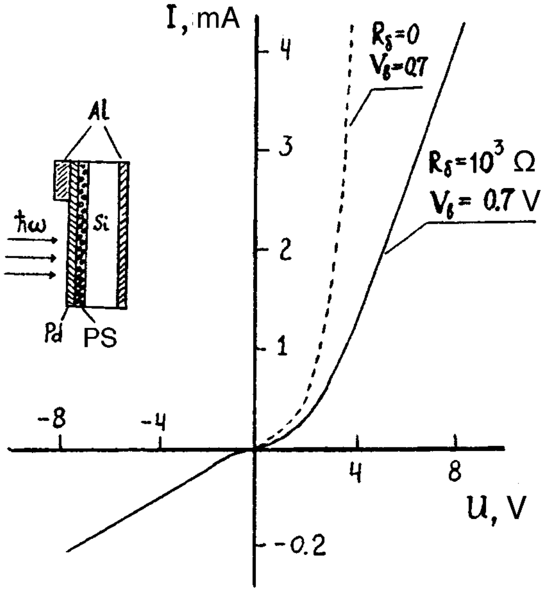

FIG. 1. Typical static current-voltage characteristic of Pd–PS–*p*-Si structures (a) and general view of these structures (b).

authors of these studies attribute this behavior to the high concentration of localized electronic states at the metal–porous-silicon interface. In our model for these structures we assume that the increase in the ideality factor *n* is strongly influenced by the high concentration of localized electronic states in the porous silicon and by its inhomogeneity.

The presence of localized electronic states in the porous silicon may influence the establishment of current through the structure. In order to determine this influence, we investigated the dynamic current-voltage characteristics of the structures under a periodic linearly varying bias. It was established that the form of the dynamic current-voltage characteristic depends on the rate of change of the bias across the structure. At repetition frequencies $<5\times10^{-3}$ Hz, clearly defined hysteresis was observed on the forward and reverse branches of the current-voltage characteristic for all the samples. Figure 2 shows a typical dynamic current-voltage characteristic for our structures, obtained at a bias repetition frequency of 10^{-3} Hz.

An analysis of the dynamic characteristics revealed that the establishment of the forward and reverse current through the structures is characterized by different times. Our investigations of the relaxation of the current through the structure under a pulsed bias allowed us to determine the characteristic times for this relaxation. We found that the times taken to establish the forward and reverse currents are 40 s and 13 s, respectively. This is consistent with the results of analyzing the hysteresis of the current-voltage characteristics. We therefore confirmed that the presence of deep electronic states is responsible for the hysteresis of the current-voltage characteristics.

Our model of a *p*–*p* heterojunction with deep electronic states in the porous silicon layer is confirmed by our investigations of the spectral photosensitivity of structures exposed to steady-state optical excitation without a bias. Figure 3 shows typical behavior of the photosensitivity for the structure whose current-voltage characteristic is illustrated in Figs. 1 and 2. A characteristic feature of all the structures studied are the heteropolar photoresponses in different parts of the spectrum. The maximum negative response was observed at almost the same wavelength for all the structures, but the shape and ratio of the positive and negative responses varied slightly from one sample to another. Similar photoeffects in Ge–Si *n*–*n* heterojunctions were observed in Ref. 6. As in that case, the negative photoresponse in our structures is attributed to photoexcitation in the single-crystal silicon while the long-wavelength positive response is determined by the photoexcitation from traps in the porous silicon and at its surface. The positive short-wavelength photoresponse is

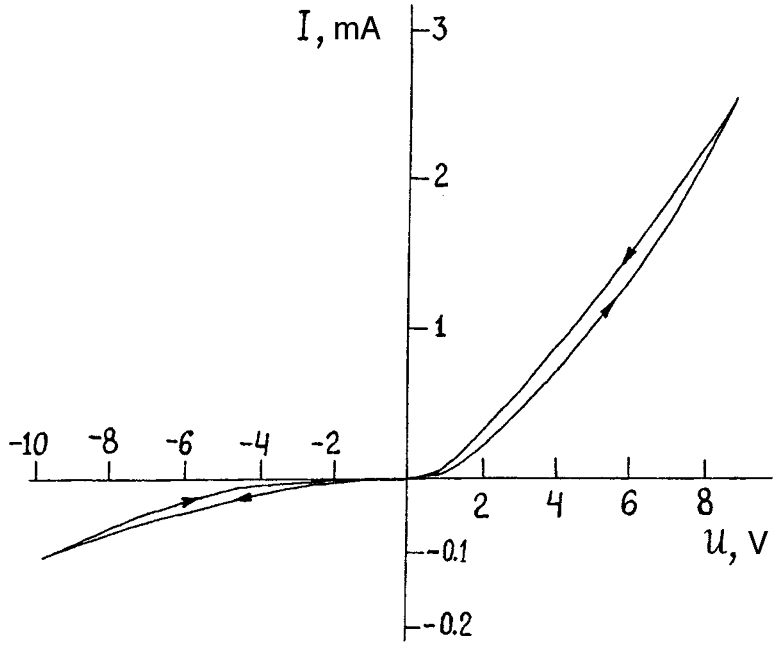

FIG. 2. Dynamic current-voltage characteristic of Pd–PS–*p*-Si structure.

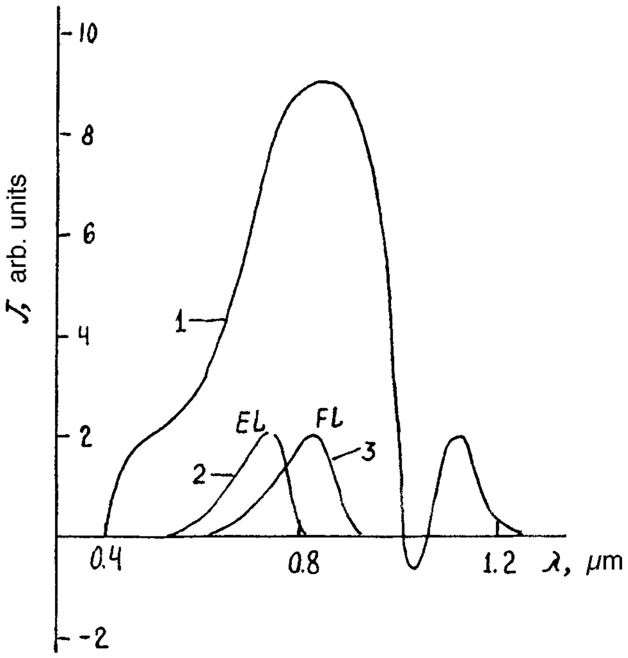

FIG. 3. Spectral dependences of the photoresponse (*1*), electroluminescence (*2*), and photoluminescence (*3*) of a Pd–PS–p-Si structure.

caused by the net photoelectric effect in the porous silicon and the crystalline silicon. The formation of traps in these structures was observed in studies of photoinduced charge trapping in porous silicon.[10] These traps may be associated with E'-centers in SiO_2 (Ref. 10) and also with boron electronic states in the presence of quantum-size effects in the porous silicon.

To conclude, our results indicate that the possible formation of an isotypic heterojunction and the presence of deep electronic states in the porous silicon, functioning as carrier traps, must be taken into account in analyses of current flow processes in Me–PS–p-Si structures. It has been shown that the experimental current-voltage characteristics of Pd–PS–p-Si structures are in good agreement with the theoretical curves obtained in the model of an isotypic p–p heterojunction between the single-crystal silicon and the porous silicon. The hysteresis observed in the dynamic current–voltage characteristics is caused by the presence of traps for holes in the porous silicon and this is confirmed by the photoresponse spectra of our structures. Further investigations are needed to identify the nature of these traps and these are planned for the future. Detailed results on photoeffects in porous-silicon structures will be presented in our next report.

The authors would like to thank S. P. Zimin for useful discussions and N. E. Mokrousov for supplying the samples.

[1] L. T. Canham, Appl. Phys. Lett. **57**, 1046 (1990).
[2] N. Koshida and H. Koyama, Appl. Phys. Lett. **60**, 347 (1992).
[3] M. Ben-Chorin, F. Möller, and F. Koch, J. Appl. Phys. **77**, 4482 (1995).
[4] S. P. Zimin, V. S. Kuznetsov, N. V. Perch, and A. V. Prokaznikov, Pis'ma Zh. Tekh. Fiz. **20**(22), 22 (1994) [Tech. Phys. Lett. **20**, 899 (1994)].
[5] L. V. Belyakov, D. N. Goryachev, O. M. Sreseli, and I. D. Yaroshetskiĭ, Fiz. Tekh. Poluprovodn. **27**, 1815 (1993) [Semiconductors **27**, 999 (1993)].
[6] A. G. Milnes and D. L. Feucht, *Heterojunctions and Metal–Semiconductor Junctions* (Academic Press, New York, 1972) [Russ. transl., Mir, Moscow, 1975].
[7] S. M. Sze, *Physics of Semiconductor Devices* (Wiley, New York, 1969) [Russ. transl., Énergiya, Moscow, 1963].
[8] H. P. Maruska, F. Namavar, and N. M. Kalkhoran, Appl. Phys. Lett. **61**, 1338 (1992).
[9] D. B. Dimitrov, Phys. Rev. B **51**, 1562 (1995).
[10] A. B. Matveeva, E. A. Konstantinova, V. Yu. Timoshenko, and P. K. Kashkarov, Fiz. Tekh. Poluprovodn. **29**, 2180 (1995) [Semiconductors **29**, 1146 (1995)].

Translated by R. M. Durham

Pinning of planar vortices in a three-dimensional Josephson medium and the applicability of the Bean model

M. A. Zelikman

St. Petersburg State Technical University

(Submitted December 11, 1996)
Pis'ma Zh. Tekh. Fiz. **23**, 66–69 (June 12, 1997)

Calculations are made of a system of planar vortices formed at the boundary of a sample with a monotonically increasing external magnetic field with allowance for pinning caused by the cellular nature of the medium. The spacing between the vortices remains approximately constant and does not decrease near the boundary. This behavior indicates that the magnetic field does not depend on the coordinate in the region where the vortices have penetrated. These observations contradict the conventional Bean model. © *1997 American Institute of Physics.* [S1063-7850(97)01206-8]

Vortices play an important role in magnetic field penetration processes in high-temperature superconductors. In the presence of pinning, these vortices form near the surface and penetrate into the sample with increasing field. The penetration of the field into the sample is usually calculated using the Bean model,[1] which assumes that all the vortices in the region where the field has penetrated, are in a ''critical state,'' i.e., that the force acting on each vortex from all the other vortices is equal to its maximum pinning force. To calculate the field profile, we need to know the dependence of this force on the magnetic field. Various mechanisms exist for the pinning of vortices at all possible types of crystal lattice defects acting as pinning centers. The authors of Refs. 2 and 3, for instance, considered the interaction between a continuous vortex and discretely distributed pinning centers for different ratios between the vortex dimensions and the spacing between the pinning centers.

In the present paper an analysis is made of a three-dimensional medium consisting of a cubic lattice in which each link of length h contains a single Josephson junction with a critical current J_c (Refs. 4 and 5). In this medium the vortex is not described by a continuous distribution of the phase difference but by discrete values thereof at various junctions. Pinning exists as a result of the cellular structure of the medium and is determined by the finite energy needed to displace the center of a vortex to the next cell. We calculate a system of vortices established in the sample with monotonically increasing external field and we check the validity of the Bean critical-state model.

Let us assume that a sample in the form of a thick plate is located in a magnetic field parallel to the plane of the plate. Then, the currents are distributed identically in all planes perpendicular to the external field. Although the formation of linear vortices is energetically more favorable, planar (laminar) vortices are considered subsequently (Fig. 1) because this model can be calculated, all subtleties can be eliminated, and the main results can be applied qualitatively to the case of linear vortices.

The conditions of fluxoid quantization in cells[4] were used to derive a system of equations to calculate the phase jumps φ_m at the Josephson junctions (Φ_0 is the magnetic flux quantum)

$$\varphi_m+1-2\varphi_m+\varphi_m-1=I\sin\varphi_m(\pm 2\pi),$$
$$(I=2\pi\mu_c hJ_c/\Phi_0), \tag{1}$$

where the terms $\pm 2\pi$ may appear on the right-hand side if the cell contains any vortex center.

Equations (1) constitute a recurrence relation to determine φ_{m+1} from known φ_m and φ_{m-1}, which allows us to calculate the distribution of φ_m over the entire sample using two values φ_1 and φ_2 at neighboring points. For a monotonically increasing magnetic field the vortex furthest from the boundary is at the surface of motion. To calculate this structure, we fix φ_1 and find φ_2 such that the neighbor to the right of some selected vortex is the greatest possible distance from it (ideally at infinity).

Then by varying φ_1 we minimize the distance from the nearest vortex on the left, and then from the next. By repeating this procedure many times, narrowing the range φ_1 time after time, we can find the unknown ''critical'' state of the vortex lattice. Calculations to fifteen decimal places can be used to find the position of 20–50 vortices. These calculations performed on a computer yielded the following results.

1. The distance between two stationary isolated vortices of the same orientation can vary between infinity and a cer-

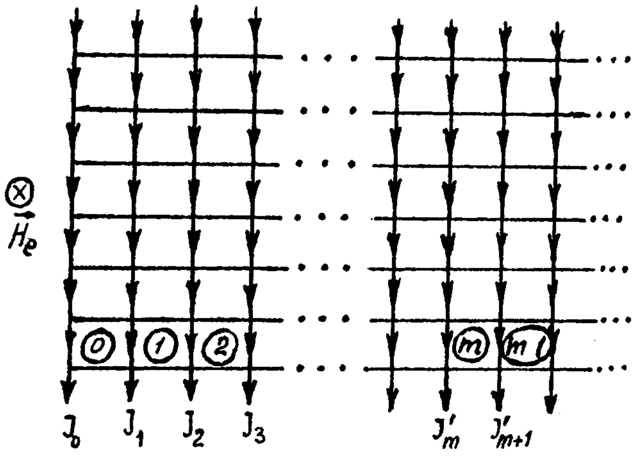

FIG. 1. Current distribution in a planar vortex in the plane perpendicular to the external field.

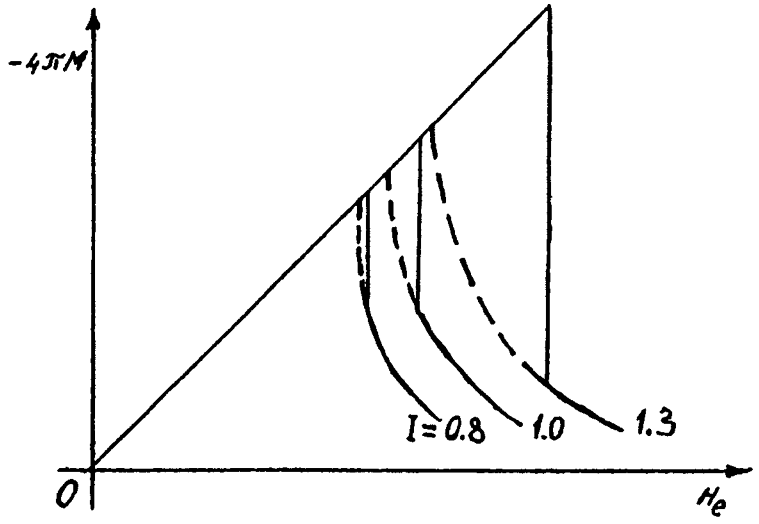

FIG. 2. Magnetization curves of sample for various I. The dashed curves correspond to no pinning.

tain minimum value. This behavior is caused by pinning, because in the absence of pinning the interaction between the vortices would separate them by infinity. As the parameter I increases, pinning is enhanced and the repulsion between the vortices decreases, so that the minimum distance between the vortices is reduced. For $I>2.9$ the centers of the vortices may be located in neighboring cells.

2. To find the magnetization curve of the sample, we analyze a system of vortices formed in a sample with a monotonically increasing external magnetic field. The shortest distance between the vortex furthest from the boundary and the nearest neighbor is a power function of I: $d \approx 6.1 \times 10^{-1.1}$.

3. For $I>1.4$, the distance between the vortices is reduced to one cell as the boundary is approached and then the centers of the vortices are located in neighboring cells. Beginning with $I=3.4$, the number of flux quanta Φ_0 in the vortex increases with increasing proximity to the sample boundary.

4. For $I \leqslant 1.3$, the distance between the vortices does not decrease as the boundary is approached, but remains approximately constant, which indicates that the magnetic field is independent of the coordinate. The theoretical magnetization curve of the sample is typical of type-II superconductors (Fig. 2). Pinning leads to an increase in the critical field H_c and a steep jump on the curve because the vortex lattice cannot have a period greater than that corresponding to the calculated critical state.

To conclude, it follows from these observations that under conditions of interacting vortices containing no more than one flux quantum Φ_0, the Bean model ceases to hold for pinning caused by the cellular nature of the medium.

[1] C. P. Bean, Rev. Mod. Phys. **36**, 31 (1964).

[2] Y. S. Kivshar, and B. A. Malomed, Rev. Mod. Phys. **61**, 763 (1989).

[3] V. V. Bryksin and S. N. Dorogovtsev, Zh. Éksp. Teor. Fiz. **102**, 1025 (1992) [Sov. Phys. JETP **75**, 588 (1992)].

[4] M. A. Zelikman, Sverkhprovodimost' (KIAE) **5**, 60 (1992) [Superconductors **5**, 60 1992)].

[5] M. A. Zelikman, Sverkhprovodimost' (KIAE) **5**, 1819 (1992) [Superconductors **5**, 1738 1992)].

Translated by R. M. Durham

Electroluminescence and current–voltage characteristics of *n*-type porous silicon structures

É. Yu. Buchin, N. A. Laptev, A. V. Prokaznikov, N. A. Rud', V. B. Svetovoĭ, and A. N. Chirkov

Yaroslavl' State University

(Submitted December 27, 1996)
Pis'ma Zh. Tekh. Fiz. **23**, 70–76 (June 12, 1997)

An investigation is made of a set of *n*-type porous-silicon structures exhibiting high electroluminescence efficiency and low degradation, and results are presented. These results demonstrate that operating voltages corresponding to those of standard ceramic–metal-oxide–semiconductor technology can realistically be achieved. © *1997 American Institute of Physics.* [S1063-7850(97)01306-2]

One of the unsolved problems impeding the expansion of the capabilities of conventional silicon technology is the development of light-emitting devices with an emission efficiency sufficient for practical applications. Porous silicon is a promising material for the development of such devices, since it can convert supplied energy into visible radiation at room temperature. Thus, numerous studies have been devoted to the physicochemical properties of this new material and to investigations of methods of preparing it.[1]

Studies of the properties of porous silicon attracted particular interest following the observation of efficient visible photoluminescence (of the order of 10%) at room temperature.[2] This discovery inspired hopes of developing light-emitting devices based on silicon technology. These devices could be integrated monolithically with other silicon structures to fabricate optical interconnections and planar displays. The most important property for practical applications is the electroluminescence of porous silicon, when light is emitted under the action of a flowing current. The first attempts to fabricate electroluminescent devices revealed a low electroluminescence efficiency (of the order of 10^{-5}%), which was inadequate for practical purposes.[3–5] This difficulty caused some loss of interest in this topic but the publication of the first promising results in 1995 rekindled interest.[6]

The electrophysical properties of *p*-type porous silicon structures not exhibiting electroluminescence were studied in Refs. 7–9. Carrier transport in porous silicon layers of varying thickness was investigated in Ref. 7, where it was shown that the problem of injection from the contact could be resolved by fabricating a sufficiently thin layer of porous silicon. It was shown in Ref. 8 that the rectifying properties of porous silicon structures can be attributed to depletion in the single-crystal silicon substrate in the porous silicon–single-crystal silicon transition zone. The frequency dependence of the conductivity and permittivity of porous silicon structures was investigated in Ref. 9. The experimentally observed behavior is explained in terms of hopping conduction on a fractal network.[9]

In the present paper, we investigate the electroluminescence and electrophysical properties of specially prepared porous silicon structures fabricated on KÉF-20 substrates. The special technology used to fabricate the electroluminescent structures involved two important aspects: controlled, reproducible formation of structures with a special porous-structure morphology and the final laser treatment of these porous silicon layers to produce electroluminescence.

The morphology of the porous structure[10–12] was controlled by selecting the operating point on the current–voltage characteristic of the silicon anodization process in hydrofluoric acid solutions. In particular, structures with a mixed type of porous silicon morphology were fabricated by shifting the current–voltage characteristic during the anodization process. The resultant structures have reliably reproducible morphologies and the electroluminescence properties differ for each type of morphology. The aim was to fabricate those structures with the highest electroluminescence efficiency. Note that there is no correlation between the photoluminescence, whose level is always fairly high for our samples, and the electroluminescence properties of structures based on these samples. The emitting properties of the prepared samples are influenced not only by the techniques used to fabricate the porous silicon but also by the subsequent treatment methods used to produce the emitting structures. Our particular aim was to optimize the conditions for removal of the insulating film from the surface of the porous silicon and metal (to enable transmission of output radiation) by laser treatment of the surface. Fired Al was used as the lower Ohmic contact with the Si in the metal–porous-silicon–silicon–metal structure while the upper Ohmic contact with the porous silicon was formed by Pt, Au, or Al. The upper contact was prepared as follows. The natural insulating film formed on the porous silicon layer during anodization was used as an interlayer insulator. At those points where contact was required between the metal and the porous silicon, the film was removed by N_2 laser pulses with a controlled number of pulses incident at each point. Two types of structure were formed on each sample. ''Point'' structures consist of equidistant holes (100 μm spacing), approximately 20 μm in diameter, made in the film. ''Comb'' structures are formed by lines 20 μm wide and 100 μm apart removed from the insulating film. An approximately 0.2 μm layer of metal was then deposited on the surface. On the point structures the metal was removed by laser etching everywhere except for the narrow lines connecting the points. On the comb structures an interdigital structure of narrow metal

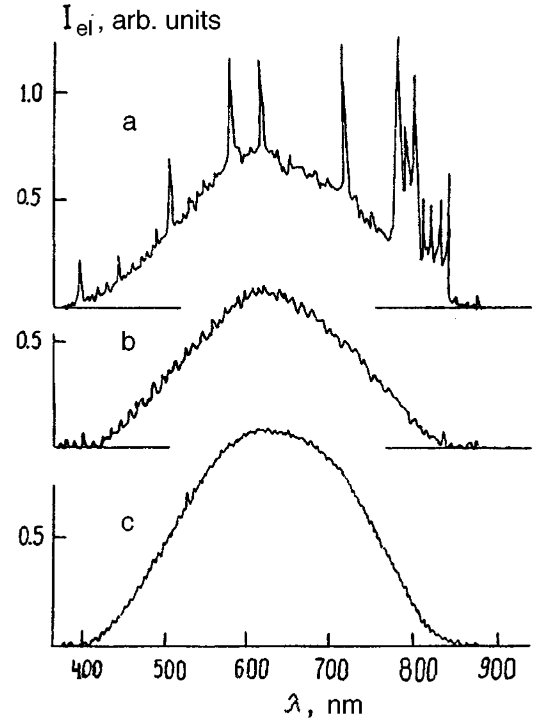

FIG. 1. Electroluminescence spectra obtained for the following structures: a — sample B_2, comb structure; b — sample B_2, point structure; c — sample B_3, point structure.

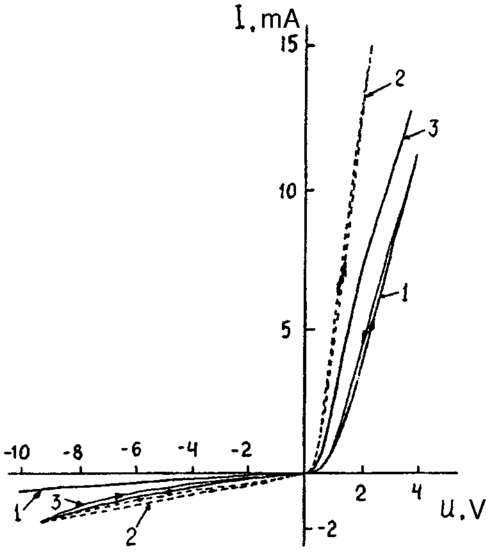

FIG. 2. Current–voltage characteristics obtained for the following structures: *1* — sample B_2, comb structure; *2* — sample B_2, point structure; *3* — sample B_3, point structure.

strips was formed similarly. In the latter case, the current flow geometry can be varied, perpendicular or parallel to the surface of the sample, respectively. The different samples were identified as A_N, etc., where the letters $A, B, C, \ldots$ correspond to a specific morphology of the porous structure and the subscript N indicates the laser treatment conditions used to form the light-emitting structure. Around twenty different structures were singled out for investigation.

Figure 1 shows the electroluminescence spectra of structures using samples B_2 and B_3 in which the upper contact is made of Pt. The point structures begin to emit at the potential $V \approx 20$ V and current $I \approx 20$ mA and give a bluish white luminescence, clearly visible in the dark. The luminescence is only observed under reverse bias, i.e., when a negative potential is applied to the upper electrode. The B_2 comb structures begin to emit at $V \approx 60$ V and $I \approx 30$ mA. Bright bursts of red luminescence are clearly visible and begin to dominate as the potential increases. We note that the red luminescence is far brighter and clearly visible in daylight. The bluish white luminescence is evidently attributable to surface levels at the upper interface of the porous silicon. The red luminescence is most likely caused by quantum-size effects in the porous silicon. Thus, two types of luminescence were observed: stable but weak bluish white luminescence and unstable but efficient red luminescence.

Figure 2 shows the current–voltage characteristics of B_2 and B_3 point structures and a B_2 comb structure. It can be seen that the characteristic exhibits rectifying behavior. Hysteresis can be clearly identified and changes its form depending on whether electroluminescence has occurred in the sample. For example, whereas broader hysteresis was observed on the reverse branch prior to electroluminescence, after the electroluminescence the hysteresis was broader on the forward branch, and conversely. If we follow the current–voltage characteristic in the directions indicated by the arrows, on the lower forward branch of the characteristic carriers are dumped into the conducting state from surface states or deep levels, so that on the return section of the forward branch these excess carriers make an additional contribution to the total current and the return section of the forward branch is higher. On the reverse branch, the pattern is reversed (apart from the sign).

This complex characteristic indicates that several junctions are operating efficiently in the Pt–porous-silicon–Si–Al system. This conclusion is supported by an investigation of the behavior of the photovoltage in the barrier-layer regime, which changes its sign at a specific illumination wavelength.[13] These data will be published in detail at a later date.

These current–voltage characteristics obtained have different profiles, particularly for samples whose porous layers are prepared by different methods and for which the subsequent laser treatments used to produce the electroluminescence also differ. Differences are also observed in the type of hysteresis. This is because the resulting structure is a fairly complex system of junctions between materials with different physical properties, characterized by a different band structure. The experimentally observed behavior suggests that the Pt–porous-silicon–Si–Al system may be represented schematically as a system of series-connected devices possessing rectifying properties. The behavior of the Pt–porous-silicon junction is obviously similar to the diode properties of a metal–semiconductor junction and has a negligible influence on the current–voltage characteristic. The properties of the porous-silicon–Si junction are similar to those of an isotypic n–n heterojunction with different band gaps on the left and right of the junction. The behavior of this junction may be made more complex by the presence of surface states at the junction. The operation of an isotypic heterojunction may be modeled, according to Ref. 13, by two diodes connected in opposition. The Fermi level in the porous silicon and the impurity levels in the porous silicon are lower in relation to the conduction band than those in ordinary silicon as a result of the quantum-size effect.[14] It was shown in Ref. 13 that the operation of an isotypic $n-n$ heterojunction (from the point of view of the current–voltage characteristic) depends in particular on the position of the Fermi level in the wider-gap semiconductor, in this case the porous silicon. The position of this level in the porous silicon is determined by the preparation technology, since it is associated with the quantum-size effect (via the transverse pore sizes).

In conclusion we note that this set of structures has demonstrated a fairly high electroluminescence quantum efficiency and the samples have shown no appreciable degradation over prolonged operation (several months). These experiments have demonstrated that it is a realistic proposition to attain operating voltages corresponding to those of standard ceramic–metal-oxide–semiconductor technology.

The authors would like to thank V. F. Bochkarev and V. V. Naumov for assistance with preparing the structures.

[1] R. L. Smith and S. D. Collins, J. Appl. Phys. **71**, R1 (1992).
[2] L. T. Canham, Appl. Phys. Lett. **57**, 1046 (1990).
[3] N. Koshida and H. Koyama, Appl. Phys. Lett. **60**, 347 (1992).
[4] A. Richter, P. Steiner, F. Kozlowski, and W. Land, IEEE Electron. Dev. Lett. **EDL-12**, 691 (1991).
[5] F. Namavar, H. P. Maruska, and N. M. Kalkhoran, Appl. Phys. Lett. **60**, 2514 (1992).
[6] A. Loni, A. J. Simons, T. I. Cox, P. D. J. Calcott, and L. T. Canham, Electron. Lett. **31**, 1288 (1995).
[7] M. Ben-Chorin, F. Möller, and F. Koch, Phys. Rev. B **49**, 2981 (1994).
[8] M. Ben-Chorin, F. Möller, and F. Koch, J. Appl. Phys. **77**, 4482 (1995).
[9] M. Ben-Chorin, F. Möller, F. Koch, W. Schirmacher, and M. Eberhard, Phys. Rev. B **51**, 2199 (1995).
[10] É. Yu. Buchin, A. V. Postnikov, V. A. Prokaznikov, V. B. Svetovoĭ, and A. B. Churilov, Pis'ma Zh. Tekh. Fiz. **21**(1), 60 (1995) [Tech. Phys. Lett. **21**, 27 (1995)].
[11] E. Yu. Buchin, A. B. Churilov, A. V. Postnikov, A. V. Prokaznikov, and V. B. Svetovoy, Phys. Low-Dim. Struct. **2/3**, 97 (1995).
[12] E. Yu. Buchin, A. B. Churilov, and A. V. Prokaznikov, Appl. Surf. Sci. **102**, 431 (1996).
[13] A. G. Milnes and D. L. Feucht, *Heterojunctions and Metal-Semiconductor Junctions* (Academic Press, New York, 1972) [Russ. transl., Mir, Moscow, 1975].
[14] C. Cadet, D. Deresmes, D. Vuillaume, and D. Stievanard, Appl. Phys. Lett. **64**, 2827 (1994).

Translated by R. M. Durham

Electronic properties of microporous silicon under illumination and with the adsorption of ammonia

Yu. A. Vashpanov

I. I. Mechnikov State University, Odessa

(Submitted January 27, 1997)
Pis'ma Zh. Tekh. Fiz. **23**, 77–82 (June 12, 1997)

An electromotive force has been observed at contacts of porous silicon samples, its magnitude and sign varying with illumination and adsorption of ammonia. The samples exhibit characteristic nonuniformity of the porosity along the surface of the material. The physical mechanism for these effects is discussed. © *1997 American Institute of Physics.* [S1063-7850(97)01406-7]

Porous silicon is currently a promising material in semiconductor electronics whose physical properties are attracting attention among many researchers.[1–4] Particular interest is focused on studying the luminescence properties,[5,6] because of the possibility of developing silicon light emitters. Porous silicon has a large surface area, which leads to high chemical activity when this material interacts with an ambient gas.[7,8] Despite a considerable number of studies, the physical properties of porous silicon have not yet been determined definitively. This particularly applies to the mechanism of carrier localization and the adsorption sensitivity of the material. The electronic parameters of porous silicon may vary widely, depending on its preparation conditions. The search for a techniques to fabricate photosensitive and gas-sensitive porous-silicon sensors is also relevant.

Porous silicon samples were prepared by electrochemical etching of *n*- and *p*-type single-crystal silicon in a 48% aqueous solution of hydrofluoric acid. During the etching process the material was subjected to additional illumination and ultrasound treatment. Aluminum electrical contacts were deposited on the surface of the material.

The electronic properties of the samples were studied at temperatures between 293 and 573 K in a special measuring chamber in which the semiconductor could be illuminated, the composition of the gaseous atmosphere could be altered or the system evacuated. The influence of the adsorption of O_2, H_2, NO, NO_2, CO_2, CH_4, and NH_3 gas on the electronic parameters of the material was studied. Certified cylinders of these gases and highly pure nitrogen were used.

When studying the electronic properties of these porous silicon samples, we observed that a voltage U appeared at the contacts of some of the samples. These samples had a porosity higher than 12%. The value of U was considerably higher in samples possessing higher porosity and reached 35 mV in some cases. The magnitude and sign of U also depended on the geometry of the contacts and their distribution over the surface of the material.

The greatest effect was observed for a porous silicon sample with an average porosity of 45%. After the samples had been heated at temperatures above 423 K in high vacuum, the value of U at room temperature was 3 mV. When the semiconductor was illuminated with white light ($E=130$ lx), U was observed to increase to $+27$ mV (Fig. 1, curve *1*). The spectra of these gases showed that only the adsorption of ammonia vapor led to any change in the electronic parameters of the material and the value of U. As a result of contact with 490 ppm of ammonia in highly pure nitrogen, U initially decreased and then changed its sign (Fig. 1, curve *2*). Under steady-state conditions the value of U reached -35 mV. When the sample was subsequently illuminated, U increased to $+5$ mV(Fig. 1, curve *3*).

Figure 2 shows current-voltage characteristics measured in the dark (curve *1*), under illumination by white light at 130 lx (curve *2*), and after adsorption of 490 ppm of ammonia vapor (curve *3*). It can be deduced from these results that the material contains an internal electric field whose magnitude and sign depend on the measurement conditions (illumination or adsorption of ammonia).

It should be noted that unlike the other gases studied, the ammonia molecule has a high intrinsic dipole moment.[9] The adsorption of oxidizing gases (O_2, NO_2, CO_2) has no influence because of the fluorine atom content at the surface of the material while the adsorption of H_2 and CH_4 has no effect because of the high hydrogen content incorporated into the surface region during the anodic etching process.[10] In addition, at room temperature these gases undergo very little chemisorption because of the high heats of adsorption. This means that the physical reason for the change in the electronic parameters of the material is the physical adsorption of dipolar ammonia molecules.

A decrease in the absolute value of U with increasing measurement temperature is observed after the preliminary adsorption of ammonia. At 423 K in high vacuum, U again reaches $+3$ mV and cooling to room temperature in vacuum does not alter this voltage. With subsequent admission of ammonia vapor and illumination of the material the U profile is repeated (Fig. 1). This behavior indicates that these porous silicon samples contain an internal electric field whose magnitude and polarity depend on the adsorption of polar ammonia molecules and on the illumination.

A study of the surface morphology of samples with a microporous structure by scanning electron microscopy revealed that the body of the silicon is permeated with cylindrical pores. In addition, the surface of the porous silicon samples showing the greatest effect displayed nonuniform regions of enhanced and reduced porosity, pore diameter, and relative distribution, i.e., the geometric structure of these porous silicon samples is nonuniform.

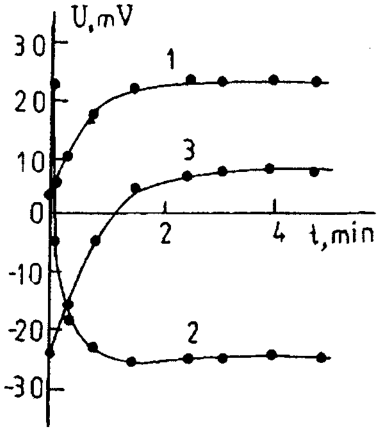

FIG. 1. Time dependences of U for illumination of porous silicon (curve *1*), in contact with 490 ppm ammonia vapor in highly pure nitrogen (*2*), and subsequent illumination (curve *3*).

A study of the chemical composition using secondary-ion mass spectroscopy revealed that the material contains a significant number of incorporated hydrogen atoms. The concentration of hydrogen atoms is highest near the surface, 20–46 at.%, and decreases to zero in the interpore space. Fluorine atoms were also observed at the surface at a concentration of 2–4 at.%.

It is interesting to note that in hydrogenated silicon the band gap depends on the incorporated hydrogen concentration.[11] Thus, the electronic structure of porous silicon may be represented as a variable-gap material with a maximum band width at the surface and a minimum in the interpore space. The nonuniform geometric and electronic properties of the material give rise to a spatially dependent band width and large fluctuations in the potential in the porous silicon structure. This leads to spatial localization of the carriers at potential energy minima, and regions of positive and negative charge are formed. For porous silicon samples with a porosity of 45% and an average pore diameter of less than 10 nm, the spacing between the pores is less than 100 nm. For a localization of the positive and negative charge of the order of $10^{17}q$ (q is the electron charge) with a spacing between them of 10 nm, a dipole is formed with a moment approximately equal to one debye.

In strictly periodic porous silicon structures the voltage at the contacts should be zero since the local fields of the regions are opposed. On account of the asymmetry in the properties of the porous structure in various directions along the surface the value of U will be nonzero. Thus, the value of U, equal to the sum of the electric fields of the local spatial structures in the material, is nonzero in certain directions.

When the surface of the semiconductor is illuminated, the nonequilibrium carriers tend to become localized at sites of minimum potential energy. This will be accompanied by an increase in the charge density localized in these spatial regions, which will increase the internal field and the voltage U.

Conversely, the adsorption of polar ammonia molecules reduces the internal local field and thus the voltage U on the contacts because the local field of the ammonia dipoles is in the direction opposite to that of the structure field of the material. The adsorption of NH_3 is intensified by fluorination of the surface of porous silicon.[10] In this case, the adsorbed ammonia dipoles become aligned perpendicular to the surface of the pores. The dipole moment of ammonia molecules is 1.46 D which is comparable with that in the porous silicon structures exhibiting the maximum effect. The local electric fields of the adsorbate may lead to relocalization of the charge in the structure and a change in the sign of U, as was observed experimentally.

It is important to note that a voltage was observed in samples having a porosity greater than 12%. This factor suggests that for lower porosities the internal fields are fairly weak and the voltage U is not recorded experimentally. As the porosity increases to 45%, the adsorption of polar gas has the greatest influence on U in asymmetric porous silicon structures.

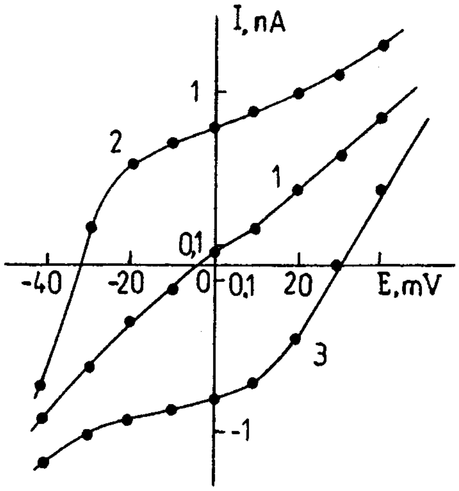

FIG. 2. Current–voltage characteristics of porous silicon samples measured in darkness after heating in vacuum at 423 K (curve *1*), illumination with white light (curve *2*), and after adsorption of 490 ppm ammonia vapor (curve *3*).

[1] R. Sabet-Dariani and D. Haneman, J. Appl. Phys. **76**, 1346 (1994).
[2] A. G. Cullis, L. T. Canham, G. M. Williams *et al.*, J. Appl. Phys. **75**, 493 (1994).
[3] V. P. Bondarenko, V. E. Borisenko, A. M. Dorofeev *et al.*, J. Appl. Phys. **75**, 2727 (1994).
[4] T. Ozari, M. Araki, S. Yoshimura *et al.*, J. Appl. Phys. **76**, 1986 (1994).
[5] E. V. Astrova and A. A. Lebedev, Fiz. Tekh. Poluprovodn. **29**, 1649 (1995) [Semiconductors **29**, 858 (1995)].
[6] A. J. Kontkiewicz, A. M. Kontkiewicz, J. Siejka *et al.*, Appl. Phys. Lett. **65**, 1436 (1994).
[7] V. A. Labunov, V. P. Bondarenko, and V. G. Borisenko, Zarub. Elektron. Tekh. 3 (1978).
[8] M. Ben-Chorin, A. Kux, and I. Schechter, Appl. Phys. Lett. **64**, 481 (1994).
[9] V. F. Kiselev and O. V. Krylov, *Electronic Effects in Adsorption and Catalysis at Semiconductors and Insulators* [in Russian], (Nauka, Moscow, 1979).
[10] Yu. A. Vashpanov, Fotoelektronika, No. 6, 68 (1995).
[11] B. Delley and E. F. Steigmeier, Appl. Phys. Lett. **67**, 2370 (1995).

Translated by R. M. Durham

Polycrystalline silicon films doped with aluminum during deposition

D. V. Shengurov

Scientific-Research Physicotechnical Institute, Nizhniĭ Novgorod State University

(Submitted January 10, 1997)
Pis'ma Zh. Tekh. Fiz. **23**, 83–87 (June 12, 1997)

Aluminum-doped polycrystalline silicon films have been grown by molecular-beam deposition at substrate temperatures between 540 and 600 °C. The grain size increases to 1–8 μm with increasing substrate temperature. High Hall mobilities of the carriers were measured, in the range 30–90 cm^2/V·s. © *1997 American Institute of Physics.* [S1063-7850(97)01506-1]

Polycrystalline silicon films are widely used to fabricate thin-film transistors,[1] solar cells,[2] sensors,[3] and various other components of integrated circuits.[4] A disadvantage of this material is that it contains grain boundaries, which are responsible for degradation of its electrical and optical properties. Increasing the grain size and hydrogen passivation of grain boundaries reduces the density of traps at grain boundaries and thereby improves the quality of the devices.[5,6]

Among the various methods of obtaining polycrystalline silicon with a large grain size at low temperature ($\leqslant$600 °C), mention should be made of the method of depositing amorphous films, followed by crystallization by prolonged (several tens of hours) annealing at ~500 °C (Ref. 7). However, this process is uneconomical.

It is known that the crystallinity of films deposited on steel[8] or fused quartz[9] substrates is improved considerably when silicon is deposited onto an aluminum sublayer at or near the eutectic temperature of Al–Si.

In the present paper an investigation is made of how the coevaporation of aluminum during the molecular beam deposition of silicon influences the fabrication of polycrystalline silicon of large grain size and high carrier mobility.

Polysilicon films were prepared by molecular-beam deposition using a subliming silicon source doped with aluminum by a procedure described in Ref. 10. The aluminum concentration in the source was $\sim 9\times10^{18}$ cm^{-3}. The substrates were silicon wafers coated with a ~0.4 μm thick layer of thermally grown oxide. The films were prepared under two sets of conditions. In the first, the films were deposited at a selected temperature between 540 and 600 °C. In the second, they were deposited at a substrate temperature of ~300 °C and then annealed at a temperature in this range immediately after deposition without exposing the films to air.

The influence of the deposition and annealing temperature on the surface morphology of the films was investigated using electron photomicrographs obtained from carbon-platinum replicas. As the deposition temperature of the film increases from 540 to 580 °C, the grain size becomes larger (see Figs. 1a, 1b, and 1c). The films grown at 540° still exhibit a fine-grained structure, while those grown at T_s=560 °C show fine grains combining to form larger islands. As the growth temperature is increased further (to 580 °C), the grains in these islands merge to form larger grains whose dimensions may reach several (1–5) micrometers.

For films deposited at reduced temperature (300 °C) and then annealed, the dependence of the grain size on the annealing temperature was similar to the previous case. However, in these films the grains had a flat top (see Figs. 1d, 1e, and 1f) and the grain sizes were ~0.8 μm.

Table I gives the deposition (T_s) and annealing (T_{ann}) temperatures, as well as the resistivity (ρ), concentration (N), and mobility (μ) of the carriers in the films. It can be seen that as the substrate temperature increases, the resistivity decreases and the carrier concentration increases, reaching a maximum of 3.6×10^{18} cm^{-3} at T_s=580 °C. The maximum carrier mobility in this film was ~90 cm^2/V·s. When the temperature was increased further, the resistivity increased. A nonmonotonic dependence of ρ on T_{ann} was also observed for films grown in the two-stage regime. At an annealing temperature of 580 °C, the carrier concentration in the film was almost the same as that in the source and the maximum carrier mobility was 29 cm^2/V·s.

The higher carrier concentration in the films grown under the second set of conditions, compared with that in films grown under the first, may well be attributed to a difference in the mechanism of dopant (aluminum) capture by the growing silicon layer. When the polycrystalline film is grown at elevated temperature (540–600 °C), as in the growth of an epitaxial layer, the aluminum segregates at the surface.[11] It only begins to penetrate into the crystal after a certain amount has accumulated on the growth surface.[12] When the film is deposited at reduced (~300 °C) temperature, the dopant penetrates into the amorphous film with a capture coefficient of unity. As a result of subsequent annealing, the film recrystallizes and the embedded impurity becomes electrically active. Increasing the annealing temperature above 580 °C probably intensifies the diffusion of aluminum toward grain boundaries. As a result, its concentration in the grain decreases and the resistivity increases. Another possible reason for the improved electrical properties of polycrystalline silicon films doped with aluminum during deposition is the passivation of the grain boundaries caused by the appreciable diffusion of aluminum toward these boundaries.[13]

To conclude, the coevaporation of aluminum during the molecular-beam deposition of silicon can be used to grow

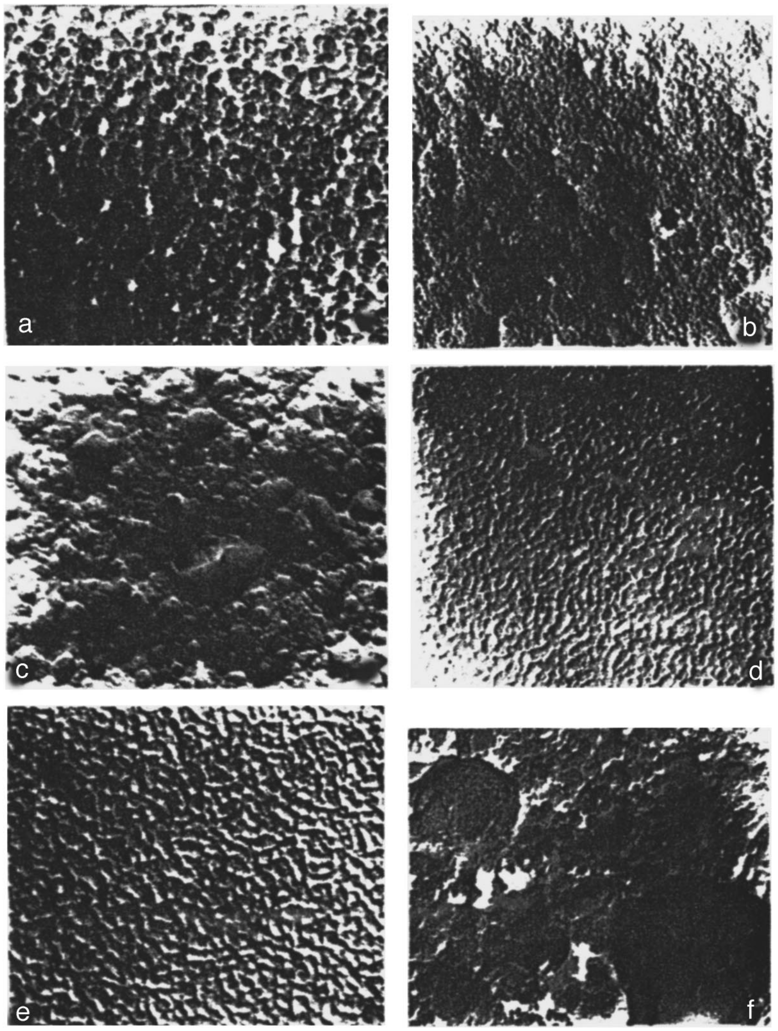

FIG. 1. Photomicrographs of carbon replicas of the surface of silicon films grown at: a — 540 °C, b — 560 °C, c — 580 °C, d–f — 300 °C and annealed at: d — 540 °C, e — 560 °C, and f — 580 °C (×16 000).

polycrystalline silicon at relatively low temperature (~580 °C) with grain sizes of several micrometers, a carrier concentration close to that in the source, and a carrier mobility of ~30–90 $\mathrm{cm^2/V \cdot s}$.

TABLE I. Resistivity (ρ), carrier concentration (N), and mobility (μ) in aluminum-doped polycrystalline silicon films for different preparation conditions.

T_s, °C	T_{ann}, °C	ρ, $\Omega \cdot$cm	N, $\mathrm{cm^{-3}}$	μ, $\mathrm{cm^2/V \cdot s}$
540	–	1.5×10^{2}	1.7×10^{15}	3.8
560	–	1.2	1.1×10^{18}	14.4
580	–	1.9×10^{-2}	3.6×10^{18}	89
600	–	4.6	5.2×10^{17}	5.9
300	540	7.8×10^{1}	3×10^{16}	2.5
300	560	2.7×10^{1}	1×10^{17}	4.2
300	580	2.4×10^{-2}	8×10^{18}	29
300	600	5×10^{2}	1.7×10^{16}	7.3

[1] M. K. Hatalis and D. W. Greve, IEEE Electron. Dev. Lett. **EDL-8**, 361 (1987).
[2] Z. Shi and S. R. Wenham, Progr. Photovolt. **2**, 153 (1994).
[3] P. H. L. Rasky, D. W. Greve, M. N. Kryder, and S. Dutta, J. Appl. Phys. **57**, 4077 (1985).
[4] S. D. Malhi *et al.*, IEEE Trans. Electron. Dev. **ED-32**, 258 (1985).
[5] H. Seager and D. S. Grinley, Appl. Phys. Lett. **34**, 337 (1979).
[6] A. Mimura, N. Konishi, K. Ono *et al.*, IEEE Trans. Electron. Dev. **ED-36**, 351 (1989).
[7] N. Yamauchi and R. Reif, J. Appl. Phys. **75**, 3235 (1994).
[8] P. H. Fang, I. Ephrath, and W. B. Nowak, Appl. Phys. Lett. **25**, 583 (1974).
[9] C. A. Chang, W. J. Siekhaus, T. Kaminska, and D. T. Hou, Appl. Phys. Lett. **26**, 178 (1975).
[10] D. A. Pavlov, V. G. Shengurov, D. V. Shengurov, and A. F. Khokhlov, Fiz. Tekh. Poluprovodn. **29**, 286 (1995) [Semiconductors **29**, 142 (1995)].
[11] G. E. Becker and J. C. Bean, J. Appl. Phys. **48**, 3395 (1977).
[12] V. P. Kuznetsov, R. A. Rubtsova, T. M. Isaeva *et al.*, Elektron. Tekh. Ser. Mater. **11**, 24 (1983).
[13] R. Sundaresan, D. E. Burk, and J. G. Fossum, J. Appl. Phys. **55**, 1162 (1984).

Translated by R. M. Durham

Method of monitoring the shape of an atomic force (tunneling) microscope tip using backscattering spectrometry

G. V. Dedkov and S. Sh. Rekhviashvili

Kabardino Balkarsk State University, Nal'chik

(Submitted September 24, 1996)
Pis'ma Zh. Tekh. Fiz. **23**, 88–92 (June 12, 1997)

A method is proposed to monitor the shape of an atomic force microscope tip, which can combine the operations of ion etching and shape monitoring, by using the intensity of the backscattering of ions from the same or a different beam to monitor the shape. Relationships have been obtained to monitor the shape of the probe using the measured dependence of the backscattering intensity on the parameters of the incident beam. © *1997 American Institute of Physics.* [S1063-7850(97)01606-6]

The scanning tunneling microscope (STM) and atomic force microscope (AFM) are among the most efficient analysis tools in surface physics, nanotechnology, and other fields.[1,2] Despite the continuing search for new modifications, the systems for scanning and processing an electrical signal in these devices have already attained a high level of perfection. The least controllable operation in the construction of STMs and ATMs and the least amenable to straightforward production techniques is the preparation of the sensing element — the tip. It is particularly important to fabricate tips of controllable shape with a small radius (around a few angstroms, or ideally, with a single atom at the apex of the tip). Real measurements of the radius of curvature of the probe tip and its overall shape have so far presented difficulties. Ion beam milling[3,4] whereby the tip surface of is etched with an ion beam has recently been used as a promising method of sharpening the tip. In the present paper we propose a method of combining the operations of ion milling and monitoring the probe shape by using the intensity of the backscattering of ions from the same or a different beam to monitor the shape. A very important factor is that both processes can be performed in a single vacuum chamber.

We assume that the STM (AFM) tip has a parabolic profile with radius of curvature R at the lower section and height H. A highly collimated ion beam of circular cross section with initial energy E_0 is directed onto the tip, as shown in Fig. 1. If the projection of the tip onto the plane perpendicular to the beam has the area F, the backscattering yield on reflection of the beam from its surface will be

$$Y = IFN\sigma \frac{\delta E}{S(E_0)} \delta\Omega, \tag{1}$$

where the standard notation is used: I is the flux density of the incident ions, σ is the differential scattering cross section, N is the density of the tip atoms, δE and $\delta\Omega$ are the energy and angular resolution of the detector, and $S(E)_0$ is the initial stopping power. The use of formula (1) presup-

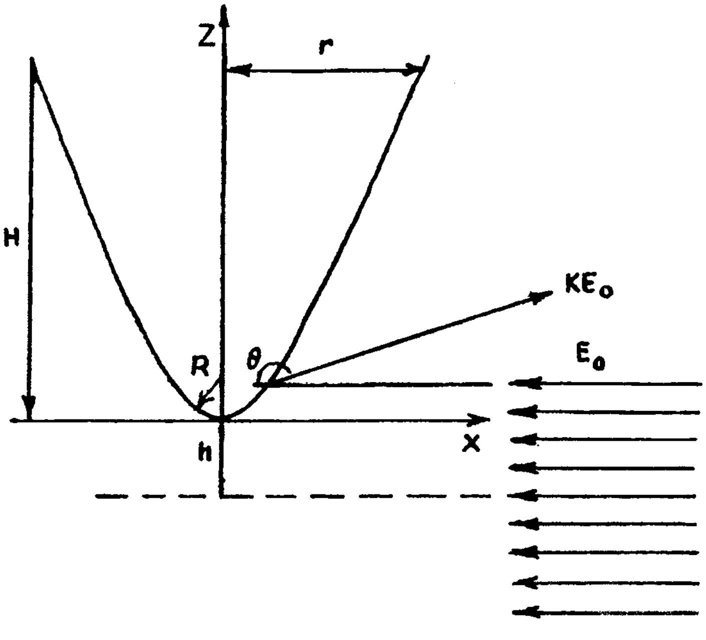

FIG. 1. Design of experiment.

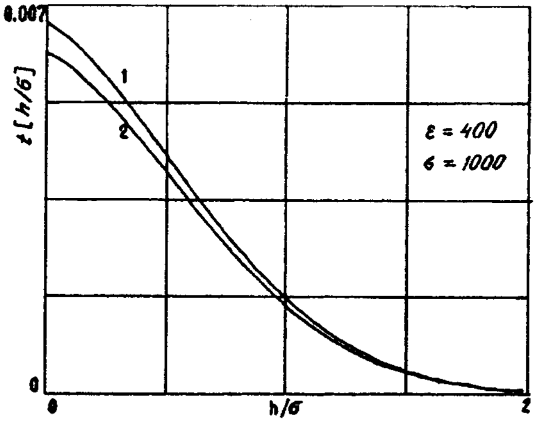

FIG. 2. Relative intensity of backscattering from AFM tip for various distances h of beam axis from the end of the tip. It is assumed that $H/R=\varepsilon=400$ and $\sigma/R=1000$. Curve *1* is plotted for a parabolic tip and curve *2* for a conical tip.

poses that only those ions backscattered near the surface of the tip with a layer thickness determined by $\delta E/S(E_0)$ are recorded.

This factor is important because recording the backscattering yield in a wider energy range impairs the proportionality between Y and the surface area at the convex tip.

Assuming that the beam axis is located at a distance h from the end of the tip (Fig. 1) and that it has a Gaussian intensity distribution over the cross section (with standard deviation σ), the product IF should be determined by averaging over the area of the projection of the tip on the xz plane:

$$\langle IF\rangle=\frac{I_0}{\pi\sigma^2}\int\int_S dxdz\,\exp\left[-\frac{(z+h)^2+x^2}{\sigma^2}\right], \tag{2}$$

where I_0 is the maximum beam intensity (at its center). Subsequently, all the linear dimensions and coordinates are conveniently expressed in units of R. Formula (2) is simplified by substituting the variables $u=x/\sigma$ and $v=z/\sigma$, $\varepsilon=H/R$. For a tip with the surface equation $z=(x^2+y^2)/2R$, we obtain:

$$\langle IF\rangle=I_0R^2f(\varepsilon,\sigma,n), \tag{3}$$

$$f(\varepsilon,\sigma,h)=0.5\,\mathrm{erf}\left[\frac{\sqrt{2\varepsilon}}{\sigma}\right]\left\{\mathrm{erf}(\varepsilon/\sigma+h/\sigma)-\mathrm{erf}(h/\sigma)-\frac{1}{\sqrt{\pi}}\exp(-h^2/\sigma^2)\int_0^{\varepsilon/\sigma}\exp(-t^2)\,\mathrm{erf}(\sqrt{2t}/\sigma)\,dt\right\}, \tag{4}$$

where erf(x) is the error function. By scanning the tip over the Z coordinate, we can find out how the yield Y and the function $f(h)$ depend on the test conditions. The AFM tip is moved by using a standard piezomotor while keeping the beam axis fixed.

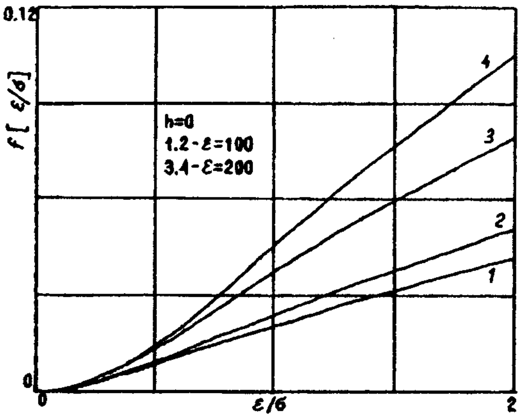

FIG. 3. The same as Fig. 2 for various values of ε/σ and $h=0$. Curves *1* and *3* are plotted for a parabolic tip with $\varepsilon=100$ and 200, and curves *2* and *4* are plotted for a conical tip.

Figure 2 shows theoretical dependences of $f(\varepsilon,\sigma,h)$ on the ratio h/σ for $\varepsilon=400$ and $\sigma=1000$, calculated according to formula (4). Curve *1* corresponds to a tip shaped as a paraboloid of revolution, while curve *2* corresponds to a cone, having the same height H and the base radius r. In the relative units used it is clear that $r=\sqrt{2\varepsilon}$. Figure 3 shows similar curves for $h=0$ and various values of ε and the ratios ε/σ. Curves *1* and *3* refer to a paraboloid and curves *2* and *4* refer to a cone.

By applying these results, shape of the tip can be reliably monitored using the experimentally measured dependence $f(\varepsilon,\sigma,h)$.

It should be noted that the real diameter of the diagnostic beam (actually, the standard deviation σ) need not necessarily be of the same order of magnitude as the tip height, since it is sufficient to use only part of the beam. This is also facilitated by the fact that the tip material usually differs from that of the AFM apparatus, so that the corresponding energy spectra are shifted relative to each other on the energy scale and are easily identified. Nevertheless, it is obviously desirable to use submicron beams and low current density. Such parameters have already been achieved in modern beam technology.

The problem of calculating the tip shape as a function of laser irradiation time and intensity is more complex (even if the angular dependence of the sputtering coefficient is known). This issue will be examined at a later date.

---

[1] V. S. Édel'man, Prib. Tekh. Éksp. No. 1, 24 (1991).

[2] D. Sarid, *Scanning Force Microscopy with Applications to Electric, Magnetic, and Atomic Forces* (Oxford University Press, New York, 1991).

[3] M. J. Vasile. D. A. Grigg, J. E. Griffith *et al.*, Rev. Sci. Instrum. **62**, 2167 (1991).

[4] L. C. Hopkins, J. E. Griffith, L. R. Harriott *et al.*, J. Vac. Sci. Technol. B **13**, 335 (1995).

Translated by R. M. Durham

Dry etching of aluminum nitride by an ion beam

D. M. Demidov, R. V. Leus, V. P. Chalyĭ

Center for Advanced Technology and Development, St. Petersburg

(Submitted February 5, 1997)
Pis'ma Zh. Tekh. Fiz. **23**, 1–6 (June 26, 1997)

A comparative study of the important problem of dry etching AlN by an ion beam has been carried out. The etching rate as a function of the parameters of the process has been determined for layers deposited by vapor-phase epitaxy and by magnetron sputtering. It is shown possible to form a specified relief (systems of mesa stripes) in AlN layers. It is demonstrated that this method can be used for smoothing the AlN surface. © *1997 American Institute of Physics.* [S1063-7850(97)01706-0]

One of the important problems in modern optoelectronics related to the production of semiconductor photodiodes and heterolasers in the blue-green region is the development of methods for forming profiled structures based on the group III nitrides, including AlN. The solution of this problem by the method of standard photolithography, based on the treatment of samples in liquid solutions is difficult because of the high chemical resistance of the nitrides. Therefore new methods are needed to form structures with a specified geometry.

The present paper reports an investigation of using a collimated ion beam for dry etching of AlN prepared by various methods.

For the etching we used a broad, partially neutralized collimated argon ion beam with an energy up to 1 keV. The ion source was mounted on the flange on the work chamber of a multifunctional vacuum apparatus. The distance between the emitter mesh of the source and the sample was ~80 mm. The sample was placed on a rotating pedestal. The rate of rotation of the pedestal during the etching was 100 rpm. The angle of incidence of the ion beam could be varied from 0 to 90 degrees.

For purposes of comparison we used the following materials as test samples for the method: single-crystal AGNK-3 gallium arsenide with the (100) orientation, a layer of aluminum nitride grown on leukosapphire substrates by reactive magnetron sputtering at 600 °C, and by vapor-phase deposition in a chloride system at 1100 °C. The AlN layers prepared by magnetron sputtering were polycrystalline with a great deal of surface roughness, as much as 3000 Å. The layers grown by vapor-phase epitaxy were highly textured. An x-ray structural analysis of these layers, carried out on a DRON-2 diffractometer (Cu_α radiation) revealed reflections only from the surfaces perpendicular to the ⟨0001⟩ direction.

First, we investigated how the dry etching of crystals depended on the parameters of the process. In all samples the etching depth increased linearly with time, which indicates that the etching rate is constant. The etching rate of GaAs and of polycrystalline and highly textured layers of AlN as a function of the accelerating voltage for a constant ion current of 14 mA was measured. One of these curves taken for polycrystalline AlN is shown in Fig. 1. As one can see from this figure, the etching rate varies linearly with the accelerating voltage in the range 300–1000 V, and as the voltage is lowered below 300 V, the etching rate falls off sharply, going to zero at $U \approx 50$–70 V. This dependence agrees with the theoretical notions of the cascade mechanism of sputtering of a

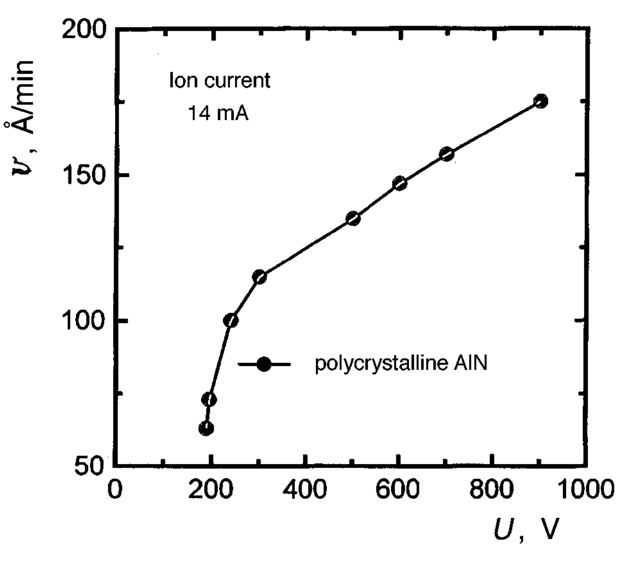

FIG. 1. Rate of etching aluminum nitride versus the accelerating voltage.

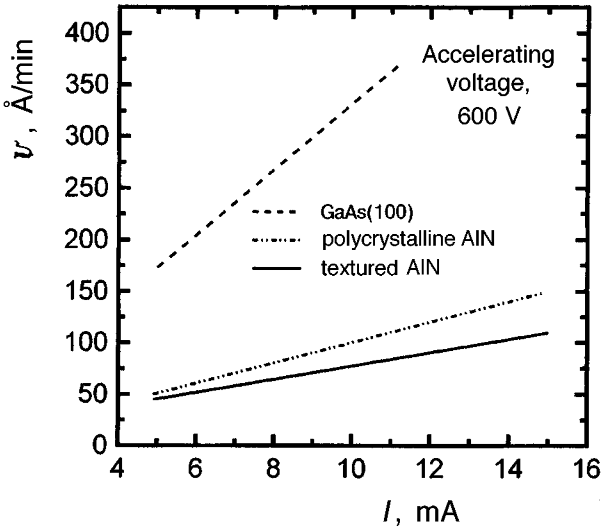

FIG. 2. Rate of etching gallium arsenide and aluminum nitride prepared by different methods versus the ion beam current.

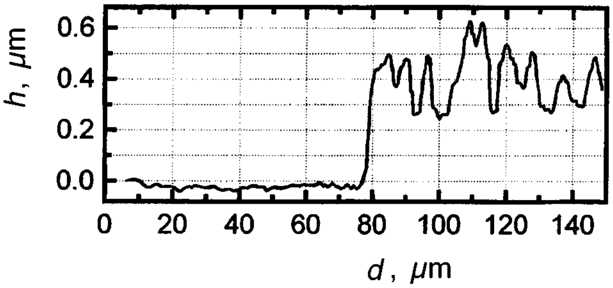

FIG. 3. Profilometer curve of the surface layer of aluminum nitride after etching (left side) and the unetched part (the right side).

surface, characteristic of this range of incident ion energy.[2,3] In turn, this result implies that there are very few high-energy ions in the beam.

In Fig. 2 we show the etching rate of GaAs and AlN layers versus the ion beam current and a constant accelerating potential of 600 V. In the entire range of current we observed a linear increase in the etch rate. The etching rates of these materials for identical beam characteristics are naturally quite different, and for a current of 10 mA are ~330 Å/min for GaAs, ~100 Å/min for polycrystalline AlN, and ~75 Å/min for textured AlN.

We have tested the possibility of smoothing the AlN surface by ion beam etching. For this purpose we used an AlN film grown by magnetron reactive sputtering, with a great deal of surface roughness. The etching was carried out through a photoresist mask. In Fig. 3 we show the profilometer curve of the AlN surface after etching (the left-hand part) and the part covered by the mask during the etching (the right-hand part). This figure shows that the characteristic surface roughness size after the etching had diminished from ~ 0.3 μm to tens of angstroms.

This method of ion etching was used for creating relief on the surface of a layer of textured AlN. For this purpose we used a photoresist mask with dimension 5 μm every 3 μm, through which the AlN layer was dry-etched to a depth of ~2 μm to form a system of mesa stripes. Figure 4 shows a photomicrograph of the cleaved structure after etching and removal of the photoresist mask.

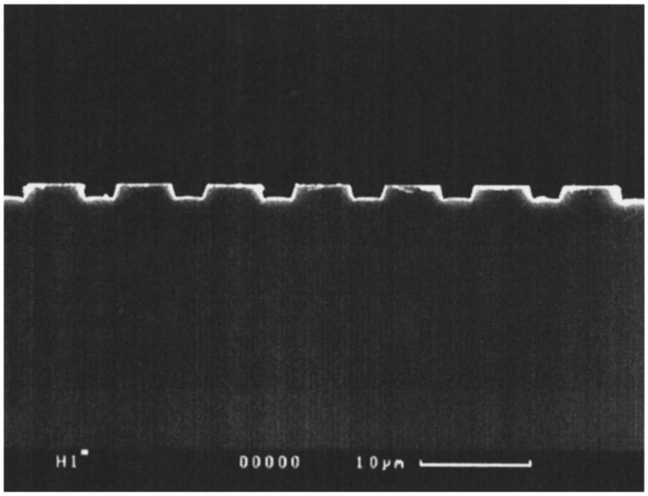

FIG. 4. Photomicrograph of the cleaved section of a structure with mesa stripes formed in a layer of aluminum nitride.

The following conclusions can be drawn on the basis of these investigations:

— The method of etching permits us to form relief on the AlN surface and smooth the roughness of the surface.

— The etching rate depends on the method used to deposit AlN and the degree of its crystallization.

This work was performed with the support of the Russian Fund for Fundamental Research (Grant No. 96-02-17203).

[1] H. Morkoc, S. Strite, G. B. Gao, M. E. Lin, B. Sverdlov, and M. Burns, J. Appl. Phys. **76**, 1363 (1994).
[2] P. G. Glöersen, J. Vac. Sci. Technol. **12**, 28 (1975).
[3] G. F. Ivanovskiĭ and V. I. Petrov, *Ion-Plasma Treatment of Materials* [in Russian] (Radio i Svyaz', Moscow, 1986).

Translated by J. R. Anderson

Functional properties of silicon/non-native-oxide heterostructures

E. A. Tutov, S. V. Ryabtsev, and E. N. Bormontov

Voronezh State University

(Submitted December 27, 1996)
Pis'ma Zh. Tekh. Fiz. **23**, 7–13 (June 26, 1997)

It is shown possible to use Al/SnO_2/Si and Al/WO_3/Si metal–oxide–semiconductor structures as photodiodes with a large-area heterojunction. For structures with a film of amorphous tungsten trioxide (a-WO_3) they show promise for applications associated with the development of varicaps and photovaricaps and also chemical sensors of the capacitance type. © *1997 American Institute of Physics.* [S1063-7850(97)01806-5]

In addition to the general trend to miniaturization of the elements used in electronics, there exists a steady need for large-area structures, such as photodetectors, displays, and sensors for ''artificial smelling.''

The unique qualities of c-Si/SiO_2 heteroboundaries make this system the basis of modern semiconductor microelectronics.[1] The combination of the highly developed silicon technology plus the use of other oxide layers, including nonideal insulators, makes it possible to greatly diversify the functional properties of these structures.

Films of tin dioxide are used as transparent conductors, the functional layers of heaters, and chemical sensors. The high sensitivity of the electrophysical and optical properties of tungsten trioxide to the stoichiometry (deficiency in the anion sublattice and the presence of interstitial cations in the structural interstitial sites) is the prerequisite for using this material as the active layer in sensors, indicating devices, and photoelectrochemical devices.

Silicon heterostructures with thin a-WO_3 films have been previously studied,[2–7] where the main problems were to determine the various properties of the electrochromism, photochromism, and thermochroism in amorphous tungsten trioxide, and for which purpose the investigators exploited the high sensitivity of the electrophysical parameters of the heteroboundaries to the electronic processes taking place in the oxide layer. Besides providing basic information, this structure has functional possibilities of independent interest.

This paper reports a study of some electrophysical characteristics of the metal/oxide/semiconductor structures Al/SnO_2/Si and Al/WO_3/Si. In either case the disordered structure of the oxide film governs their main characteristics, the surface properties are more important than the bulk properties, they have a high ionic conductivity, and the mobility gap has a larger value (for a-WO_3).

The Al/a-WO_3/Si heterostructures were prepared by vacuum condensation of the thermally evaporated oxide and metal. The substrates were single-crystal silicon wafers, mostly of type KÉF-4.5 with the (001) orientation. The microcrystalline tin dioxide films were deposited by dc and rf magnetron sputtering. The thickness of the oxide layers varied between 50 and 500 nm. The area of the upper electrode of the test structures was 0.5×1.0 mm. The correlation between the method of preparation and the local order and structure of the films has been discussed in, e. g., Refs. 8 and 9. The current–voltage characteristics and high-frequency capacitance–voltage characteristics were measured by the usual methods, as described in Refs. 4 and 10.

In Fig. 1a we present the reverse branches of the current–voltage characteristics of the WO_3/Si and the SnO_2/Si structures. Illumination with white light with a specific power of 0.01 W/cm^2 causes changes in the current–voltage characteristics, as is usual for photodiodes. Investigation of their spectral sensitivity showed that the photovoltaic effect is mainly due to the generation of photocarriers in the silicon (the peak of the photocurrent lies in the near infrared).

Because of the high resistance of the oxide layers, the absolute values of the photocurrent in both structures is insufficient for practical utilization for solar energy. However, for special-purpose photodiodes the possibility of obtaining large-area heterojunctions and its illumination through a transparent oxide layer is regarded as a definite advantage.[10]

The capacitance of the WO_3/Si structure also varies not only with the applied voltage, but also with the illumination, which is the physical basis for its operation as a varicap or a photovaricap. In Fig. 1b we show the high-frequency capacitance–voltage characteristics for the case of a p-Si substrate. We note that the capacitance tuning ratio (in the present case ~ 5) can be even higher than 10 (Refs. 2 and 5), which is much higher than, for example, the characteristics of similar Al/Sm_2O_3/Si structures[11] for a comparable slope of the capacitance–voltage characteristic.

For the structure with the SnO_2 film the higher conductance of the oxide layer did not permit us to measure the equilibrium capacitance–voltage characteristics.

The possibility of using these diode structures as gas (photo) detectors in a manner similar to that of Refs. 12 and 13 will be the object of a separate investigation. Here we only note that the WO_3/Si structures can operate as a capacitance-type chemical sensor.

An a-WO_3/Si heterostructure was used in Refs. 4 and 5 for studying the properties of the photochromism and electrochromism in thin films of amorphous tungsten trioxide. The electrophysical parameters of the a-WO_3/Si heterostructures are distinguished by their high sensitivity to the stoichiometry of the oxide layer. In essence, the change in the capacitance–voltage characteristic in these processes demonstrates the operation of this structure as a chemical sensor of hydrogen (Fig. 2a).

Double injection of electrons and protons from an elec-

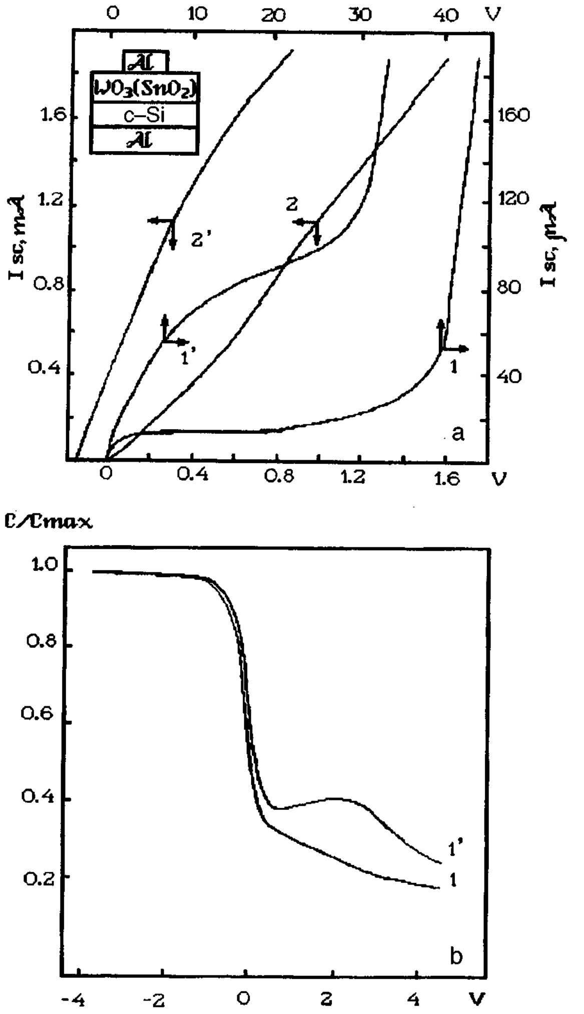

FIG. 1. a — Dependence of the short-circuit current I_{sc} on the reverse bias V for Al/WO$_3$/*n*-Si and Al/SnO$_2$/*n*-Si heterodiodes in the dark and with illumination (curves *1*, *1'* and *2*, *2'*, respectively); b — high-frequency capacitance–voltage characteristics of the Al/*a*-WO$_3$/*p*-Si heterostructure in the dark (*1*) and with illumination (*1'*). The frequency of the test signal is 1 MHz, the amplitude is 20 mV.

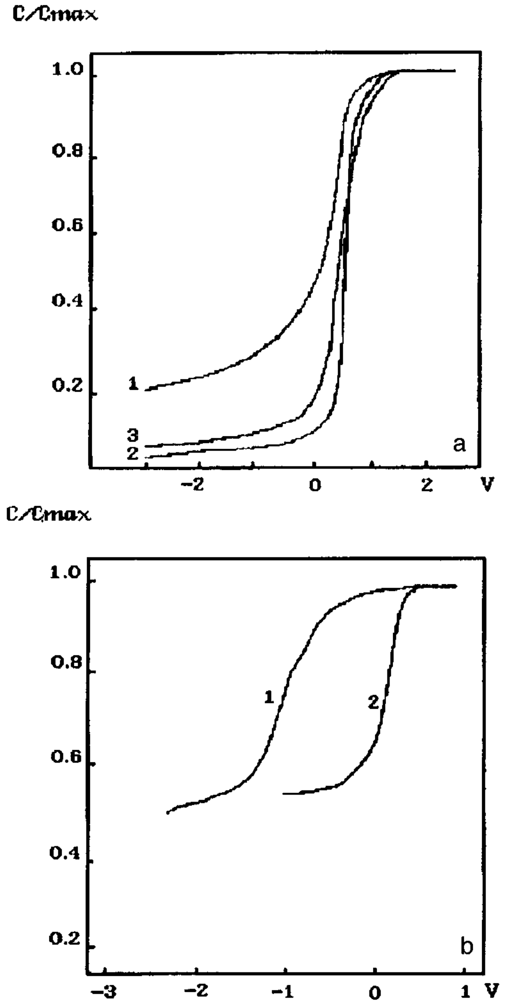

FIG. 2. a — High-frequency capacitance–voltage characteristics of an Al/*a*-WO$_3$/*n*-Si heterostructure (*1*) and its change with the injection of hydrogen into the tungsten trioxide in photochromism (*2*) and electrochromism (*3*) processes; b — high-frequency capacitance–voltage characteristic of an Al/*a*-WO$_3$/*n*-Si heterstructure before (*1*) and after (*2*) storage in saturated ethanol vapor for a day.

trolyte or photoinjection of hydrogen by ultraviolet irradiation results in a partial reduction of WO$_3$ and places the tungsten ions in the lowest oxidation state (+5). This causes an increase in the density of negative effective charge and a corresponding shift of the capacitance–voltage characteristic of metal/oxide/semiconductor structure. In the photochromism and electrochromism processes hydrogen is injected into the structural voids of WO$_3$, which causes corresponding energy reorganizations[5] leading to the formation of hydrogen-tungsten bronze.[14] This oxidation-reduction reaction is reversible.

It is known that *a*-WO$_3$ films chemisorb water[8] and other hydrogen-containing substances that are photochromism enhancers — alcohols, aldehydes, and others, whose split-off protons lead to consequences similar to those due to the direct injection of hydrogen (Fig. 2b).

The capacitance–voltage characteristics were measured at room temperature, where the kinetics of the adsorption-desorption processes are unsuitable for the practical detection of gases (taking hours), and therefore Fig. 2b only shows the maximum possible change in the capacitance of the *a*-WO$_3$Si structure in the presence of ethanol vapor.

An important feature of amorphous tungsten trioxide as the active layer for sensors of hydrogen and hydrogen-containing compounds is the bulk mechanism of the process, which permits operation over a broad range of concentrations, and the high degree of porosity of the film and the large surface-to-volume ratio, which provides fast operation at relatively low temperatures.

The amorphous tungsten trioxide films exhibit more pronounced electrochromism or sensor properties, but the thermodynamic instability is the main reason for time-dependent degradation of its characteristics (the ''aging'' effect[8]). This problem may be partly solved by preparing polycrystalline films with a specified texture,[14] in which the high ionic conductivity characteristic of *a*-WO$_3$ are preserved.

The multifunctionality of these structures, which provide in principle the possibility of using a single material as the active layer in structures for different applications (transparent contacts, physical and chemical sensors, information visualization devices) is a potentially important achievement in the solution of the problem of their integration and combined technology.

[1] S. M. Repinskiĭ, Poverkhn. Fiz. Khim. Mekh. No. 7–8, 12 (1995).

[2] V. I. Kukuev, E. A. Tutov, É. P. Domashevskaya *et al.*, Zh. Tekh. Fiz. **57**, 1957 (1987) [Sov. Phys. Tech. Phys. **32**, 1176 (1987)].

[3] V. I. Kukuev, E. A. Tutov, M. V. Lesovoĭ *et al.*, Poverkhn. Fiz. Khim. Mekh. No. 11, 87 (1988).

[4] E. A. Tutov and A. A. Baev, Appl. Surf. Sci. **90**, 33 (1995).

[5] E. A. Tutov, V. I. Kukuev, A. A. Baev *et al.*, Zh. Tekh. Fiz. **65**(7), 117 (1995) [Tech. Phys. **40**, 697 (1995)].

[6] B. Sh. Galyamov, I. E. Obvintseva, and Yu. E. Roginskaya, Pis'ma Zh. Tekh. Fiz. **14**, 253 (1988) [Sov. Tech. Phys. Lett. **14**, 113 (1988)].

[7] B. Sh. Galyamov, I. E. Obvintseva, Yu. E. Roginskaya, and M. I. Yanovskaya, Pis'ma Zh. Tekh. Fiz. **15**(2), 74 (1989) [Sov. Tech. Phys. Lett. **15**, 69 (1989)].

[8] V. I. Kukuev, E. A. Tutov, M. V. Lesovoĭ, and É. P. Domashevskaya, Kristallographiya **33**, 1551 (1988) [Sov. Phys. Crystallogr. **33**, 926 (1988)].

[9] V. I. Kukuev, E. A. Sorokina, Yu. Ya. Tomashpol'skiĭ *et al.*, Izv. Ross. Akad. Nauk Neorg. Mater. **31**, 342 (1995).

[10] E. A. Tutov, A. A. Baev, S. V. Ryabtsev, and A. V. Tadeev, *Abstracts of the E-MRS Spring Meeting*, Strasbourg, France, 1995, B/P39.

[11] V. A. Rozhkov, A. Yu. Trusova, I. G. Berezhnoĭ, and V. P. Goncharev, Zh. Tekh. Fiz. **65**(8), 183 (1995) [Tech. Phys. **40**, 849 (1995)].

[12] G. G. Kovalevskaya, M. M. Meredov, E. V. Russu *et al.*, Zh. Tekh. Fiz. **63**(2), 185 (1993) [Tech. Phys. **38**, 149 (1993)].

[13] S. V. Slobodchikov, G. G. Kovalevskaya, and Kh. M. Salikhov, Pis'ma Zh. Tekh. Fiz. **20**(10), 66 (1994) [Tech. Phys. Lett. **20**, 417 (1994)].

[14] A. I. Gavrilyuk, V. G. Prokhvatilov, and F. A. Chudnovskiĭ, Fiz. Tverd. Tela (Leningrad) **24**, 982 (1982) [Sov. Phys. Solid State **24**, 558 (1982)].

Translated by J. R. Anderson

Solitons in disperse systems with electric double layers

E. G. Fateev

Institute of Applied Mechanics, Ural Division of the Russian Academy of Sciences, Izhevsk

(Submitted January 17, 1997)
Pis'ma Zh. Tekh. Fiz. **23**, 14–18 (June 26, 1997)

An investigation is made of the behavior of disperse systems with electric double layers in external time-dependent electric fields, taking into account the interaction between the moving concentrated charges in the shells of the neighboring grains. It is shown that an external electromagnetic excitation at ultralow frequencies can be transmitted to the bulk of a disperse system in the form of solitary waves. It is proposed that the real observation of these waves is possible, for example, in disperse systems with nonconducting spherical inclusions having thin liquid shells and suspended in a solid insulator. *© 1997 American Institute of Physics.* [S1063-7850(97)01906-X]

In disperse systems consisting of a collection of cells with nonconducting spherical inclusions (grains) having thin liquid or quasiliquid conducting shells, suspended in a solid insulator, one can observe giant values of the permittivity at ultralow frequencies.[1,2] Similar kinds of phenomena are also possible in other types of disperse systems. For the sake of simplicity the theories of this effect[1–4] have examined the behavior of charges in external time-dependent fields on no more than one cell. In going from a single cell to the bulk disperse system in the analysis of the electromagnetic response to an external interaction, one must take into account the interaction among the moving concentrated charges in the shells of the neighboring grains. It is clear that electromagnetic waves (charge density waves) can propagate in such systems of coupled oscillators. An analysis of this proposition is the subject of the present letter.

We consider a system of one-dimensional oscillators with uncompensated charges in the shells of disperse particles of radius r separated by a distance a from each other, as shown in Fig. 1. It is assumed that the ordering in the orientation of the charges is additive when the system is driven out of equilibrium, for example, after an electromagnetic field pulse on the first particle. Then the positive charges (we assume that they are considerably more mobile than the negative charges) deviate in particles *1–3* by the angles φ_{n-1}, φ_n, and φ_{n+1}. Let us consider the interaction between the charges and their surroundings in the Coulomb approximation. The expressions for the kinetic energy of the system of charges with masses $M_n = c_n m$ is

$$T_k = \frac{1}{2}\sum_n J_n \dot{\varphi}_n^2 . \tag{1}$$

Here $J_n = M_n r^2 = c_n m u r/\omega$ is the moment of inertia, u is the velocity, ω is the angular frequency of the oscillations, and c_n is the number of uncompensated charges (cations) of mass m in the shell of the nth particle. If we assume that the dissipative forces depend linearly on the velocity of the charges, then the corresponding dissipative function with the dissipation parameters α takes the form

$$D = \frac{1}{2}\sum_n \alpha \dot{\varphi}_n^2 . \tag{2}$$

The potential energy of the interacting charges in this system is expressed as the relation

$$U_{\text{int}} = -\frac{Q^+Q^+}{4\varepsilon\varepsilon_0\pi}\sum_n \left\{ \frac{1}{[a - r(\sin\varphi_{n-1} - \sin\varphi_n)]} - \frac{1}{[a - r(\sin\varphi_n - \sin\varphi_{n+1})]} \right\} . \tag{3}$$

Here ε is the permittivity of the medium between the charges with the shells and ε_0 is the permittivity of free space. If the deviations of the charges from their equilibrium positions are assumed to be small (i. e., $\sin\varphi_n \approx \varphi_n$), then relation (3) for a chain of oscillators can be written as

$$U_{\text{int}} = -B\sum_n (\varphi_{n+1} + \varphi_{n-1} - 2\varphi_n), \tag{4}$$

where $B = (Q^+)^2 r/4\pi\varepsilon\varepsilon_0 a^2$. The local energy of interaction of the oscillating charges Q^+ with the surrounding field created by the concentrated charges Q^- external to the shells (see Fig. 1) is given by the expression

$$U_l = -A\sum_n \cos\varphi_n , \tag{5}$$

where $A = Q^+Q^-/4\pi\varepsilon\varepsilon_0 a^2$. The Lagrangian for this system is

$$Z = T_k - U_{\text{int}} - U_l . \tag{6}$$

Let us assume that a time-dependent force $F(x,t)$ acts on the model system. Then, using the Euler-Lagrange equation (2) including dissipation, we find the following nonlinear equation of motion for the function (6) in the continuum approximation $na \to x$, $\varphi_n(t) \to \varphi(x,t)$

$$\frac{\partial^2\varphi}{\partial t^2} - \nu_0^2\frac{\partial^2\varphi}{\partial x^2} + \omega_0^2 \sin\varphi + \eta\frac{\partial\varphi}{\partial t} = \gamma(x,t). \tag{7}$$

The maximum velocity of propagation of the excitations in this system is $\nu_0 = (aB/J)^{1/2}$ the plasma frequency is $\omega^2 = (A/J)^{1/2}$, the perturbation is $\gamma(x,t) = F(x,t)/J$ and the coefficient corresponding to the dissipation level is $\eta = \alpha/J$.

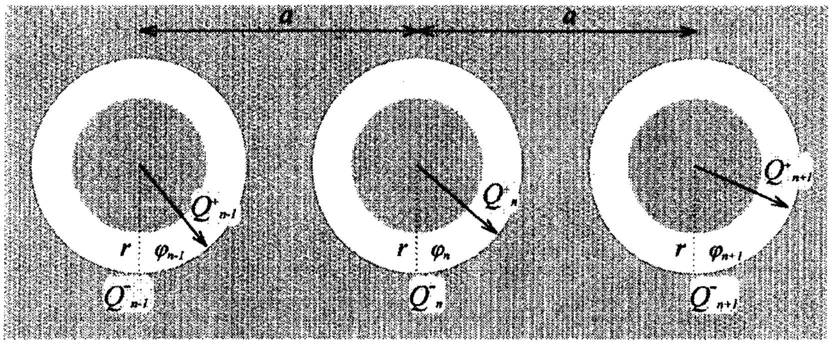

FIG. 1. System of oscillators, showing the oscillations of the charges in the shells (the usual shell thickness is 10–100 Å) around the particles with diameters $2r$, separated by a distance a.

Expression (7) is the well-known perturbed sine-Gordon equation, which has soliton solutions. The sine-Gordon equation is found everywhere, and can describe wave propagation in ferromagnets, Josephson transmission lines, superionic conductors, the behavior of charge density waves, etc. (see, e.g., Refs. 5 and 6). It is clear that in the present case as well, many interesting features of the behavior of solitary waves in disperse systems can be similar to those found in the most diverse media.[5,6] However, the behavior of solitons in disperse systems can exhibit unusual properties, associated with the possible giant soliton-like excitations. The lithosphere can be cited as an example of a giant disperse system saturated with fluids.[2]

Let us consider in this discussion the type and the dimensions of a disperse system in which one may observe these waves. An ideal model would be that of immobile spherical inclusions with liquid or quasiliquid shells, suspended in a solid insulator and separated by a distance $a \sim 3r$. It is assumed that the ions can migrate and diffuse freely along the surface of the inclusion in the shell. It is also assumed that the exchange of charge carriers in the shells with the dielectric matrix is negligible. The characteristic frequencies at which this system has a high permittivity is given by the relation $\nu = 2D/r^2$ (Ref. 2) and for an inclusion size $r \sim 10^{-5}$ cm and ordinary ion diffusion coefficients $D \sim 10^{-4}$–10^{-6} cm^2/s this frequency is in the range $\nu \sim 10^{-4}$–10^{-6} Hz. The solution of the sine-Gordon equation can be correct if the characteristic length in the medium is not less than the size $2a$ of an elementary cell, consisting of at least two grains, that is, $\lambda = 2\pi\nu_0/\omega_0 > 2a$ (Ref. 7). To these characteristic dimensions correspond the plasma frequencies $\omega_0 < \pi\nu_0/r \sim 10^1$–$10^6$ rad/s for $\nu_0 \sim 10^{-2}$–10^3 m/s. This assumption agrees with estimates of the charge density per unit volume of the shell, $c_n < 10^{22}$ charges/m^3 (Ref. 2). The corresponding uncompensated charge in the shell of a grain of size $r \sim 10^{-3}$–10^{-4} m can be of the order of $Q^+ \approx c_n q \sim 10^{-12}$–$10^{-9}$ C. Here $q \sim 1.6 \times 10^{-19}$ C is the elementary charge.

Using the concept of the balance of power entering into and dissipated in the system, as described by the perturbed sine-Gordon equation (7) (Refs. 5 and 8), one can find the steady-state velocity of the waves as a function of the perturbation amplitude F, the dissipation α, and the plasma frequency ω_0 in the form $\nu \approx \nu_0\{1 + (4\omega\alpha/F\pi)^2\}^{-1/2}$. It follows from this relation that for any perturbation power, the maximum velocity in a system of uncompensated charges $Q^+ \sim 10^{-12}$ C and inclusion radius $r \sim 10^{-3}$–10^{-4} m does not exceed $\nu_0 \sim 10^3$–10^4 m/s. The characteristic length is about $\lambda \sim 1$–10 cm if there is no appreciable concentrated charge Q^- near the grain. Thus the solution of the sine-Gordon equation can be correct for disperse systems of nearly any inclusion size.

In conclusion, it should be noted that because of the possibility of giant ultralow frequency of the permittivity in such disperse systems, the nature of the soliton-like formations in them can be nontrivial. A possible consequence is also a decrease in the threshold for mechanical stability of dehydrating solid compounds in external electric fields of ultralow frequency.[9–11]

[1] S. S. Dukhin and V. N. Shilov, *Dielectric Phenomena and the Double Layer in Disperse Systems and Polyelectrolytes* [in Russian] (Naukova Dumka, Kiev, 1972).
[2] T. L. Chelidze, A. I. Derevyanko, and O.D. Kurilenko, *Electrical Spectroscopy of Heterogeneous Systems* [in Russian] (Naukova Dumka, Kiev, 1977).
[3] Yu. B. Barkovskaya and V. N. Shilov, Kolloid. Zh. **54**(2), 43.
[4] V. N. Shilov, O. A. Shramko, and T. S. Simonova, Kolloid. Zh. **54**(4), 208.
[5] *Solitons in Action*, edited by K. Lonngren and A. Scott (Academic Press, New York, 1978) [Russ. transl., Mir, Moscow, 1981].
[6] R. K. Dodd, J. C. Eilbeck, J. Gibbon, and H. C. Morris, *Solitons and Nonlinear Wave Equations* (Academic Press, New York, 1982) [Russ. transl., Mir Moscow, 1988].
[7] J. F. Currie, S. E. Trullinger, A. R. Bishop, and J. A. Krumhansl, Phys. Rev. B **15**, 5567 (1977).
[8] A. Ferringno and S. Pace, Phys. Lett. A **112**, 77 (1985).
[9] E. G. Fateev, Pis'ma Zh. Tekh. Fiz. **19**(10), 48 (1993) [Tech. Phys. Lett. **19**, 313 (1993)].
[10] E. G. Fateev, Zh. Tekh. Fiz **66**(6), 93 (1996) [Tech. Phys. **41**, 571 (1996)].
[11] E. G. Fateev, Dokl. Akad. Nauk Ross. Akad. Sci. [Phys. Dokl.] (in press).

Translated by J. R. Anderson

Appearance of molecular hydrogen in the ultraviolet spectra of diamond-like carbon

B. R. Namozov, É. A. Smorgonskaya, M. P. Korobkov, and V. I. Ivanov-Omskiĭ

A. F. Ioffe Physicotechnical Institute, Russian Academy of Sciences, St. Petersburg

(Submitted February 24, 1996)
Pis'ma Zh. Tekh. Fiz. **23**, 19–24 (June 26, 1997)

Ultraviolet Raman scattering is used to study the state of hydrogen in diamond-like α-C:H. Scattering lines are observed corresponding to transitions between the rotational states of the hydrogen molecule. The interaction with the α-C:H matrix increases the internuclear distance and perturbs the electronic-vibrational terms of the H_2 molecule, so that resonance Raman scattering can be observed, excited by 10.04 eV photons. © *1997 American Institute of Physics.* [S1063-7850(97)02006-5]

Many of the remarkable properties of diamond-like carbon (α-C:H) are associated with incorporated hydrogen, which can enter into the disordered carbon matrix in various states: chemically bound or free atoms, free molecules, etc. While the bound hydrogen can be detected by the infrared vibrational spectra without difficulty,[1] the problem of observing free hydrogen in thin films of α-C:H is complicated by the inadequate sensitivity of the NMR spectrometer or the Raman spectrometer in the visible range (in the absence of resonance). Recently we reported on an investigation of the equilibrium of the bound and free hydrogen in bulk α-C:H (Ref. 2), but the state of the free hydrogen was still unknown. In the present communication we present experimental results that show that α-C:H contains molecular hydrogen.

The layers of α-C:H were prepared by magnetron sputtering of a graphite target in an argon–hydrogen (4 : 1) plasma at a pressure of about 10 mTorr in the work chamber. The temperature of the substrate (fused quartz or single-crystal silicon) was up to 200 °C. The argon ion energy was about 100 eV. For primary monitoring of the films we measured the infrared transmission in the region of the vibrational frequency of the C–H bond by means of a Specord 751IR two-beam spectrometer. A portion of a typical absorption spectrum in the neighborhood of the C–H stretch frequency is shown in the inset to Fig. 1. The structure of the bands is very typical of diamond-like carbon, and indicates the breaking of sp^3 bonds in the material.

To study the spectral characteristics of the hydrogen in the α-C:H films we used the method of resonance Raman scattering. The experimental setup included a vacuum cryostat of the contact type combined with a Seya-Namioka vacuum monochromator with a reflection angle of 70°. The monochromator employed a novel ruled elliptical diffraction grating with a variable line spacing to reduce astigmatism and coma. With a relative aperture of 1:8 and a reciprocal dispersion of 13.2 Å/mm, this grating gives a resolution of 0.25 Å in the operating range of the monochromator, 900–3000 Å. The measuring channel employed an FÉU-142 photomultiplier and a photon counting system. The excitation sources were KsR-2P and KrR-2P xenon and krypton lamps. The radiation spectra of these lamps contain mainly the intense ($\sim 10^{14}$ photons/s) resonance lines of xenon at 1470 Å and krypton at 1236 Å, which allowed us to place the lamps directly at the external window of the cryostat without any preliminary monochromatization. To record the scattered light the samples were placed in such a way that the ray reflected specularly from the surface was displaced relative to the slit in the blackened cavity of the entrance unit of the monochromator.

Figure 1 shows a graph of the light scattered from an α-C:H sample 1 μm thick, measured at room temperature. It took about 500 seconds to accumulate each point, for a dark count of 1–2 counts per second in the photomultiplier.

The main result is the observation of two distinct peaks of scattered light in the wings of the excitation line at 1236 Å (Kr) symmetrically disposed about the center by 550 cm^{-1}. In addition, weaker lines at 780 and 960 cm^{-1} are observed in the anti-Stokes spectrum. The resolution in the measurements was ± 20 cm^{-1}. Thus the observed scattering spectrum shows one Stokes and three anti-Stokes components. We note that at room temperature the lowest-energy anti-Stokes line at 550 cm^{-1} is somewhat elevated compared to the corresponding Stokes line. At 80 K the Stokes and anti-Stokes scattering lines are equal in amplitude.

The scattered lines are about two orders of magnitude lower in intensity than the excitation line at 1236 Å (Kr). A careful study of the shape of the other excitation line at 1470 Å (Xe) did not reveal any such structure on the wings upon scattering from the sample. Control measurements of scattering from glass substrates on which the layers of α-C:H were subsequently deposited also did not reveal any such features on the wings, either with krypton or with xenon excitation.

To interpret these results, let us note the proximity of the krypton excitation line (1236 Å, photon energy $\hbar\omega_{\mathrm{ex}} = 10.04$ eV) to the energy gap between the ${}^1\Sigma_g^+$ ground state and the ${}^1\Sigma_u^+$ excited electron terms of the H_2 molecule, which, with allowance for the zero-point vibrations is ~ 10.93 eV (Ref. 3). It may be supposed that because of the van der Waals interaction of the molecular hydrogen with the medium, a change occurs in its electronic terms. As a result it becomes possible at the wavelength 1236 Å to observe resonance Raman scattering by the H_2 molecules that interact with the structural elements of the main matrix of the diamond-like carbon. In other words, the hydrogen molecules entering into the medium become quasifree. The scales of the ''reorganization'' of the ground state of the free H_2 molecule in α-C:H can be estimated from a comparison

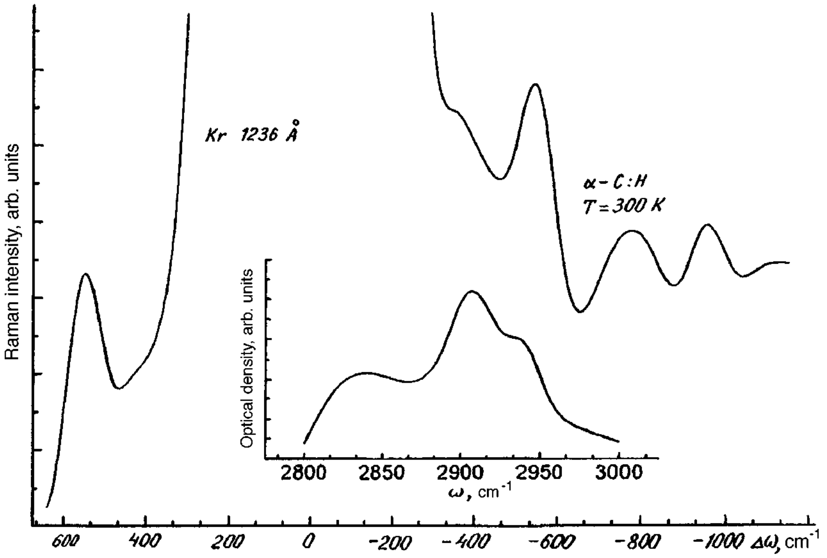

FIG. 1. Raman scattering spectra of α-C:H films at room temperature (film thickness 1 μm). The inset shows a portion of the infrared absorption spectrum in the region of the stretch vibrations of the C–H bond.

of the observed resonance Raman scattering spectrum with published data on Raman scattering of gaseous molecular hydrogen.

In the paper of Stoicheff[4] results were presented of an investigation of Raman scattering in gaseous H_2. The resonance Raman scattering spectrum observed by us is located principally in the region of the anti-Stokes frequencies. Nonetheless, one can readily see the similarity between the spectrum from Ref. 4 and that shown in Fig. 1 from the frequency shifts in the scattered line relative to the excitation line. The data of Ref. 4 indicate that these shifts for H_2 in the gas phase are 354, 587, 814, and 1034 cm^{-1} and correspond to the (2–0), (3–1), (4–2), and (5–3) transitions between the rotational sublevels of the electronic-vibrational ground state.

In the H_2 molecule the rotational states closest in energy differ in the total angular momentum J by 2: the parahydrogen molecule has even values of J and the orthohydrogen molecule has odd values (see, e.g., Ref. 5). In accordance with the selection rule for linear molecules, the transitions with $\Delta J = \pm 2$ should appear in the rotational Raman spectrum,[6] so that in the H_2 molecule transitions between sublevels with even J (parahydrogen) and with odd J (orthohydrogen) will be observed in the Raman scattering spectrum.

In the present case, the frequency shift with scattering are 550, 780, and 960 cm^{-1}, i.e., they differ from those listed above by about 5%. The (2–0) transition, which corresponds to a Raman scattering frequency 354 cm^{-1}, was not seen because of the strong Rayleigh broadening of the 1236 Å excitation line by the inhomogeneous film. From the comparison one can see that the anti-Stokes frequencies of 550, 780, and 960 cm^{-1} we observed correspond to the (1–3), (2–4), and (3–5) transitions between the rotational sublevels of the electronic-vibrational ground state of the para- and orthohydrogen molecules with $\Delta J = +2$. We naturally attribute the Stokes line at 550 cm^{-1} to the (3–1) transition in the orthohydrogen molecule for $\Delta J = -2$.

On the basis of this interpretation of the experimental data we can use the simple model of a rigid rotator to estimate the rotational constant $B = \hbar / m r^2$ in the expression for the rotational energy of a molecule, $E_r = BJ(J+1)$, and consequently the internuclear spacing r in the electronic-vibrational ground state of the molecule. (Here m is the mass of the hydrogen atom). We find that the values of B calculated for all three observed frequency shifts agree with good accuracy and average out to $B = 54.7$ cm^{-1}. This value is about 10% lower than that for gaseous H_2 (60.85 cm^{-1}; Ref. 3). From our estimates, the average internuclear distance in the H_2 molecule embedded in the α-C:H matrix is 0.782 Å. In gaseous H_2 this distance is $r_e = 0.7414$ Å (Ref. 3). This appreciable increase in r compared to r_e is due to the interaction of the H_2 molecule with the α-C:H matrix, which results in an effective elongation of the molecule, which increases its moment of inertia and reduces the rotational frequency. We note that because of the elongation of the molecule one might also expect a reduction in its characteristic vibrational frequencies.

In this situation the energy of the electronic transitions are decreased in the molecule, which, because of the interaction with the medium are in an excited state relative to the completely free molecules in the gas. This means that the energy of the excitation photon, $\hbar \omega_{\text{ex}} = 10.04$ eV (Kr) is very close to the energy of the corresponding electronic transition $^1\Sigma_g^+(\text{pert}) \rightarrow {}^1\Sigma_u^+(\text{pert})$ between the perturbed terms of molecular hydrogen. At the same time, the photon energy $\hbar \omega_{\text{ex}} = 8.44$ eV for the excitation line at 1470 Å (Xe) does not suffice for resonance at this transition. This result is evidence for the correctness of the statement above that at the 1236 Å line (Kr) we are observing resonance Raman scattering by the quasifree H_2 molecules embedded in the α-C:H matrix.

This work was supported by the Russian Fund for Fundamental Research (No. 96-02-16851) and partly by a grant from Arizona University.

[1] A. Grill, in *Synthetic Diamond: Emerging CVD Science and Technology*, edited by K. Spear and J. P. Dismukes (Wiley, New York, 1994).

[2] V. I. Ivanov-Omskiĭ, G. S. Frolova, and S. G. Yastrebov, Pis'ma Zh. Tekh. Fiz. [Tech. Phys. Lett.] (in press).

[3] *Handbook of Physical Quantities* [in Russian], edited by I. S. Grigor'ev and E. Z. Meĭlikhov, (Énergoatomizdat, Moscow, 1991).

[4] B. P. Stoicheff, Canad. J. Phys. **35**, 730 (1957).

[5] U. Fano and L. Fano, *Basic Physics of Atoms and Molecules* (Wiley, New York, 1959) [Russ. transl., Nauka, Moscow, 1980; pp. 540–550].

[6] M. M. Sushchinskiĭ, *Raman Scattering Spectra of Molecules and Crystals* [in Russian] (Nauka, Moscow, 1969), pp. 114–138.

Translated by J. R. Anderson

Energy transitions in CuIn(Te,Se)$_2$ chalcopyrite films near the fundamental absorption edge

V. V. Kindyak, A. S. Kindyak, and Ya. I. Latushko

Institute of Solid State and Semiconductor Physics, Belarus Academy of Sciences, Minsk

(Submitted January 10, 1997)
Pis'ma Zh. Tekh. Fiz. **23**, 25–30 (June 26, 1997)

The structure of the fundamental absorption edge in thin CuIn(Te,Se)$_2$ chalcopyrite films has been studied. Identifications are made of the energy transitions due to the splitting of the valence band by the tetragonal crystal field and the spin-orbit interaction. The concentration dependences of these transitions are determined [S1063-7850(97)02106-X]

Thin-film structures based on the chalcogenide compounds CuInSe$_2$ and CuInTe$_2$ have high absorption coefficients ($\alpha \approx 10^4$–10^5 cm^{-1}) and optimum band gaps $E_g \approx 1$ eV for making efficient solar cells,[1–5] while the solid solutions of CuIn(Te,Se)$_2$ (CITS) can be used not only as absorbing layers but as the intermediate layers for improving the mechanical and optical properties of the Mo/CuInSe$_2$ structure.[6] It would be of considerable interest to study the physical properties of thin CITS films, in particular their optical characteristics and the nature of the energy transitions in these materials near the fundamental absorption edge. There is little published information on the optical properties of thin CITS films because of the difficulty of preparing stoichiometric layers by standard deposition methods.

Previously we reported on the preparation of stoichiometric thin films of CuInSe$_2$, CuInTe$_2$, and CuIn(Te$_{0.15}$Se$_{0.85}$)$_2$ by pulsed laser deposition and a study of the structure of the absorption edge in these films.[7–10] In the present paper we present the results of an investigation of the photon energy dependence of the edge absorption of stoichiometric thin films of the chalcogenide CuIn(Te$_x$Se$_{1-x}$)$_2$ ($0 \leqslant x \leqslant 1$) (the stoichiometry is known with an accuracy of 2% from Rutherford backscattering measurements). The films were prepared by pulsed laser deposition in a manner similar to that described previously.[7–10] It was possible to determine how the transitions associated with direct allowed electron transitions from the valence band to the conduction band and transitions resulting from the splitting of the valence band by the tetragonal crystal field and the spin-orbit interaction depend on the composition of the CITS solid solutions.

The wavelength dependences of the reflection coefficient R and of the transmission T of the CITS films on glass substrates were measured at room temperature in the visible and near infrared (500–1700 nm) on Specord-61 NIR and Specord-UV-VIS spectrophotometers. For the measurements we used the standard reflection attachment with symmetric beam paths. The spectral resolution was ≈ 0.8 meV in the visible and 0.5 meV in the near infrared. The measurement error in the reflection coefficient was no more than 2%. The film thickness was ≈ 0.6 μm.

The optical constants of thin CITS films were found by solving the system of equations using the experimental data for $R(\lambda)$ and $T(\lambda)$ taking into account interference in the film/substrate system, and

$$T_{14} = \frac{1 - R_{12}}{1 - R_{12} R_a^1} \cdot T_a ,$$

$$R_{14} = \frac{R_{12} T_a^2}{1 - R_{12} R_a^1} + R_a . \tag{1}$$

Here $R_{12} = (n_2 - 1)^2/(n_2 + 1)^2$ is the Fresnel reflection coefficient at the film-air interface, $R_a = C/A$; $R_a^1 = B/A$; $T_a = 16 n_3 (n_2^2 + k_2^2)/A$; T_{14} and R_{14} are the measured transmission and reflection coefficients of the film- substrate system

$$A = \rho\tau \exp(\gamma k_2) + \delta\sigma \exp(-\gamma k_2) + 2S \cos(n_2\gamma) + 2t \sin(n_2\gamma),$$

$$B = \rho\sigma \exp(\gamma k_2) + \delta\tau \exp(-\gamma k_2) + 2q \cos(n_2\gamma) - 2r \sin(n_2\gamma),$$

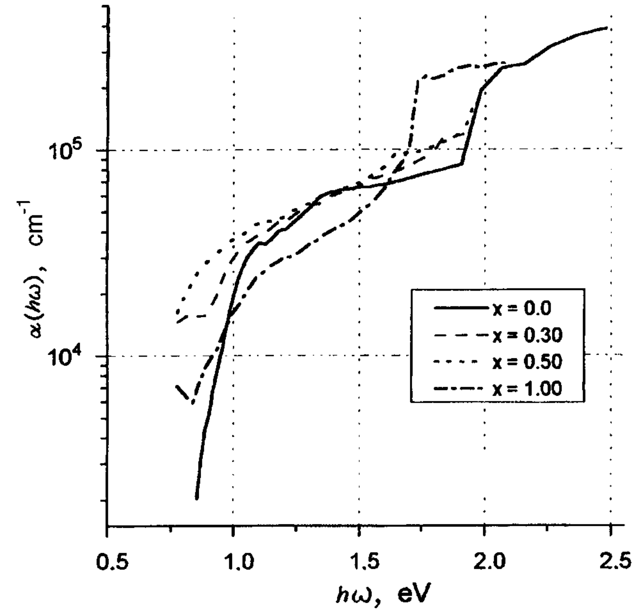

FIG. 1. Photon energy dependence of the absorption coefficient of thin films of CuIn(Te$_x$Se$_{1-x}$)$_2$.

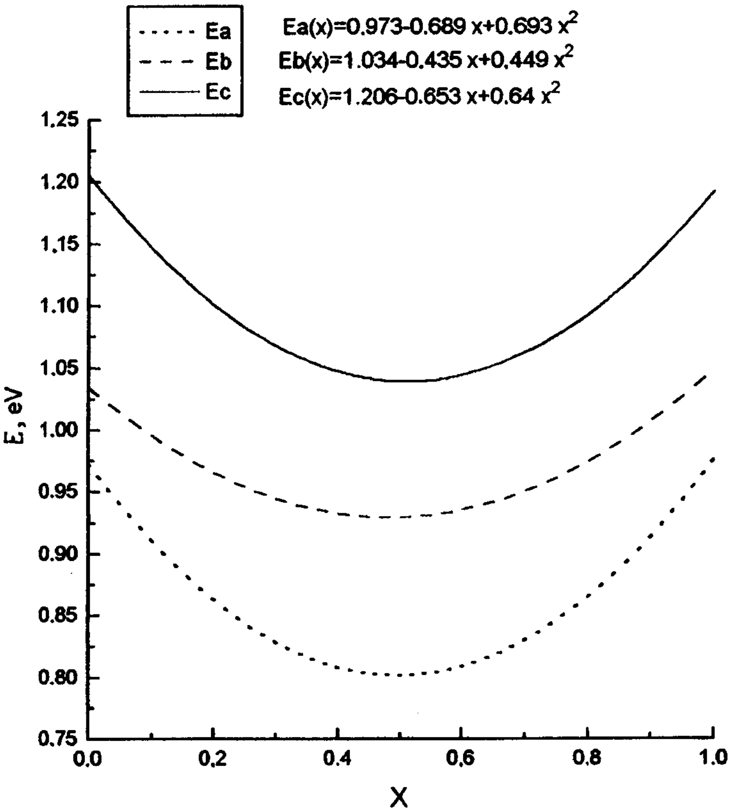

FIG. 2. Concentration dependence of the transitions E_A, E_B, and E_C.

$$C=\tau\sigma\ \exp(\gamma k_2)+\sigma\rho\ \exp(-\gamma k_2)+2q\ \cos(n_2\gamma)$$

$$+2r\ \sin(n_2\gamma),$$

$$\sigma=(n_2-n_3)^2+k_2^2,\quad \rho=(n_2+1)^2+k_2^2,$$

$$\tau=(n_2+n_3)^2+k_2^2,\quad r=2k_2(n_3-1)(n_2^2+k_2^2+n_3),$$

$$\delta=(n_2-1)^2+k_2^2,\quad t=2k_2(n_3+1)(n_2^2+k_2^2-n_3),$$

$$S=(n_2^2+k_2^2)(n_3^2+1)-(n_2^2+k_2^2)^2-n_3^2+4n_3k_2^2,$$

$$q=(n_2^2+k_2^2)(n_3^2+1)-(n_2^2+k_2^2)^2-n_3^2-4n_3k_2^2,$$

$$\gamma=4\pi d_2/\lambda.$$

The system of equations (1) were solved by an iteration method. It was assumed that the refractive index of the initial phase (n_1) and of the final phase (n_4) is unity, and that of the substrate is $n_3=1.5\pm 0.01$. The accuracy in the determination of n_2 and k_2 was ± 0.001. The absorption coefficient α was determined from the relation $\alpha=2\pi k/\lambda$.

An analysis of the curves of $\alpha(\omega)$ for the CITS films (Fig. 1) by the quasicubic model of $p-d$ hybridization of the valence bands in the chalcogenide compounds[11] showed that a large contribution to the structure of the edge absorption of the CITS films comes from direct allowed transitions, determined from the relations $(\alpha\hbar\omega)^2=A_n^2(\hbar\omega-E_{gn})$ in different energy intervals: E_A is the valence band-conduction band transition (Γ_7^v–Γ_6^c); E_B is the transition associated with the splitting of the valence band by the tetragonal crystal field, (Γ_6^v–Γ_6^c); E_C is the transition associated with the spin-orbit splitting of the valence band (Γ_7^v–Γ_6^c). The concentration dependences of the transitions E_A, E_B, and E_C are nonlinear, with a minimum for the equimolar composition of the solid solution (Fig. 2) and are described by the quadratic equations

$$E_A(x)=0.973-0.689x+0.693x^2,$$

$$E_B(x)=1.034-0.436x+0.449x^2,$$

$$E_C(x)=1.206-0.653x+0.64x^2.$$

The nonlinearity parameters C_A, C_B, and C_C are, respectively, 0.693, 0.449, and 0.64, and are determined here for the first time for CITS films. It might be suggested that the nonlinear nature of the composition dependence of E_A, E_B, and E_C of the CITS solid solutions may be related to the nonlinear properties of the crystal field of the solid solutions, but to verify this would require additional investigations by the pseudopotential method. It should be pointed out that the shape of the curve of E_A versus the composition of the solid solution with a minimum at $x=0.5$ for the films is in good agreement with the data of Ref. 12 for CITS crystal.

In conclusion we should note that the complex structure of the edge absorption in CITS thin films has been identified for the first time in this investigation.

The authors wish to thank V. F. Gremenek and I. A. Viktorov for preparing the films and determining their composition.

This work was financed by the Russian Fund for Fundamental Research (Grant No. F94-289).

[1] *Current Topics in Photovoltaics*, edited by T. J. Coutts and J. D. Meaken, (Academic Press, Orlando, 1985) [Russ. transl., Mir, Moscow, 1988].
[2] R. Diaz, M. Leon, and F. Rueda, Jpn. J. Appl. Phys. **31**, 3675 (1992).

[3] H. Neumann, B. Perlt, Hörig, and G. Kuhn, Thin Solid Films **182**, 115 (1989).
[4] J. Hedstrom, H. Ohlsen, M. Bodegard *et al.*, *23rd IEEE Photovoltaic Specialists Conference*, Louisville, 1993, p. 364.
[5] T. Yamaguchi, J. Matsufusa, and A. Yoshida, Jpn. J. Appl. Phys. **31**, Part 2, L703 (1992).
[6] B. M. Basol, V. K. Kapur, A. Halani, and C. Leidholm, Solar Energy Materials and Solar Cells **29**, 163 (1993).
[7] V. V. Kindyak, A. S. Kindyak, V. F. Gremenok *et al.*, Thin Solid Films **250**, 33 (1994).
[8] V. V. Kindyak, A. S. Kindyak, V. F. Gremenyuk *et al.*, Pis'ma Zh. Tekh. Fiz. **21**(7), 60 (1995) [Tech. Phys. Lett. **21**, 268 (1995)].
[9] A. S. Kindyak, V. V. Kindyak, and A. E. Hill, Cryst. Res. Technol. **31S**, 193 (1996).
[10] V. V. Kindyak, A. S. Kindyak, and Ya. I. Latushko, Pis'ma Zh. Tekh. Fiz. **22**(14), 90 (1996) [Tech. Phys. Lett. **22**, 596 (1996)].
[11] J. L. Shay, B. Tell, H. M. Kasper, and L. M. Shiavone, Phys. Rev. B **5**, 5003 (1972).
[12] I. V. Bondar' and I. A. Zabelina, Zh. Prikl. Spektrosk. **60**, 320 (1994).
[13] V. A. Chaldyshev and G. F. Karavaev, Izv. Vyssh. Uchebn. Zaved. Fiz. No. 5, 103 (1963).

Translated by J. R. Anderson

Surface light waves on the boundary of a photorefractive crystal with a diffusion-drift nonlinearity mechanism

V. N. Belyĭ and N. A. Khilo

Division of Optical Problems in Information Sciences, Belarus Academy of Sciences, Minsk

(Submitted January 15, 1997)
Pis'ma Zh. Tekh. Fiz. **23**, 31–36 (June 26, 1997)

All the possible types of surface light wave that can exist on the boundary of a photorefractive uniaxial crystal with a diffusion-drift nonlinearity mechanism are identified. It is shown that by varying the magnitude and direction of an external electric field E_0 one can control both the parameters and the type of the surface wave. In the particular case of zero field E_0 (the diffusion nonlinearity mechanism) the general solution agrees with the solution obtained in Ref. 5.

It has been recently shown that diffractionless light beams or spatial solitons can exist in photorefractive crystals with a nonlocal nonlinear response.[1,2] An investigation of spatial solitons in photorefractive crystals is important both for elucidating the mechanisms of the photorefractive response, and in a practical sense to develop optical information processing systems. Of interest are the case of bulk photorefractive media, and also the effects of spatial boundedness of the crystal on the photorefractive response and the effects of diffractionless propagation of light. The effect of the spatial boundedness of the crystal on the propagation of light is related, as in linear crystal optics, mainly to the possibility of a new type of excitation — surface waves. It should be noted that the solution of Maxwell's equations in the form of surface waves must follow from the general soliton solution by also including the region of divergence of the latter. The real divergence of the amplitude of the light wave is eliminated through the finiteness of the crystal. We shall use this approach in this work, basing it on the previously derived solution[3] for a spatial soliton in an unbounded photorefractive crystal with a diffusion-drift nonlinearity mechanism.

Let us consider the propagation geometry shown in Fig. 1. A uniaxial photorefractive crystal such as strontium barium niobate (SBN) or barium titanate ($BaTiO_3$), is oriented with the optical axis perpendicular to the interface. The optical **c** axis coincides in direction with the spontaneous polarization of the photorefractive ferroelectric, and the x axis of the coordinate system is directed parallel to the **c** vector. A surface light wave propagates along the z axis and is polarized in the xz plane. The solution of Maxwell's equations for the x component of the field amplitude, $a(x,z)$ has the form[3,4]

$$a(x,z)=\exp[ik_0\delta n_s z+P_e x](\operatorname{sech}(P_s x))^D, \tag{1}$$

where

$$P_e=k_0I_{01}/(2k_0I_{11}-1/2k),$$

$$D=(1/2k-k_0I_{11})/(2k_0I_{11}-1/2k),$$

$$P_s=\sqrt{(k_0I_{01})^2+k_0(\delta n_v-\delta n_s)(2k_0I_{11}-1/2k)}/ (1/2k-k_0I_{11}), \tag{2}$$

$$\delta n_v=I_{00},\quad k_0=\omega/c,\quad k=k_0n,$$

n is the refractive index. The parameters I_{mn} are determined by the nonlocal response function of the photorefractive crystal in the following way

$$I_{00}=n^3rE_0/2,\quad I_{01}=I_{00}(E_0/C_p+C_d/E_0),$$

$$I_{11}=-2I_{00}(E_0^2/C_p^2+2C_d/C_p),$$

where r is the effective electrooptical coefficient, $C_p=(q-q')E_p$, $C_d=E_d/(q-q')$, q and q' are the transverse components of the wave vectors of the pair of interacting plane waves, E_d is the diffusion field, E_p is limiting space-charge field, and E_0 is the external electric field. If the field is applied along the positive x axis (see Fig. 1) then $E_0>0$, $I_{00}>0$, and $I_{11}<0$. Therefore by varying the magnitude and direction of the electric field one can control the spatial amplitude distribution (1).

Let us consider systematically the possible cases of existence of surface waves in photorefractive crystals.

1. We assume that $D>0$. This is possible for $E_0<0$ and $k_0I_{11}<1/2k_0I_{11}$, Then Eq. (2) implies that $\delta n_v<0$, $P_e>0$, and therefore in the b geometry (in Fig. 1) a spatially bounded solution will exist regardless of the behavior of the function (1) for $x>0$. In the a geometry (Fig. 1) the condition $P_sD>P_e$ must hold for the existence of a surface wave, from which we find $\delta n_s<0$, $|\delta n_s|>|\delta n_v|$. Since the parameter δn_v has the sense of an electrooptical correction of the refractive index for a plane wave, these inequalities imply that in this particular case the surface wave has a higher phase velocity of propagation than a plane wave in an unbounded crystal.

2. $D<0$, $E_0>0$. In this case $\delta n_v>0$, $P_s<0$, and the spatial distribution of the field has the form

$$a(x,z)=\exp[ik_0\delta n_s z+P_e x](\cosh(P_s x))^{|D|}. \tag{3}$$

Equation (3) implies that a surface wave can exist here in the a geometry. The necessary condition is the inequality $P_s|D|<|P_e|$. We then obtain $\delta n_s<\delta n_v$, and thus the value of δn_s can be positive or negative. If $\delta n_s<\delta n_v-k_0I_{01}^2/(2k_0|I_{11}|+1/2k)$, then the parameter P_s in Eq. (2) becomes imaginary. Then from Eq. (3) we find the distribution of the amplitude of the surface wave field

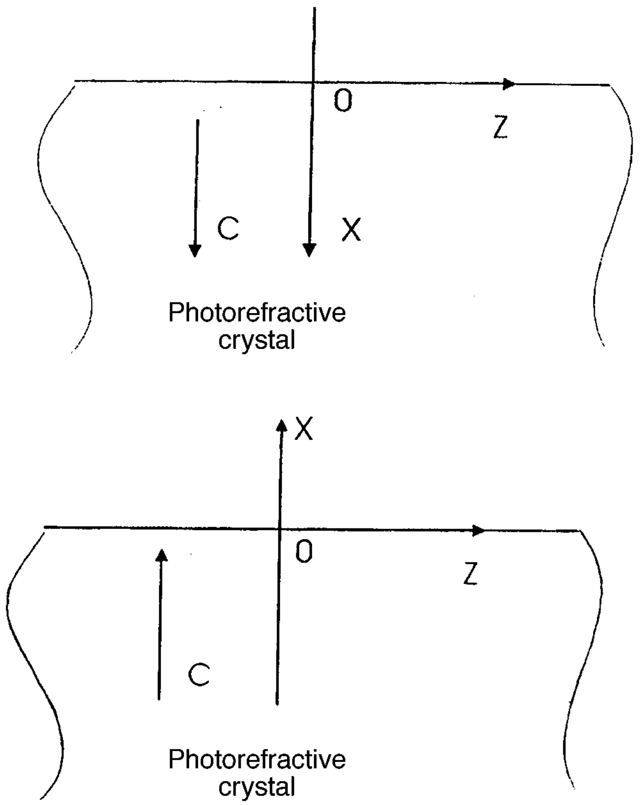

FIG. 1. Orientation of the optical **c** axis relative to the face of the photorefractive crystal: a—the axis is directed from the face into the photorefractive crystal; b—the axis directed is towards the face.

$$a(x,z)=\exp[ik_0\delta n_s z+P_e x](\cos(|P_s|x))^{|D|}. \tag{4}$$

This distribution, unlike that of Eqs. (1) or (3) has damped oscillations, which is characteristic of the field of a surface wave or the evanescent field of linear crystal optics. In the special case $P_s=0$, we obtain exponential damping of the field amplitude in the photorefractive crystal.

3. $D<0$, $E_0<0$, $1/2k<k_0I_{11}$. In this case the field distribution is described by expression (3) in which $P_e>0$. Consequently a surface wave exists in the *a* geometry, while in the *b* geometry it exists if $P_e>P_s|D|$, that is, for $\delta n_s>\delta n_v$. Here the amplitude distribution is given by the expression (3). Then for $\delta n_s>\delta n_v+k_0I_{11}^2/(2k_0I_{11}-1/2k)$ the parameter P_s in Eq. (2) becomes imaginary and the field is described by formula (4). The difference between this regime and case (2) ($D<0$, $E_0>0$) is that the surface wave has a lower velocity of propagation than a plane wave.

4. $D<0$, $E_0<0,1/2k\geqslant k_0I_{11}$. In this case $P_e<0$ and surface waves can exist in the *a* geometry of Fig. 1 for the condition $|P_e|>P_s|D|$. From Eqs. (2) we obtain the condition $\delta n_s<\delta n_v$ for the existence of surface waves of type (3). Then for $\delta n_s<\delta n_v-k_0I_{01}^2/(1/2k-2k_0I_{11})$ a surface wave is of the oscillatory type (Eq. (4)). Let us now determine the structure of the field at the boundary of this region, i.e., for $2k_0I_{11}=1/2k$. In this case $D=\infty$, and the field distribution has the form

$$a(x,z)=\exp[ik_0\delta n_s z+P_e x], \tag{5}$$

where $P_e=(\delta n_s-\delta n_v)/2I_{01}$. Since $\delta n_v<0$ and $I_{01}>0$, the field (5) corresponds to a surface wave for the condition $(\delta n_s+|\delta n_v|)<0$ in the *a* geometry and $(\delta n_s+|\delta n_v|)>0$ in the *b* geometry.

5. Finally, we consider the case where $D=-1$. It is realized in the absence of an external electric field, i.e., for a photorefractive crystal with a diffusion nonlinearity mechanism. Setting $D=-1$ in formulas (1) and (2), we obtain

$$a(x,z)=\exp[k_0(i\delta n_s z-2lI_{01}x)]\cosh[2k(\sqrt{(k_0I_{01})^2+\delta n_s/2n})x]. \tag{6}$$

The existence of a surface wave is possible here in the *a* geometry if $0>(\delta n_s/2n)>-(k_0I_{01})^2$. For $(\delta n_s/2n)<-(k_0I_{01})^2$ the surface wave becomes oscillatory. This special case of the diffusion nonlinearity mechanism has been studied theoretically in Ref. 5 and experimentally in Ref. 6.

Thus photorefractive crystals with a diffusion-drift nonlinearity mechanism can support surface waves of various types. By varying the magnitude and also the direction of the applied electric field one can change both the parameters and the type of surface wave. In addition to studying the surface waves on one interface, it would be of interest to study them in waveguide layers. On the whole, however, along with the spatial solitons, surface waves constitute interesting objects for study, both from the point of view of physics and for the sake of possible practical applications for optical data processing. The importance of studying the properties of nonlinear surface waves is also linked with the solution of other interesting problems, such as bistability in the reflection from the faces of photorefractive crystals.[7]

[1] B. Crosignani, M. Segev, D. Englin, P. Porto, A. Yariv, and G. Salamo, J. Opt. Soc. Amer. B **10**, 446 (1993).

[2] G. S. Duree, J. L. Shultz, Jr., G. J. Salamo, M. Segev, A. Yariv, B. Crosignani, P. Porto, E. J. Sharp, and R. R. Neurgaonkar, Phys. Rev. Lett. **71**, 533 (1993).

[3] V. N. Belyĭ and N. A. Khilo, Pis'ma Zh. Tekh. Fiz. **20**(18), 40 (1994) [Tech. Phys. Lett. **20**, 740 (1994)].

[4] V. N Belyi, N. S. Kazak, V. K. Pavlenko, and N. A. Khilo, Proc. SPIE **2800**, 179 (1996).

[5] G. S. Garcia-Quirino, J. J. Sanchez-Mondragon, and S. Stepanov, Phys. Rev. A **51**, 1571 (1995).

[6] M. Cronin-Golomb, Opt. Lett. **20**, 2075 (1995).

[7] R. Daisy and B. Fisher J. Opt. Soc. Amer. B **11**, 1059 (1994).

Translated by J. R. Anderson

Fullerenes as the imaging element of the tip of an atomic force microscope

G. V. Dedkov

Kabardino–Balkarsk State University, Nal'chik

(Submitted January 29, 1997)
Pis'ma Zh. Tekh. Fiz. **23**, 37–43 (June 26, 1997)

It is proposed that the C_{60} molecule be used as the imaging element of the tip of an atomic force microscope. Test computer images are obtained of portions of a distorted graphite surface and a graphite surface with vacancies. [S1063-7850(97)02306-9]

Atomic force microscopy is a highly sensitivity method of measuring ultrasmall forces between the tip of the atomic force microscope and the sample surface, for studying the atomic topography of objects, for studying adhesion, friction, electrical, and magnetic properties, etc.[1–4] At the present time, however, there is no reliable theoretical model to allow one to make adequate quantitative calculations of the topography of the force interactions between the tip of the atomic force microscope and the sample, and accordingly interpret the experimentally obtained images of the surface. Known theoretical schemes advanced in Ref. 5, by which one can model the operation of the atomic force microscope in the contact mode, use a greatly simplified model of the tip, formed of one or several atoms.[5–7] Despite the qualitative advances in obtaining theoretical images of some model objects, the theory is still far from perfected, since the images that are obtained depend strongly on the model of the tip and the approximations used for the interatomc forces (usually this potential is of the Lennard–Jones or the Morse type, whose applicability in the range of interatomic distances $R<0.5$ nm is doubtful). This results in such artifacts as "dipping of the tip below the surface" and unstable scanning the tip along a line of constant force.[7] For these and other reasons it has not yet been found possible to find a reliable connection between the experimental forces (determined from the well-known piezoelectric moduli of the cantilever of the atomic force microscope) and the vertical and horizontal coordinates of the tip, or to calculate the forces theoretically. One must regard as paradoxical even the fact that atomic resolution can be obtained with tips whose radius of curvature is 20 nm and more,[8,9] i.e., much greater than atomic distances. Computer simulation of images of a surface with tips of this kind do not, of course, reveal any kind of atomic structure. This result compels us to hypothesize that the surface of the tip contains small-scale uncontrolled microscopic roughness (protuberances), one of which is the "imaging" element. Such protuberances may be made by, for example, adsorbed microparticles of water or other material. This would explain the experimentally observed disappearance of atomic resolution under high vacuum, or, conversely, the high resolution obtained when the atomic force microscope is operated in air (using exactly the same tip).

In this article we propose that the C_{60} fullerene molecule be used as the imaging element on the tip of an atomic force microscope; this molecule has a well-defined structure, a

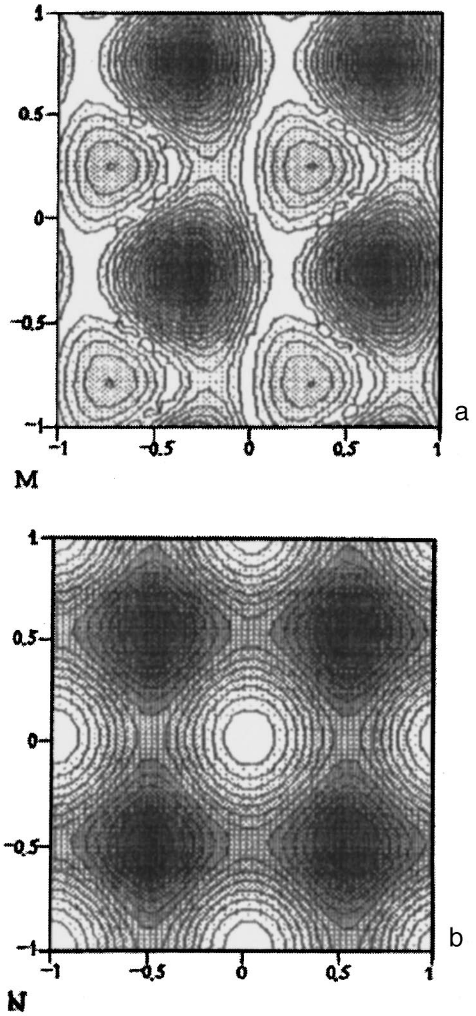

FIG. 1. Theoretical contour image of a nominal square lattice of carbon atoms (the lattice period is $d=0.246$ nm, the size of the frame is 4.8×4.8 Å, the dark background corresponds to the interstitial sites: a — image obtained with C_{60} ($f_0=7.07$ nN; the maximum variation in height from light to dark is 0.008 nm); b — the "one imaging atom" approximation ($f_0=2.7$ nN, height variation is 0.034 nm).

TABLE I. C_{60}–C_{60} interaction parameters.

Our work	Equilibrium spacing, nm	Binding energy, eV
Ref. 13	0.96	0.34
	1.006	0.32

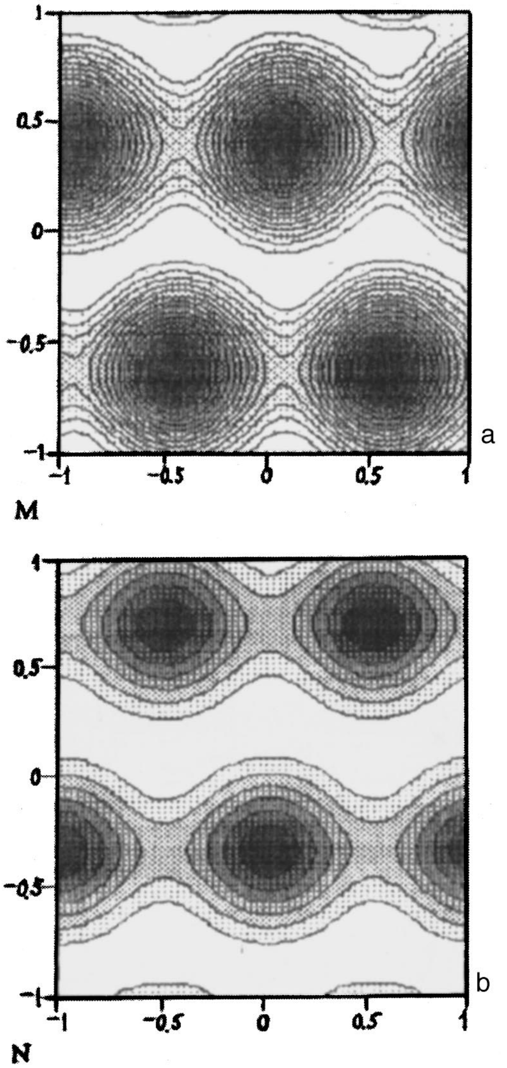

FIG. 2. The same as in Fig. 1 for the (0001) graphite surface. a — $f_0=12.6$ nN, height variation 0.005 nm; b — $f_0=3.82$ nN, height variation 0.013 nm.

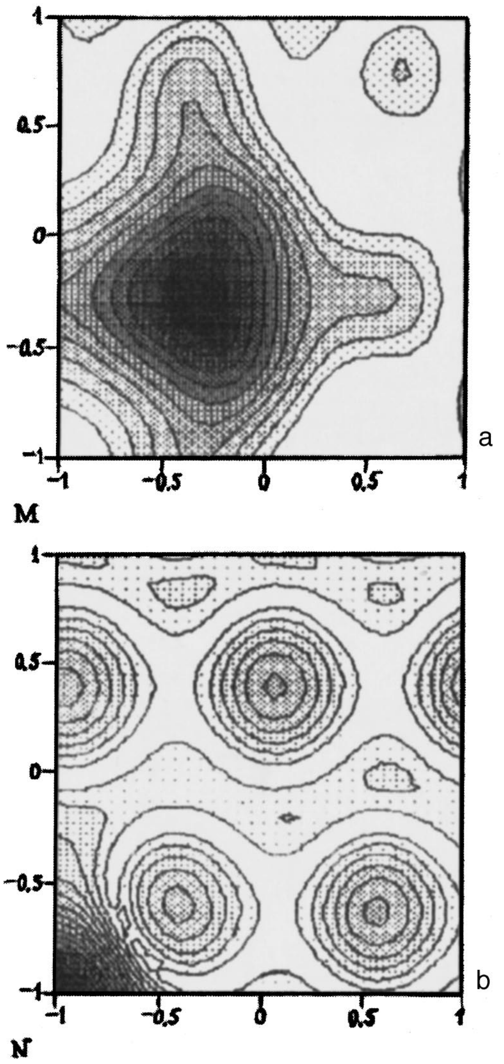

FIG. 3. Image of a square lattice and a graphite lattice with vacancies. In both cases the imaging element of the atomic force microscope is a C_{60} molecule: a — $f_0=13.5$ nN, b — $f_0=9.59$ nN, height variation 0.005 nm.

small diameter (0.7 nm), and extremely high mechanical stability.[10] I believe that all of these properties together make fullerene a unique imaging element for the atomic force microscope. Present-day technology for preparing fullerenes and fullerene coatings is highly advanced. The C_{60} molecule can be fastened to the tip of the cantilever of an atomic force microscope by mechanical pressing or by electrochemical deposition.

In order to clarify the theoretical side of this question, computer simulations were carried out for several model surfaces, with C_{60} used as the imaging element on the tip of the atomic force microscope. The forces of interation between the carbon atoms of the C_{60} molecule and the surface were calculated in the approximation of an electron gas.[11,12] The individual components of the force were obtained by direct differentiation of the integral expressions for the corresponding components of the interaction potentials, and then by numerical integration over the volume, as is done in the calculation of the pair potentials. To monitor the accuracy of this method we first calculated the potential of the pair interaction between C_{60} molecules. We used additive summation of the interactions between the carbon atoms belonging to different molecules. The results of the calculations of the binding energy and the equilibrium distance, obtained after averaging over the orientation of the molecules, were found in very good agreement with the experimental data.[13] The corresponding data are listed in Table I.

Figures 1, 2a, and 3a and b show the results of computer simulations of the lines of constant force $h(x,y)=f_0$ corresponding to the position of the tip of an atomic force microscope, where x and y are the Cartesian coordinates of its atom closest to the surface (in the plane of the surface), h is its distance from the surface, and f_0 is the level of the force in units of 10^{-9} N.

In the calculations it was assumed that the C_{60} molecule is oriented so that the carbon atom closest to the surface is situated in the closest to the surface point of its spherical framework. The size of the frame is 4.8×4.8 Å. The number of model points in a single frame is 961. Figures 1a and 2a correspond to the images of a nominal square lattice of carbon atoms (with the side of a square equal to $d = 0.246$ nm) and the unreconstructed (0001) graphite plane (with the same period of the orthorhombic lattice). The calculations assumed an interaction only with the outermost atom of the plane of the graphite structure, and therefore the images lack the contrast in the brightness of neighboring atoms of the hexagons such as was observed in Ref. 6. Figures 3a and b show images of the same surface when there is a vacancy at one of the sites. Figures 1b and 2b were obtained with the assumption of a single imaging atom, and are shown for comparison. The results show that an atomic force microscope tip formed by a fullerene molecule can provide high contrast. A comparison of the numerical values of the forces corresponding to the same coordinate h gives grounds to assume that the ''single imaging atom'' approximation underestimates by a factor of 3–4 the results obtained without taking into account all the C_{60} atoms. This result supports the conclusion that a quantitative prediction of the force of interaction in an atomic force microscope is not possible without allowing for the real atomic configuration of the apex of the atomic force microscope tip. In the model examined in this work this is automatically provided by the well-defined structure of the C_{60} molecule.

In conclusion, it should be noted that fullerenes other than C_{60} can be used for the same purpose: metal carbones with heavy atoms within, such as $U@C_{60}$, this may enhance the contrast of the image. Good geometrical parameters and strength are also attributes of single nanotubes (empty or with a filler) as well as graphite fibers.

[1] G. Binnig, C. F. Quate, and Ch. Gerber, Phys. Rev. Lett. **12**, 930 (1986).
[2] D. Sarid, *Scanning Force Microscopy with Applications to Electric, Magnetic and Atomic Forces* (Oxford University Press, New York, 1991).
[3] F. Ohnesorge and G. Binnig, Science **260**, 1451 (1993).
[4] G. Meyer and N. M. Amer, Appl. Phys. Lett. **57**, 2089 (1990).
[5] B. Brushan, J. N. Israelachvili, and U. Landman, Monthly Nature. **3**(4), 63 (1995).
[6] S. A. Gould, K. Burke, and P. K. Hansma, Phys. Rev. B **40**, 5363 (1989).
[7] E. V. Blagov, G. L. Klimchitskaya, A. A. Lobashev, and V. P. Mostepanenko, Pis'ma Zh. Tekh. Fiz. **21**(3), 73 (1995) [Tech. Phys. Lett. **21**, 121 (1995)].
[8] Park Scientific Instruments, Sunnyvale, CA.
[9] J. P. Clevelend, M. Radmacher, and P. K. Hansma, in *Forces in Scanning Probe Methods*, edited by H. J. Gunterodt *et al.* (Kluwer Academic Publishers, Netherlands, 1995).
[10] A. V. Eletskiĭ and V. M. Smirnov, Usp. Fiz. Nauk **165**, 978 (1995).
[11] R. G. Gordon and Y. S. Kim, J. Chem. Phys. **56**, 3122 (1972).
[12] G. V. Dedkov, Usp. Fiz. Nauk **165**, 919 (1995).
[13] L. A. Girifalco, J. Phys. Chem. **96**, 858 (1992).

Translated by J. R. Anderson

Analytic model for the lowering of the ionization potentials of atoms and ions in a collisional plasma

S. I. Anisimov and Yu. V. Petrov

L. D. Landau Institute of Theoretical Physics, Russian Academy of Sciences, Moscow District, Chernogolovka

(Submitted February 10, 1997)
Pis'ma Zh. Tekh. Fiz. **23**, 44–49 (June 26, 1997)

A model admitting of an analytic solution is developed for the calculation of the level shift and the reduction of the ionization potentials of atoms and ions due to screening in a collisional plasma. The application of the derived equations to the plasmas of aluminum, gold, copper and cesium shows the greatest reduction in the ionization potential occurs for cesium. © *1997 American Institute of Physics.* [S1063-7850(97)02406-3]

The ionization potentials of the neutral atoms and the ions are of great importance in determining the densities of the components of a collisional plasma.[3,4,6–14] In a dense plasma these potentials are to a great extent renormalized compared to the free atoms and ions because of screening of the Coulomb interaction. We shall describe the potential energy of a valence electron of an atom or ion at a distance r from the nucleus by the function

$$U(r)=-\frac{Z^*/\lambda}{\exp(r/\lambda)-1} \tag{1}$$

(the Hulthén potential with a screening length λ and an effective charge Z^*). For $r\ll\lambda$ this function goes over to the Coulomb potential $U_c(r)=-Z^*/r$, and for $r\gg\lambda$ it takes the form $U(r)=-(Z'/\lambda)\,e^{-r/\lambda}$. Transforming to the variable $x=r/\lambda$ and writing the Schrödinger equation for the function $\chi(x)=R(x)/x$, where $R(x)$ is the radial part of the wave function, we obtain (in atomic units)

$$-\frac{\chi''}{2\lambda^2}+\left(-\frac{Z^*}{\lambda}\cdot\frac{1}{e^x-1}+\frac{l(l+1)}{2\lambda^2x^2}\right)\chi=E\chi. \tag{2}$$

The discrete spectrum of this equation is known[2,5] for the states with an orbital angular momentum $l=0$. It is determined by the principal quantum number $n(n=1,2,\dots)$:

$$E_n=-\frac{Z^{*2}}{2n^2}\left(1-\frac{n^2}{2Z^2\lambda}\right)^2. \tag{3}$$

For the states with nonzero orbital angular momentum l we proceed in the following way. We replace in Eq. (2) the centrifugal term $U_l(x)=l(l+1)/2\lambda^2x^2$ by the function $\widetilde{U}_l(x)=l(l+1)/2\lambda^2/(e^x-1)^2$. For $r\ll\lambda$ the functions $U_l(x)$ and $\widetilde{U}_l(x)$ coincide, and since $r\sim1$ for a free electron, for $\lambda\gg1$ in a plasma $\widetilde{U}_l(x)$ is a very good approximation to the function $U_l(x)$. With the centrifugal function $\widetilde{U}_l(x)$ we can solve the radial equation exactly for arbitrary l. Moreover, we can improve the result by taking into account the difference between $U_l(x)$ and $\widetilde{U}_l(x)$ by perturbation theory. The equation for the function χ now is

$$-\frac{\chi''}{2\lambda^2}+\left(-\frac{Z^*}{\lambda}\cdot\frac{1}{e^x-1}+\frac{l(l+1)}{2\lambda^2}\cdot\frac{1}{(e^x-1)^2}\right)\chi=\widetilde{E}\chi. \tag{4}$$

Going over to the variable $u=e^{-x}$ and introducing the notation

$$\alpha^2=-\lambda^2\widetilde{E},\quad \beta^2=2Z^*\lambda, \tag{5}$$

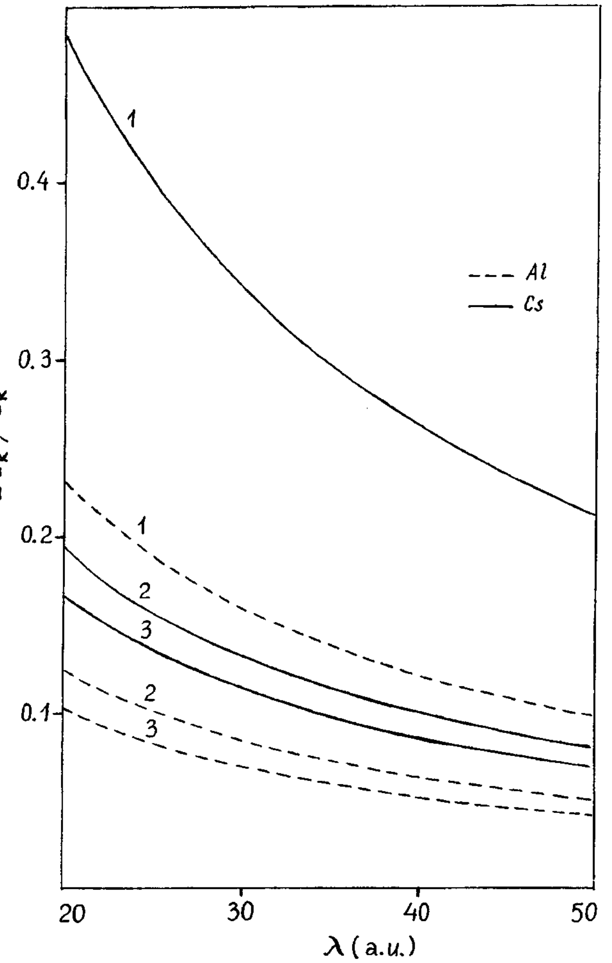

FIG. 1. Relative lowering of the three first ionization potentials ΔI_k ($k=1,2,3$) for aluminum and cesium. Here $\Delta I_k/I_k=(I_k(\lambda)-I_k(\infty))/I_k(\infty)$.

we can write χ as

$$\chi(u)=u^{\alpha}(1-u)^{l+1}w(u), \tag{6}$$

where the function $w(u)$ satisfies the equation

$$u(1-u)w''+(2\alpha+1-(2\alpha+2l+3)u)w'-((2\alpha+1)\times(l+1)-\beta^2)w=0. \tag{7}$$

The final solution for $u\to 1$ has the form

$$w(u)=F(\alpha+1+l+\gamma,-n_r,\,2\alpha+1,u), \tag{8}$$

where $\gamma=(\alpha^2+\beta^2+l(l+1))^{1/2}$, $n_r=-(\alpha+1+l+\gamma)$ is the radial quantum number ($n_r=0,1,2,\ldots$), and $F(\xi,\eta,\zeta,u)$ is the hypergeometric function

$$F(\xi,\eta,\zeta,u)=\sum_{m=0}^{\infty}\frac{(\xi)_m(\eta)_m}{(\zeta)_m}\cdot\frac{u^m}{m!}.$$

Here we have introduced the notation

$$(\xi)_m=\xi(\xi+1)(\xi+m-1),$$

$$(\xi)_0=1.$$

Introducing the principal quantum number $n=n_r+l+1$ ($n=1,2,\ldots$), we obtain the discrete spectrum in the form

$$\widetilde{E}_{n,l}=-\frac{Z^{*2}}{2n^2}\left(1-\frac{n^2-l(l+1)}{2Z^*\lambda}\right)^2. \tag{9}$$

Using the perturbation

$$\delta U_l(x)=U_l(x)-\widetilde{U}_l(x), \tag{10}$$

we obtain the correction to $\widetilde{E}_{n,l}$:

$$\delta\widetilde{E}_{n,l}=\frac{l(l+1)}{2\lambda^2}\,\frac{\int_0^{\infty}\chi_{n,l}^2\left(\frac{1}{x^2}-\frac{1}{(e^x-1)^2}\right)dx}{\int_0^{\infty}\chi_{n,l}^2dx}. \tag{11}$$

For the cases corresponding to the so-called circular Coulomb orbitals ($n_r=0,\ l=n-1$), this correction is

$$\begin{aligned}\delta\widetilde{E}_{n,l}&=\delta\widetilde{E}_{n,n-1}\\&=\frac{l(l+1)}{2\lambda^2}\,\frac{\sum_{m=0}^{2n}(-1)^m\binom{2n}{m}(2\alpha+m)\ln(2\alpha+m)-\sum_{m=0}^{2(n-1)}\frac{(-1)^m}{2\alpha+2+m}\binom{2n-2}{m}}{\sum_{m=0}^{2n}\frac{(-1)^m}{2\alpha+m}\binom{2n}{m}}.\end{aligned} \tag{12}$$

Here

$$\binom{i}{j}=\frac{i!}{j!(i-j)!}$$

are the binomial coefficients.

All the sums in expression (12) are finite and of low order and therefore can be easily calculated. The expression is also valid for small λ, and hence it is possible to determine the point of the Mott transition, i. e., the value of λ for which $E_{n,l}=0$. Far from the region of the Mott transition, where $\lambda \gg 1$, by calculating the asymptote of expression (11), we obtain for arbitrary l:

$$\delta\widetilde{E}_{n,l}=\frac{\alpha l}{2\lambda^2}. \tag{13}$$

The effective charge Z^* will be determined from the equality of the ionization potential of the free atom or ion ($\lambda\to\infty$) with the experimental value I_{nl}^0

$$\frac{Z^{*2}}{2n^2}=I_{nl}^0. \tag{14}$$

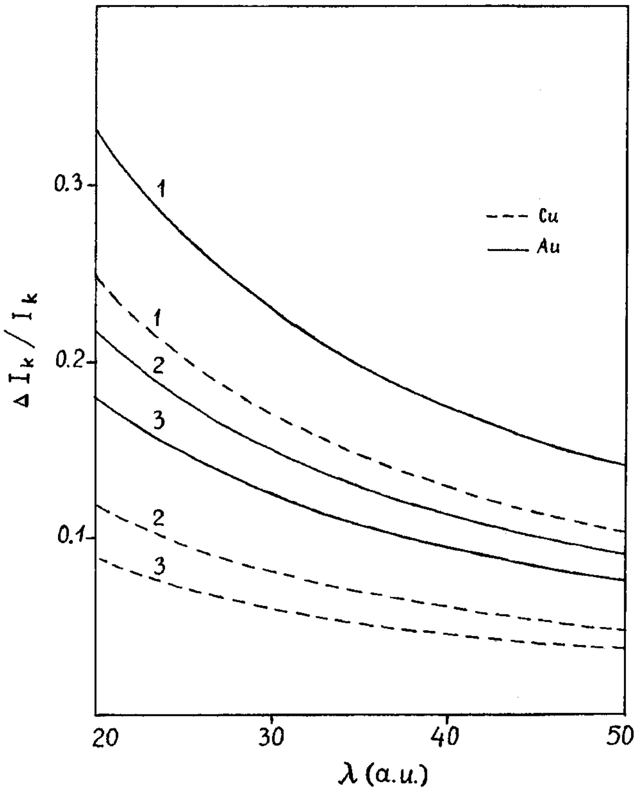

FIG. 2. Relative lowering of the first three ionization potential for copper and gold.

Then the ionization potential taking into account the screening for large λ is

$$I_{nl}=-E_{nl}=I_{nl}^{0}\left(1-\frac{n^{2}-l(l+1)}{2n\lambda}\sqrt{\frac{1}{2I_{nl}^{0}}}\right)^{2}\left(1-\frac{l}{\lambda}\sqrt{\frac{1}{I_{nl}^{0}}}\right). \tag{15}$$

The relative lowering of the first three ionization potentials of aluminum and cesium as functions of the screening length is shown in Fig. 1. Similar curves for the first three ionization potentials for gold and copper are shown in Fig. 2. One should notice that the ionization potential of cesium is lowered to a considerably greater degree than those of the other elements.

This work was supported by the Russian Fund for Fundamental Research, Grant No. 95-02-04535a and the Grant INTAS-94-1105.

[1] L. D. Landau and E. M. Lifshitz, *Statistical Physics*, 2 vols, 3rd ed., (Pergamon Press, Oxford 1980) [Russ. transl., Nauka, Moscow 1976, 1978].

[2] S. Flügge, *Practical Quantum Mechanics*, transl. from the German (Springer-Verlag, Berlin, 1971) [Russ. transl., Mir, Moscow, 1974].

[3] H. Renkert, F. Hensel, and E. U. Frank, Phys. Lett. A. **30**, 494 (1969).

[4] W. Hefner and F. Hensel, Phys. Rev. Lett. **48** 1026 (1982).

[5] N. R. Arista, A. Gras-Marti, and R. A. Baragiola, Phys. Rev. A **40**, 6873 (1989).

[6] A. Förster, T. Kahlbaum, and W. Ebeling, High Press. Res. **7**, 375 (1991).

[7] W. Ebeling, A. Förster, and V. Fortov *et al.*, *Thermophysical Properties of Hot Dense Plasmas*, Teubner-Texte zur Physik, Bd. 25, (Stuttgart–Leipzig, 1991).

[8] A. A. Likal'ter, Usp. Fiz. Nauk **162**(7), 119 (1992) [Sov. Phys. Usp. **34**, 591 (1992)].

[9] I. T. Yakubov, Usp. Fiz. Nauk **163**(5), 35 (1993) [Phys. Usp. **36**, 365 (1993)].

[10] A. A. Likal'ter, Zh. Éksp. Teor. Fiz. **106**, 1663 (1994) [JETP **79**, 899 (1994)].

[11] A. A. Likal'ter, Teplofiz. Vys. Temp. **32**, 803 (1994).

[12] A. W. DeSilva and H.-J. Kunze, Phys. Rev. E. **49**, 4448 (1994).

[13] A. Ng, P. Celliers, G. Xu *et al.*, Phys. Rev. E. **52**, 4299 (1995).

[14] A. A. Likal'ter, Zh. Éksp. Teor. Fiz. **107**, 1996 (1995) [JETP **80**, 1105 (1995)].

Translated by J. R. Anderson

Silicon metal-dielectric-semiconductor varicaps with an yttrium oxide dielectric

V. A. Rozhkov and A. Yu. Trusova

Samara State University

(Submitted October 10, 1996)
Pis'ma Zh. Tekh. Fiz. **23**, 50–55 (June 26, 1997)

This paper reports an investigation of the electrophysical properties of metal-dielectric-semiconductor varicaps with an yttrium oxide dielectric, prepared by resistive vacuum evaporation of the rare-earth metal with subsequent thermal oxidation of the film in air at 500–550 °C. It is found that the electrical conductivity of the samples follows the Poole-Frenkel law. High-frequency capacitance-voltage characteristics are used to determine the specific capacitance of the dielectric, $C_0 = 0.027$–$0.03\ \mu\mathrm{F/cm^2}$, the slope of the capacitance-voltage characteristic, $dC/dV = 35$–40 pF/V, the fixed charge in the dielectric, $Q_f = (1.7$–$2.7)\times 10^{-8}\ \mathrm{C/cm^2}$, and the density of surface states at the flat-band potential, $N_{ss} = (1$–$2)\times 10^{11}\ \mathrm{cm^{-2}\cdot eV^{-1}}$. The capacitance tuning range factor for the metal-dielectric-semiconductor varicaps is 2.5–3. These structures are shown to be applicable as metal-dielectric-semiconductor varicaps with a low control voltage and a high quality factor. © *1997 American Institute of Physics.* [S1063-7850(97)02506-8]

In this paper we report the investigation of the electrophysical properties of silicon metal-dielectric-semiconductor varicaps with an yttrium oxide dielectric prepared by resistive vacuum evaporation of the rare-earth metal and subsequent thermal oxidation of the film in air at 500–550 °C.

It is found that the electrical conductivity of the samples follows the Poole-Frenkel law. High-frequency capacitance-voltage characteristics were used to determine the specific capacitance of the dielectric, $C_0 = 0.027$–$0.03\ \mu\mathrm{F/cm^2}$, the slope of the capacitance-voltage characteristic, $1/C\ dC/dV = 0.4$–$0.44\ \mathrm{V^{-1}}$, the fixed charge in the dielectric $Q_f = (1.7$–$2.7)\times 10^{-8}\ \mathrm{C/cm^2}$, and the density of surface states at the flat-band potential, $N_{ss} = (1$–$2)\times 10^{11}\mathrm{cm^{-2}\cdot eV^{-1}}$. The capacitance tuning range factor in the metal-dielectric-semiconductor varicaps was 2.5–3.

These structures have been found to be applicable as metal-dielectric-semiconductor varicaps and photovaricaps.

Nonlinear metal-dielectric-semiconductor capacitors (varicaps), which are widely used in radio engineering and optoelectronic devices, have a high quality factor, a wide capacitance tuning range, and a high input impedance. To obtain a wide capacitance tuning range and a high slope of the capacitance-voltage characteristic it is necessary to use in the device dielectric materials with a high permittivity, such

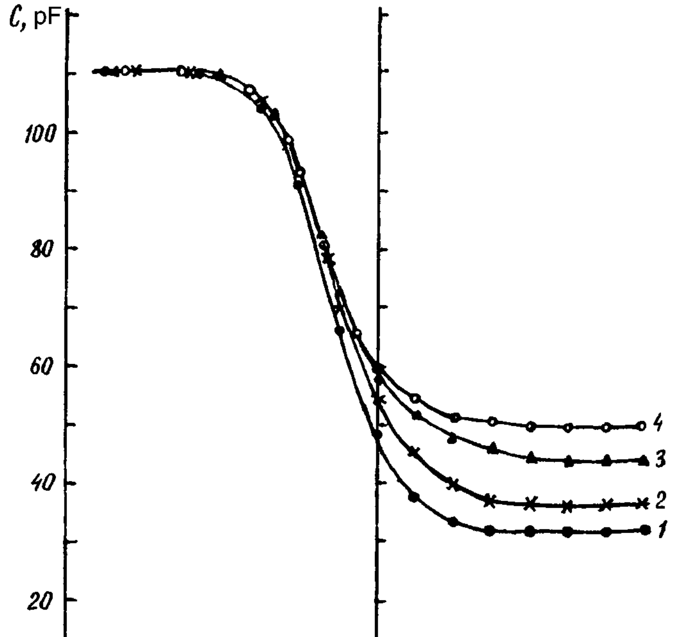

FIG. 1. Capacitance-voltage characteristics of Al-Yb_2O_3-Si metal-dielectric-semiconductor structures with *p*-type silicon in the dark (*1*) and for various levels of illumination: *2* — 450 lux, *3* — 2400 lux, *4* — 6500 lux; $d = 0.3\ \mu$m.

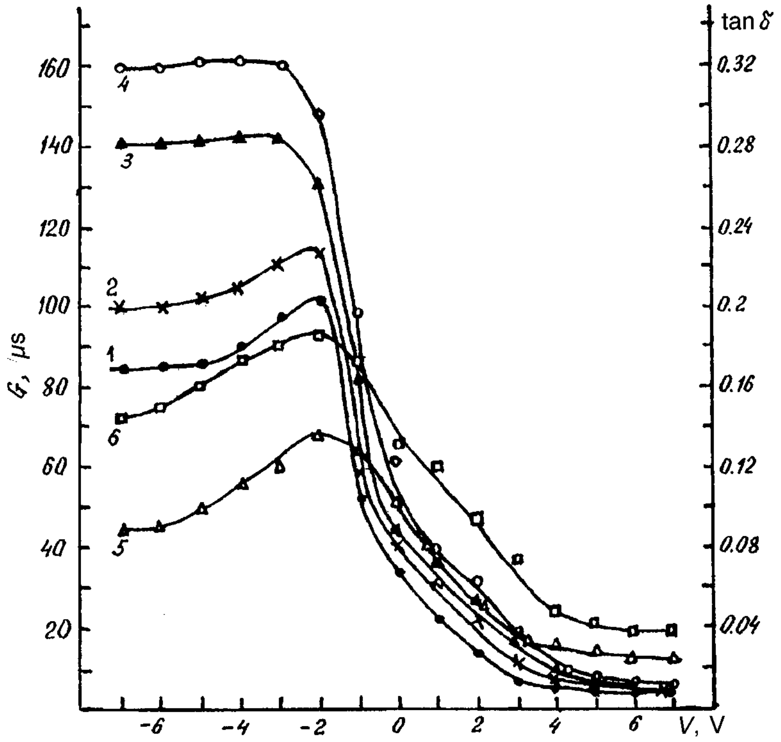

FIG. 2. Conductance G (*1–4*) and tanδ (*5,6*) versus the voltage in the dark (*1, 5*) and for various levels of illumination: 450 lux (*2*); 2400 lux (*3*) and 6500 lux (*4, 6*).

as are possessed by oxides of the rare-earth elements.[1–3] The diverse electrophysical properties of these materials in conjunction with their utility as functional devices make the rare-earth oxides effective light-transmitting coatings for silicon photoelectric devices,[4] electrical switches, memory devices,[5] metal-dielectric-semiconductor varicaps and photovaricaps.[6,7]

We have investigated the electrophysical properties of silicon metal-dielectric-semiconductor structures with dielectric films of yttrium oxide and their potential for use as varicaps and photovaricaps.

The samples used in the experiments were prepared on (111) oriented KÉB-4,5 and (100) oriented KDB-5 single-crystal silicon substrates. The silicon wafers were cleaned ultrasonically in acetone and treated in a dilute solution of hydrofluoric acid to remove the layer of native oxide. The yttrium oxide layers were prepared by deposition of the rare-earth element on the silicon substrate and thermal oxidation of this layer in air at 500–550 °C for 30 min. The yttrium film was deposited on the silicon surface by thermal resistive evaporation from a molybdenum boat in a vacuum of 10^{-5} Torr in a VUP-5 apparatus. Electrodes with an area of 0.39 mm^2 were deposited on the yttrium oxide layer by vacuum evaporation of aluminum through a mask. A continuous aluminum contact was deposited on the polished reverse side of the silicon substrate.

The thickness of the rare-earth oxide in the Al-Yb$_2$O$_3$-Si metal-dielectric-semiconductor structure was 0.3 μm.

The capacitance-voltage characteristics, the conductance G, and the loss tangent tanδ were measured as functions of the applied voltage at a frequency of 1 MHz by means of a digital E7-12 *LCR* meter. The samples were illuminated by the light from a 150 W incandescent lamp with a tungsten filament. The dc current-voltage characteristics were measured by means of an ÉD-05-M electrometer.

In Fig. 1 we show typical capacitance-voltage characteristic of the metal-dielectric-semiconductor in the dark and for various levels of illumination. These curves have the typical high-frequency shape and show no hysteresis. The control voltages corresponding to the variation of the capacitance of the metal-dielectric-semiconductor system lies in the range from -3 to $+2$ V. The experimental current-voltage characteristics have a small shift towards negative voltages relative to the theoretical C–V characteristic of ideal metal-dielectric-semiconductor structures. This indicates the presence of a small positive fixed charge in the dielectric

The capacitance tuning range factor $K = C_{\max}/C_{\min}$ in the dark for variation of the applied voltage was from 2.5 to 3 for various samples. The parameters of these metal-dielectric-semiconductor systems as determined from the capacitance-voltage characteristics have the following values: specific capacitance of the dielectric $C = 0.027$–0.03 μF/cm^2, fixed charge in the dielectric, $Q_f =$ (1.7–2.7) $\times 10^{-8}$ C/cm^2, surface state density at the flat-band potential $N_{ss} = (1\text{–}2)\times 10^{11}$ cm$^{-2}\cdot$ eV^{-1}, and a slope of the capacitance-voltage characteristic at the flat-band potential $1/C\ dC/dV = 0.4$–0.44 V^{-1}. Illumination of the samples increased the capacitance by a factor of 1.5 in the range of voltages corresponding to inversion of the semiconductor surface. This result is mainly due to the photo-induced generation of minority carriers in the surface region of the silicon.

The loss tangent tanδ and the conductance G as functions of the voltage at a measuring signal frequency of 1 MHz in the dark and for various illumination levels are shown in Fig. 2. Characteristic features of these curves are a maximum at the flat-band voltage and a tendency to saturation of $\tan\delta$ and G in the range of voltages corresponding to the accumulation and inversion surfaces of the semiconductor. The value of $\tan\delta$ in the dark for various voltages lay in the range from 0.03 to 0.18, and did not vary appreciably with the illumination level. The resistive component of the conductance on the metal-dielectric-semiconductor structure also depended on the illumination.

The current-voltage characteristics plotted in the coordinates $\log I$ versus $V^{1/2}$ are straight lines and follow the Poole-Frenkel law. The rectification coefficient was between 1.1 and 1.5. The resistivity of the yttrium oxide films, calculated from the current-voltage characteristics was 10^{14}–$10^{15}\ \Omega\cdot\text{cm}$.

In summary, the results obtained in this investigation indicate that these structures show promise for application as stable metal-dielectric-semiconductor varicaps and photovaricaps.

[1] O. S. Vdovin, Z. I. Kir'yashkina, V. N. Kotelkov, V. V. Novichkov, and V. A. Rozhkov, in *Rare-Earth Oxide Films in MIM and MIS Structures* [in Russian] (Saratov State University, Saratov, 1983).

[2] N. V. Latukhina, V. A. Rozhkov, and N. N. Romanenko, Mikroelektronika **23**, 59 (1994).

[3] V. A. Rozhkov, V. P. Goncharov, and A. Yu. Trusova, *IEEE Fifth International Conference on Conduction and Breakdown in Solid Dielectrics* (Leicester, England, 1995), pp. 552–555.

[4] Yu. A. Anoshin, A. I. Petrov, V. A. Rozhkov *et al.*, Pis'ma Zh. Tekh. Fiz. **18**(10), 54 (1992) [Sov. Tech. Phys. Lett. **18**, 321 (1992)].

[5] V. A. Rozhkov and A. I. Petrov, Pis'ma Zh. Tekh. Fiz. **11**, 49 (1985) [Sov. Tech. Phys. Lett. **11**, 21 (1985)].

[6] V. A. Rozhkov, A. Yu. Trusova, I. G. Berezhnoĭ *et al.*, Zh. Tekh. Fiz. **65**(8), 183 (1995) [Tech. Phys. **40**, 849 (1995)].

[7] V. A. Rozhkov, V. P. Goncharov, and A. Yu. Trusova, Pis'ma Zh. Tekh. Fiz. **21**(2), 6 (1995) [Tech. Phys. Lett. **21**, 46 (1995)].

Translated by J. R. Anderson

Superheating of $YBa_2Cu_3O_{7-x}$ thin-film microbridges

O. V. Matyunina and A. V. Pogrebnyakov

Belarus State University of Information Sciences and Radio Electronics

(Submitted July 25, 1996)
Pis'ma Zh. Tekh. Fiz. **23**, 56–62 (June 26, 1997)

It is found that the hysteresis that develops with decreasing temperature in the current-voltage characteristics of thin-film $YBa_2Cu_3O_{7-x}$ microbridges is due to superheating of the bridges by the transport current. The heat transport coefficient is determined to be $\alpha = 5500$–7500 V/(cm$^2\cdot$K) and the thermal resistance of the $YBa_2Cu_3O_{7-x}$/MgO film-substrate interface is $R_{if} = (1.3$–$1.8)\times 10^{-4}$ (cm$^2\cdot$K)/W.
[S1063-7850(97)02606-2]

The efficacy of heat transfer can have a critical effect on the characteristics of electronic devices. In addition to the bulk heat conduction of the materials, a decisive factor can be the thermal resistance of the film-substrate interface, R_{if}, which characterizes the transport of heat into the substrate. At low temperatures ($\leqslant 30$–40 K) R_{if} is well described by the model of mismatched acoustic impedances.[1] However, investigations carried out by various means (such as creation of a transient diffraction grating by means of optical interference, studies of transient absorption during pulsed irradiation, bolometric measurements, etc. (see, e.g., Refs. 2–4)) have shown that the thermal resistance of the interface between a thin film of $YBa_2Cu_3O_x$ and various substrates at temperatures between 80 and 100 K is considerably higher than predicted by the model of Ref. 1, and lies in the range 1×10^{-4}–1.3×10^{-3} (cm$^2\cdot$K)/W.

The non-steady-state heat transfer during measurements of the current–voltage characteristics of thin-film microbridges can cause hysteresis, and also be a reason for a decrease in the critical current, an increase in the noise temperature , and a decrease in the height of the current steps due to microwave irradiation.[5] The hysteresis in the current-voltage characteristics of superconducting weak links formed from low-temperature superconductors, specifically microbridges, has been studied on a number of occasions. The calculations and experiments with tin microbridges carried out by Skocpol and coworkers[6] have shown that because of the limited rate of dissipation of thermal energy a normal region can be formed in the microbridges (a "hot spot"), whose temperature is $T > T_c$. With reduced measurement temperature the minimum current $I_{\min}$ required to maintain the hot spot becomes lower than the critical current I_c and then hysteresis appears on the current-voltage characteristics. As shown in Ref. 6, the current $I_{\min}$ depends on the measurement temperature, the dimensions and the resistivity of the material of the microbridge, and also on the heat transfer coefficient from the microbridge into the substrate.

In this investigation we have studied the characteristics of thin-film $YBa_2Cu_3O_{7-x}$ microbridges. We show that the hysteresis that appears on the current-voltage characteristics of the microbridges with decreasing temperature is due to overheating.

Epitaxial $YBa_2Cu_3O_{7-x}$ films 5000 Å thick were grown on (100) substrates of MgO by a laser method. Films were also used that were grown by ion-beam sputtering of a stoichiometric target. The results of the investigations of the films by Rutherford backscattering in the channeling regime showed that the c axis of the films was oriented perpendicular to the substrate. The critical temperature T_c of the film was 86–91 K (at the middle of the resistive superconducting

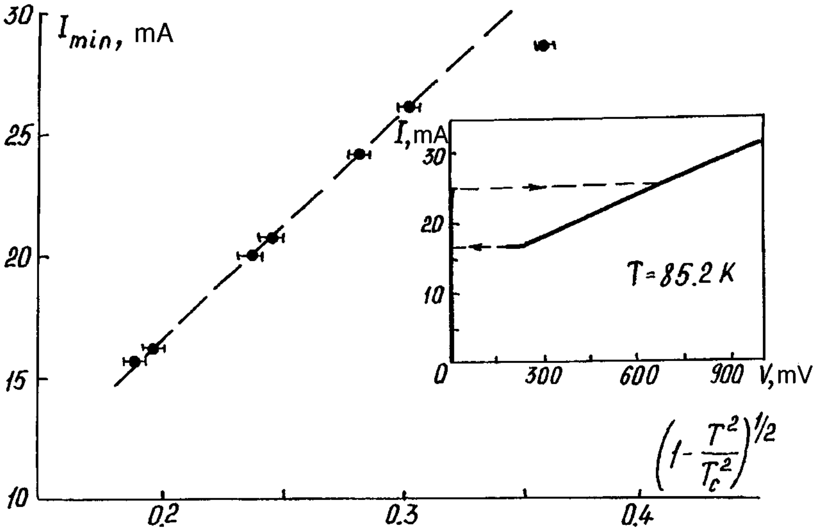

FIG. 1. Reduced-temperature dependence of the current $I_{\min}$ at which the current-voltage characteristic returns to $V=0$ with decreasing sweep current. The points represent the experimental data, the dashed line corresponds to the formula (1) in the text. The inset shows the hysteresis of the current-voltage characteristic recorded at 85.2 K.

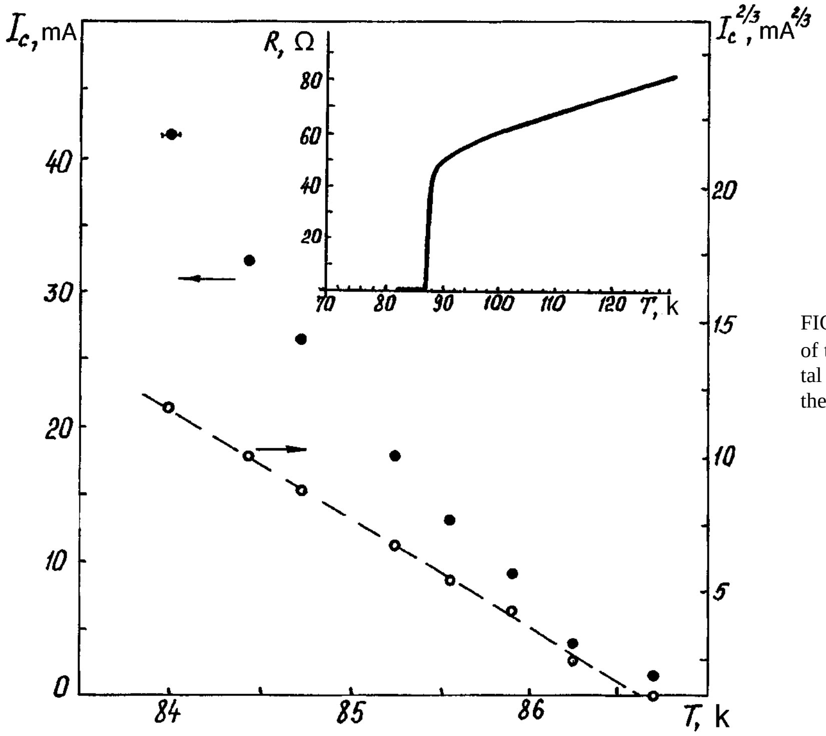

Рис. 2. Зависимости критического тока I_c микромостика и $I^{2/3}$ от температуры

FIG. 2. Temperature dependence of the critical current I_c of the microbridge and $I_c^{2/3}$ (the points show the experimental data). The inset shows the temperature dependence of the resistance of the microbridge.

transition), and the width of the transition was from 0.5 to 1 K (at the 10–90% level of the residual resistance). The microbridges studied were 5–7 μm long, formed by electron-beam lithography and irradiation by hydrogen ions[7] in lines 20 μm wide and 250 μm long. The critical current density of the microbridges at 77 K was $j_c(77\ \mathrm{K}) = 1.2\times 10^6\ \mathrm{A/cm^2}$. The high values of j_c and the relatively large width of the microbridges allowed the formation of hysteresis in the current-voltage characteristics as a result of heating of the microbridges by the transport current. A current generator was used for measuring the current-voltage characteristics.

In the measurements of the microbridge characteristics hysteresis appeared in the current-voltage characteristics below a specified temperature T_0 (here T_0 is a characteristic temperature specific to each microbridge and depends on the heat transfer conditions; see the inset to Fig. 1): with increasing current through the microbridge a jump occurred in the current-voltage characteristic corresponding to higher voltages. With further increase in the current the relation between the current and the voltage was single-valued. With decreasing current the current-voltage characteristic returned to $V=0$ over a different path.

Poulin and coworkers[8] studied the switching from the superconducting state to the normal state by microbridges formed in films of $YBa_2Cu_3O_{7-x}$ high-temperature superconductors as the result of formation of a hot spot in them. In that investigation there was no hysteresis in the current–voltage characteristics, since a voltage generator was used for the measurements. Also analyzed was the equation for the heat flux in the microbridge, similar to those considered in Ref. 2, but with allowance for the linear temperature dependence of the resistance of the $YBa_2Cu_3O_{7-x}$. The following expression was found for the minimum current to maintain the hot spot

$$I_{\min} = \sqrt{\frac{\alpha w^2 d}{c}}\left[1-\frac{T^2}{T_c^2}\right]^{1/2}, \qquad (1)$$

where α is the heat transfer coefficient per unit area of the film surface, w and d are, respectively, the width and thickness of the film, c is the slope of the linear temperature dependence of the resistance, $r = r_0 + cT$, and T is the temperature at which the measurements were made.

In Fig. 1 we show the dependence of the current I_1 on the quantity $(1-T^2/T_c^2)^{1/2}$ for which the current-voltage characteristic returns to $V=0$ at a lower sweep current for one of the microbridges studied in these experiments. This figure shows that the expression (1) gives a good description of the experimental data (the points). It was assumed for these bridges that $I_c \propto (1-T/T_c)^{3/2}$ (Fig. 2), and therefore as the measuring temperature is lowered the minimum current required for maintaining the hot spot becomes lower than the critical current of the microbridge. Therefore the heat transfer from the $YBa_2Cu_3O_{7-x}$ microbridge can become insufficient for maintaining it in the resistive superconducting state. In this case, when transport current flows through the region of the microbridge where the order parameter, and hence the critical current, are minimum, vortex motion sets in; i.e., energy is dissipated. With further increase in the current through the microbridge the voltage jumps to values corresponding to the linear part of the voltage dependence of the current, and a hot spot is formed, whose length is equal to the length of the microbridge. If the current is then reduced, the dependence of the current on the voltage is linear (see the inset to Fig. 1), i.e., the dimensions of the hot spot remain nearly unchanged until the current reaches the value $I_1 = I_{\min}$. The deviation of the experimental data from the theoretical expression (1) with decreasing measurement temperature (which corresponds to higher values of $I_{\min}$) is probably due to heating of the substrate, i.e., the fact that the substrate temperature is raised above the temperature of the surrounding medium, since the measurements were carried out in helium vapor.

It should be noted that these phenomena in microbridges, described by the heat conduction equations (see Refs. 6 and 8), correspond to steady-state conditions. In fact, measuring the current–voltage characteristics with a current sweep involves transient conditions: a discontinuous increase in the voltage causes the hot spot to expand to the size of the microbridge length. At a sufficiently low measurement temperatures the hot spot cannot spread over the entire length of the microbridge; instead local heating occurs in the region of passage of a chain of vortices. The temperature in the heated region becomes so high that the microbridge is ''superheated.'' A visual analysis of the superheated microbridges showed tht some regions of the film were lighter colored than the rest of the film, and intersected the width of the traces. In addition, some samples even showed cracks in the substrate where the microbridge was superheated.

Using data similar to that presented in Fig. 1, and the temperature dependence of the microbridge resistance (the inset to Fig. 2 shows the temperature dependence of the resistance for the same microbridge whose characteristics are shown in Figs. 1 and 2), according to formula (1), we determined the heat transfer coefficient α. For the samples studied here, we found $\alpha = 5500–7500$ W/(cm$^2 \cdot$K). The resistance $R_{if} = (1.3–1.8) \times 10^{-4}$ (cm$^2 \cdot$K)/W, the inverse of the heat transfer coefficient, is in agreement with the data obtained by other methods.[4] We should point out that since the phonon wavelength (≈ 4Å at 100 K; Ref. 9) is considerably less than the thickness of the transition layer at the interface, the purity and perfection of the crystal structure of the transition layer will have a large effect on the efficacy of the heat transfer through the interface.

Using the value 0.9 J/(cm$^3 \cdot$ K) (Ref. 10) and also the value of R_{if} obtained in these experiments for a 2000 Å film, we estimate the thermal time constant to be 2–3 ns. These data are important for developing sensitive fast bolometers based on $YBa_2Cu_3O_{7-x}$ films.

[1] W. A. Little, Can. J. Phys. **37**, 334 1959.
[2] C. G. Levey, S. Etemad, and A. Inam, Appl. Phys. Lett. **60**, 126 (1992).
[3] M. Nahum, S. Verghese, and P. L. Richards, Appl. Phys. Lett. **73**, 2034 (1991).
[4] C. D. Marshall, A. Tokmakoff, and I. M. Fishman, J. Appl. Phys. **73**, 850 (1993).
[5] M. Tinkham, M. Octavio, and W. J. Skocpol, J. Appl. Phys. **49**, 1311 (1977).
[6] W. J. Skocpol, M. R. Beasley, and M. Tinkham, J. Appl. Phys. **45**, 4054 (1974).
[7] A. V. Pogrebnyakov, Vestsi Akad. Nauk Belarus, Ser. Fiz. Material. Navuk. No. 1, 94 (1994).
[8] G. D. Poulin, J. Lachapelle, S. H. Moffat *et al.*, Appl. Phys. Lett. **66**, 2576 (1995).
[9] T. Klitsner and R. O. Pohl, Phys. Rev. B. **36**, 6551 (1987).
[10] J. W. Loram, K. A. Mirsa, and P. F. Freeman, Physica C **171**, 243 (1990).

Translated by J. R. Anderson

Bolometric properties of silicon thin-film structures fabricated by plasmachemical vapor-phase deposition

V. Yu. Zerov, Yu. V. Kulikov, V. G. Malyarov, N. A. Feoktistov, and I. A. Khrebtov

S. I. Vavilov State Optics Institute, St. Petersburg
A. F. Ioffe Physicotechnical Institute, Russian Academy of Sciences, St. Petersburg

(Submitted January 20, 1997)
Pis'ma Zh. Tekh. Fiz. **23**, 63–68 (June 26, 1997)

A method of fabricating uncooled thermally sensitive sandwich structures based on amorphous hydrated silicon films is discussed and experimental results are reported. The structures have an area of 10^{-4} cm^2, a resistance of $\cong 10$ kΩ, and a temperature coefficient of resistance $\simeq 2\%$/K. At 30 Hz and a current of $\simeq 1$ μA, the excess noise exceeds the thermal resistance noise by a factor of 1.7. © *1997 American Institute of Physics.* [S1063-7850(97)02706-7]

One of the most important factors that determine the high utility of microelements for infrared detectors based on uncooled microbolometers[1–5] is the use of semiconductor thin films with a temperature coefficient of resistance of $\simeq 1\%$/K at room temperature and a low level of excess noise as the heat-sensitive materials. For this purpose amorphous or polycrystalline silicon films prepared by various methods[3,4,6] hold out promise. The work we report here involved an investigation of the bolometric and noise properties of hydrated amorphous silicon (a-Si:H) films prepared by plasmachemical vapor-phase deposition.

The application of plasmachemical vapor-phase deposition for preparing films of hydrated amorphous silicon to be used as the thermally sensitive layers of microbolometers is attractive for a number of reasons. Films can be produced with a resistivity in the range from 10^2 to 10^{11} $\Omega \cdot$cm and an activation energy in the range from 0.1 to 0.8 eV, which corresponds to a temperature coefficient of resistance at room temperature from 1%/K to 10%/K. However, the maximum activation energy is possessed by the film with the highest resistance. The plasmachemical vapor-phase deposition of the films was carried out at low substrate temperatures (200–300 °C), with various materials used for the substrate. Plasmachemical vapor-phase deposition is entirely compatible with the modern technology of silicon integrated circuits.

The optimum scheme for fabricating microbolometers using high-resistance thermally sensitive films with a resistivity of 10–100 k$\Omega \cdot$cm is the sandwich method.[3,6] In the sandwich structure the thermally sensitive layer is situated between metal film electrodes. This particular method was selected for preparing the test structures based on (a-Si:H) films. The samples were made using detachable copper-nickel masks in a topology corresponding to the sensing elements of the microbolometers. The substrates were wafers of glass ceramic 0.5 μm thick. The area of the sandwich was 100×100 μm. Chromium films were used as the electrodes, deposited by dc magnetron sputtering in an argon plasma.

Preparation of the thermally sensitive Cr–(a-Si:H)–Cr sandwich structures with the requisite characteristics required optimization of the deposition of the Cr layers with a specified conductance and optimization of the parameters for the deposition of the (a-Si:H) films with the maximum activation energy with a resistivity of 5–30 k$\Omega \cdot$cm and preparation of the highest-quality Ohmic contacts between the metal electrodes and the silicon film. The surface resistance of the electrodes (380 and 20 Ω) and thickness of the silicon film (0.7 μm) were selected in the light of the fact that the sandwich structure must have the properties of an optical cavity, tuned to a wavelength of $\simeq 10$ μm in order to obtain a high degree of absorption of the radiation in the wavelength range from 8 to 12 μm (Ref. 3). The required total resistance of the structures (5–20 kΩ) was obtained by light phosphorous doping of the a-Si:H films by plasmachemical vapor-phase deposition of silane with an admixture of phosphorous.

The current–voltage characteristics, the temperature dependence of the resistance, and the noise spectra were measured for the films prepared in this way. The temperature dependence of the resistance was measured in dc at 0.1–4 μA in the temperature range from 18 to 40 °C. The noise was studied in the frequency range from 10 to 1000 Hz with currents from 0.7 to 12 μA and with no current. The measuring circuit included a preamplifier with an intrinsic noise of 9 nV/Hz$^{1/2}$ at 12 Hz that decreased monotonically to 1.5 nV/Hz$^{1/2}$ at 1 kHz, and a SK4-56 spectrum analyzer. The measuring circuit was calibrated by measuring the thermal noise of a resistor of known value.

To estimate the quality of the Ohmic contacts, we first prepared structures of higher resistance, i.e., with lighter doping of the thermally sensitive layer. The resistance of the metal electrodes, 1–2 kΩ, had no effect on the current–voltage characteristics. Moreover, the fairly low conductance of the thermally sensitive layer assured us that only the area covered by the electrodes, 10^{-4} cm^2 was involved in the operation (that is, just the sandwich structure), while the surface conductance of the doped layers in this mask configuration was considerably lower than that of the structures. These structures had nonlinear current–voltage characteristics: when a bias of several volts was applied the current differed by more than two orders of magnitude for the two opposite polarities. The dependence of the resistance on the polarity of the applied voltage, the shape of the current–voltage characteristic, and the temperature dependence of the

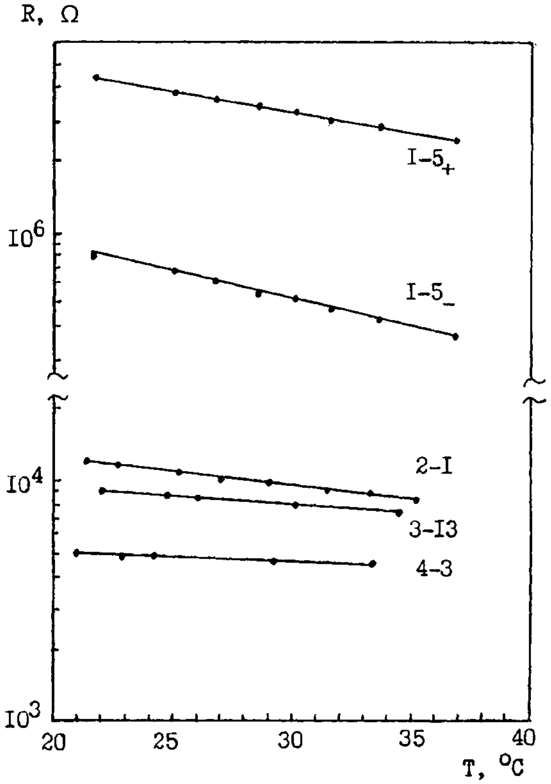

FIG. 1. Temperature dependence of the resistance of sandwich structures with n^+ layers at the contacts. The doping level of the thermally sensitive layer, the thickness, and the doping level of the n^+ layers are, respectively: *1–5* — 0.008%, 100 Å, and 0.1%; (the plus and minus signs indicate the dependences for different current directions); *2–1* — 0.1%, 200 Å, 2%; *3–13* — 0.1%, 400 Å, 2%; *4–3* — 0.3%, 200 Å, 2%.

resistance of these samples indicated the presence of Schottky barriers at the contacts, and possibly thin oxide films.[4,7]

To improve the quality of the contacts between the (a-Si:H) films and the electrodes in the subsequent depositions we introduced layers with enhanced carrier concentration (n^+ layers) of various thicknesses and doping level into the sandwich. We also varied the doping level of the thermally sensitive film in order to optimize the resistance and activation energy. The incorporation of the n^+ layer with a doping level of 0.1% and a thickness of 100 Å in the high-resistance structure with a doping level of 0.008% in the thermally sensitive layers did not produce the desired result. An example of the temperature dependence of the resistance of the high-resistance structure for various measuring currents is shown in Fig. 1 (sample *1–5*).

The greatest effect of improving the contacts was obtained for samples with n^+ layers 400 Å thick and a doping level of 2% (sample *3–13*). This is indicated both by the fact that the resistance is the same for opposite polarities of the applied voltage and by the nature of the noise spectra (Fig. 2). The main contribution to the noise voltage in sample *3–13* comes from the current noise and the thermal noise (Johnson noise) of the resistance. Calculations using a model of a bolometer on a solid substrate showed that the background noise voltage associated with the exchange of heat between the sandwich structure with the glass ceramic substrate for the currents cited in Fig. 2 is two or three orders of magnitude lower than the Johnson noise, and has no effect on the resultant noise.

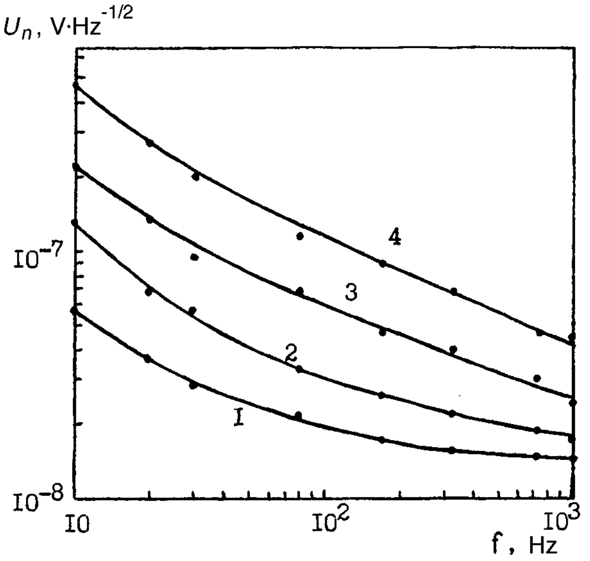

FIG. 2. Frequency dependence of the resultant noise voltage of sample *3–13* for various currents: *1* — 1.1 μA, *2* — 2.2 μA, *3* — 4.5 μA, *4* — 11.4 μA.

At a current of 1.1 μA and a frequency of 30 Hz the excess noise of sample *3–13* is a factor of 1.7 higher than the Johnson noise. At 1 kHz and the same current the noise is entirely determined by the Johnson noise. The frequency dependence of the spectral density of the excess noise power has the form $U_n^2 \propto 1/f^{1.0}$ and the current dependence is $U_n^2 \propto I^2$.

The maximum temperature coefficient of resistance (2.1%/K) for a resistance of 10–17 kΩ among the structures with good contacts is found in the samples with a doping level of 0.1% in the thermally sensitive layer (sample *2–1* in Fig. 1). Increasing the doping level to 0.3% resulted in a substantial drop in the temperature coefficient of resistance (sample *4–3*). The ratio of the maximum resistance to the minimum resistance of samples of one batch (16 sandwiches on a substrate 30×48 mm) in the worst case was 1.8, and the spread in the temperature coefficient of resistance was no higher than 30%. This last result is accounted for by the spread in the electrophysical properties of the a-Si:H films, and the reason for the former is also the spread in the dimensions of the detachable masks and how well they were affixed to the substrate.

In summary, we have prepared and studied sandwich structures with an area of 10^{-4} cm^2 that meet the requirements of the sensing elements of uncooled microbolometers. The method of fabricating the structures is compatible with modern silicon planar technology and provides a small spread in the parameters. When the resistances are optimized, the structures prepared in this manner have a temperature doe of resistance at the level of bolometers of realized uncooled infrared matrices. It is shown possible to reduce the contact noise of the structures at the operating frequencies of the uncooled matrices and at currents of ~1 μA and obtain a resultant noise voltage at the level of the Johnson noise.

The part of this work involving the noise studies was supported by the Russian Fund for Fundamental Research, Project No. 96-02-18563.

[1] R. E. Flannery and J. E. Miller, Proc. SPIE **1689**, 379 (1992).
[2] R. A. Wood, Proc. SPIE **2020**, 322 (1993).
[3] K. C. Liddiard, Proc. SPIE **1969**, 206 (1993).
[4] M. H. Unewisse, B. I. Craig, R. J. Watson, and K. C. Liddiard, Proc. SPIE **2554**, 43 (1995).
[5] N. Bulter, R. Blackwell, R. Murphy R. *et al.*, Proc. SPIE **2552**, 583 (1995).
[6] K. C. Liddiard, M. H. Unewisse, and O. Reinhold, O. Proc. SPIE **2225**, 62 (1994).
[7] A. A. Andreev, O. A. Golikova, P. M. Karageorgiĭ-Alkalaev, A. Yu. Leĭderman, M. M. Mezdrogina, V. S. Rubin, and N. A. Feoktistov, Fiz. Tekh. Poluprovodn. **18**, 373 (1984) [Sov. Phys. Semicond. **18**, 233 (1984)].

Translated by J. R. Anderson

Interaction between a ferromagnet and a high-temperature superconductor at the interface in thin-film heterostructures

C. V. Yakovlev, L. A. Kalyuzhnaya, G. A. Nikolaĭchuk, T. A. Krylova, and B. M. Lebed'

''DOMEN'' Scientific Research Center, St. Petersburg

(Submitted January 21, 1997)
Pis'ma Zh. Tekh. Fiz. **23**, 69–73 (June 26, 1997)

The development of high-temperature superconductor (HTSC)/ferromagnet thin-film heterostructures is a promising direction in their application to spin-wave electronics. The state of the HTSC–ferromagnet interface determines the nature of the propagation of the surface magnetostatic waves in the heterostructure. The formation of the HTSC films in the heterostructures involves thermal treatment at high temperatures, which results in the diffusion interaction of the HTSC films and the ferromagnet. The heterostructure consists of a $YBa_2Cu_3O_{7-x}$ HTSC film deposited by pyrolysis on an $Y_3Fe_5O_{12}$ ferromagnetic film grown epitaxially on a (111)-oriented gadolinum-gallium garnet $Gd_3Ga_5O_{12}$ substrate. The interdiffusion is studied from the intensity distribution curves of the x rays of iron (Fe), barium (Ba), copper (Cu), and silver (Ag), the last introduced into the HTSC in the amounts of 5–50 wt.%. The thin-film heterostructures are studied in the microwave range. A correlation is found between the state of the interface and the microwave characteristics. © *1997 American Institute of Physics.* [S1063-7850(97)02806-1]

The development of high-temperature superconductor (HTSC)/ferromagnet thin film heterostructures is a promising direction in their application to spin-wave electronics.[1] It has been shown that the state of the HTSC-ferromagnet interface in thin-film heterostructures determines the nature of the propagation of surface magnetostatic waves.[2] The formation of the HTSC films in the heterostructures involves thermal treatment at fairly high temperatures (900 °C), where diffusion interaction can take place at the interface between the film and the substrate, particularly with ferromagnetic substrates.

The work reported in this paper deals with the diffusion processes at the $YBa_2Cu_3O_{7-x}$–$Y_3Fe_5O_{12}$ interface and their dependence on the conditions for preparing the HTSC films in the thin-film heterostructures and the effect of the state of the interface on the conditions of propagation of the magne-

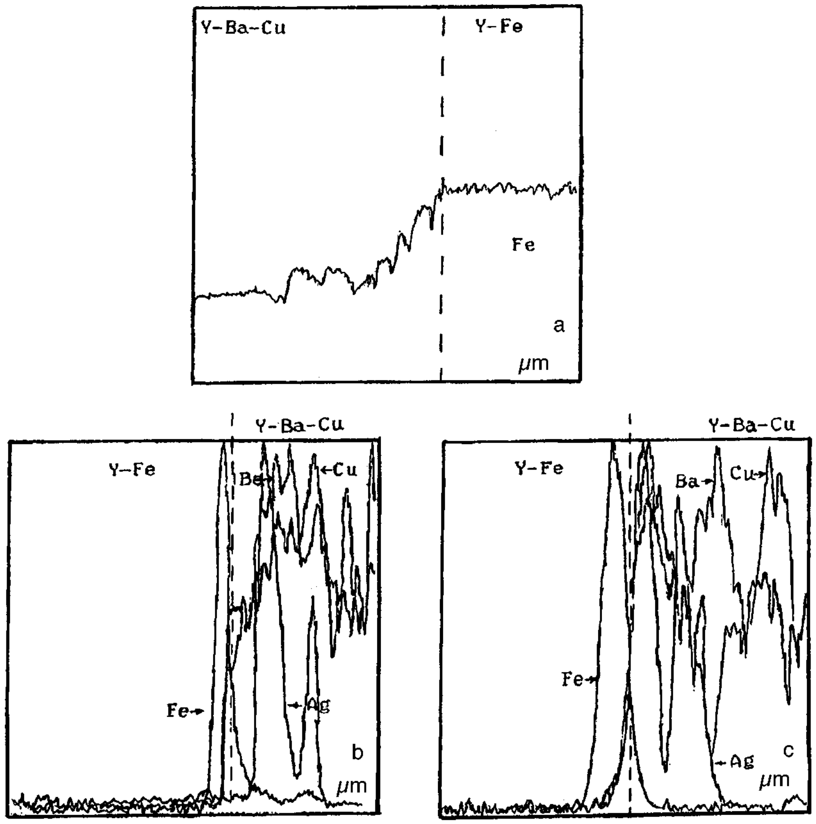

FIG. 1. X-ray intensity distributions for Fe, Ba, Cu, and Ag in YIG–HTSC thin-film heterostructures: a—0 wt.% Ag; b—5 wt.% Ag; c—30 wt.% Ag.

tostatic waves in these structures. The HTSC films of $YBa_2Cu_3O_{7-x}$ were prepared by pyrolysis on an yttrium iron garnet $Y_3Fe_5O_{12}$ (YIG) surface grown epitaxially on a (111)-oriented gadolinium–gallium garnet $Gd_3Ga_5O_{12}$ (GGG) substrate. In preparing the HTSC films in the HTSC–YIG thin-film heterostructures we used HTSC powder obtained from a solution of nitrates of yttrium (Y), barium (Ba), and copper (Cu), doped with silver (Ag).

The silver was added to the mixture in the form of a finely disperse powder with a grain size of 1.0–2.0 μm above the stoichiometric composition in the amount of 5–50 wt.%. A suspension of HTSC powder in an organic binder (triethanolamine) was deposited on the YIG epitaxial film by centrifuging (rotation speed of 2000 rpm). The thin-film heterostructures were first thermally treated at 550 °C in air, and then were thermally treated in various temperture-time regimes in an oxygen atmosphere. The thin-film heterostructures prepared in this way were studied by x-ray microanalysis in an S-570 Hitachi scanning electron microscope with an x-ray spectrometer from the Link company.

The measurements were carried out at a potential of 30 kV and a current of 1×10^{-9} A and the diameter of the probe was 200 Å. For the thin-film heterostructures with the HTSC film containing 0, 5, 30, and 50 wt.% silver we measured the intensity distribution of the iron, barium, copper, and silver x rays. The experiments were carried out by scanning over the end surface of a cleaved-off portion of the GGG–YIG–HTSC heterostructures.

In Fig. 1 we show the x-ray intensity distribution curves for various concentrations of silver in the HTSC film: *a* — 0 wt.% Ag, *b* — 5 wt.% Ag, *c* — 30 wt.% Ag. This figure shows that the Fe diffused in all of the thin film structures on the substrate (the YIG film) into the HTSC film. Without silver (0 wt.%) the iron propagated nearly over the entire thickness of the HTSC film (Fig. 1a). For a 5 wt.% Ag concentration the depth of penetration of the iron into the HTSC film was 15 μm (Fig. 1b). With increasing silver concentration up to 30–50 wt.% the depth of penetration of the iron decreased to 3 μm (Fig. 1c).

It has thus been established that the depth of penetration of iron depends on the concentration of the added silver.

No diffusion of the HTSC elements barium and copper into the substrate (the YIG film) was observed. From an x-ray spectral analysis of the distribution patterns of the silver x-ray intensity a nonequilibrium distribution of the silver over the HTSC film was found. It should be noted that as the silver concentration in the film increases, the silver is mainly concentrated near the film-substrate interface (Figs. 1b and c). It is likely that this distribution results in a decrease in the depth of penetration of iron from the YIG into the HTSC film.

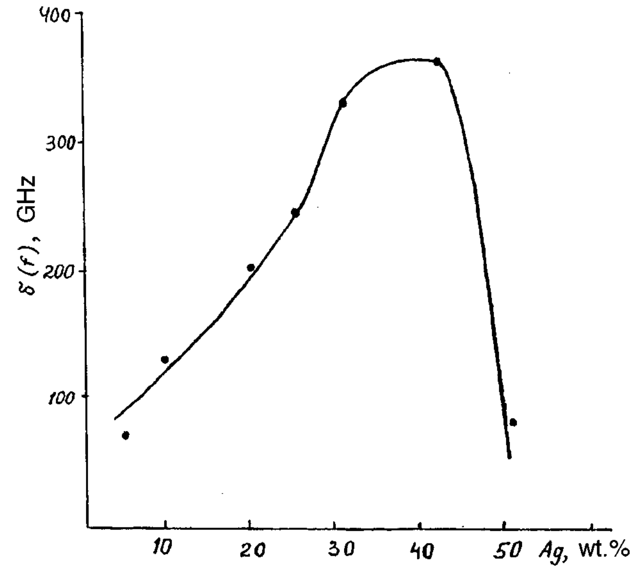

FIG. 2. Effect of the silver concentration in the HTSC power of composition $YBa_2Cu_3O_{7-x}$ on the broadening of the amplitude-frequency characteristic $\delta(f)$ in the microwave range.

The thin-film heterostructures that were prepared were studied in the range of frequencies 3–5 GHz and at 77 K. The measurements were made on devices based on the magnet–HTSC structure by the method described in Ref. 1. Studies were made of the dependence of the measured pass band $\delta(f)$ of the amplitude–frequency characteristic of magnetostatic waves on the superconducting properties of the film. For this frequency range we show in Fig. 2 curves of $\delta(f)$ of the amplitude–frequency characteristics plotted against the silver concentration in the HTSC film (0–50 wt.%). The maximum value of $\delta(f)$ was found for heterostructures with a silver content of 30–40 wt.%. An increase in $\delta(f)$ is associated with the state of the interface and with the improved characteristics of the HTSC film.

In summary, we have studied for the first time the diffusion state of the interface for HTSC–ferromagnet thin-film heterostructures. It has been determined that the state of the interface is governed by the amount of added silver in the HTSC film, and a correlation has been observed between the state of the interface and the microwave characteristics.

This work was performed with the support of the Russian Fund for Fundamental Research (Project No. 96-02-16297-a).

[1] A. B. Al'tman, B. M. Lebed', A. V. Nikiforov, S. V. Yakovlev, and I. A. Yakovlev, Sverkhprovodimost' (KIAE) **3**, 2205 (1990) [Superconductivity **3**, 1638 (1990)].

[2] B. M. Lebed, S. V. Yakovlev, G. A. Nikolaĭchuk, L. A. Kalyuzhnaya, T. A. Krylova, and M. P. Vatnik, Pis'ma Zh. Tekh. Fiz. **22**(10), 18 (1996) [Tech. Phys. Lett. **22**, 395 (1996)].

Translated by J. R. Anderson

Superconducting fast detector based on the nonequilibrium inductance response of a film of niobium nitride

E. M. Men'shchikov, I. G. Gogidze, A. V. Sergeev, A. I. Elant'ev, P. B. Kuminov,
G. N. Gol'tsman, and E. M. Gershenzon

Moscow State Pedagogical University

(Submitted February 5, 1997)
Pis'ma Zh. Tekh. Fiz. **23**, 74–80 (June 26, 1997)

A new type of fast detector is proposed, whose operation is based on the variation of the kinetic inductance of a superconducting film caused by nonequilibrium quasiparticles created by the electromagnetic radiation. The speed of the detector is determined by the rate of multiplication of photo-excited quasiparticles, and is nearly independent of the temperature, being less than 1 ps for NbN. Models based on the Owen–Scalapino scheme give a good description of the experimentally determined dependence of the power-voltage sensitivity of the detector on the modulation frequency. The lifetime of the quasiparticles is determined, and it is shown that the reabsorption of nonequilibrium phonons by the condensate has a substantial effect even in ultrathin NbN films 5 nm thick, and results in the maximum possible quantum yield. A low concentration of equilibrium quasiparticles and a high quantum yield result in a detectivity $D^* = 10^{12}\ \mathrm{W}^{-1}\cdot\mathrm{cm}\cdot\mathrm{Hz}^{1/2}$ at a temperature $T = 4.2$ K and $D^* = 10^{16}\ \mathrm{W}^{-1}\cdot\ \mathrm{cm}\cdot\ \mathrm{Hz}^{1/2}$ at $T = 1.6$ K. *© 1997 American Institute of Physics.* [S1063-7850(97)02906-6]

An important direction in the modern technology of infrared and submillimeter waves is the development of faster radiation detectors with a characteristic time τ_D in the femtosecond range. A new class of detectors has been developed — superconducting electronic bolometers — whose operation is based on the nonlinear response of thin structured superconductor films in the resistive state.[1] In this kind of detector a change in the electron temperature due to the radiation causes an increase in the resistance of the film near the critical temperature T_c of the superconductor. Because of the good acoustic coupling of the film with the substrate the phonons remain in equilibrium and serve as a constant temperature bath for the electrons. The time constant for this detector is equal to the relaxation time of the electrons via the phonons, τ_{eph}, and its detectivity D^* is determined by the fluctuations of the electron temperature. To increase the response speed requires an increase in the electron-phonon relaxation rate. This, in turn, requires that the phonon subsystem in the film be also heated in addition to the electrons, and a relatively slow bolometric component appears in the dependence of the signal on the modulation frequency of the radiation, the time of which increases with decreasing frequency, which has a deleterious effect on the detector characteristics.

To overcome these deficiencies in the response speed of resistive detectors, we propose to use superconducting nonequilibrium detectors, which operate on the principle of a variation of the kinetic inductance of the superconducting condensate under the action of the radiation. We note that a previously proposed inertia bolometer[2,3] utilized the temperature dependence of the kinetic inductance near T_c. We shall study a fast detector based on the nonequilibrium response of thin films operating at a temperature considerably lower than T_c. The time constant τ_D of such a detector is defined as the time for the development of an electron avalanche, which is much shorter than τ_{eph}. Moreover, the detectivity of this detector is much higher than resistive electronic bolometers with comparable times τ_D. For a concrete realization of the detector based on the kinetic inductance we have selected thin films of NbN, a material with a high T_c that is also highly recommended for application in resistive detectors.[4]

Niobium nitride films with a thickness d of 5 and 10 nm were prepared by reactive dc magnetron sputtering.[5] The critical temperatures T_c were 12.4 and 14.3 K, respectively, and the width of the superconducting transition was $\Delta T_c \sim 0.2$ K. The samples were formed in a meander shape (the stripe width was $\omega = 1.5\ \mu$m), which filled an area of $54\times 72\ \mu$m.

In the experiment we measured the ac voltage ΔU induced across the sample by modulation of the near-infrared light when the sample was connected into a circuit with a dc current I. The source of the radiation was an RLD-78M20 semiconductor laser diode with a maximum power of 10 mW and a wavelength of 788 nm. The modulated power of the radiation of the laser diode was calibrated by an LFDG-70A fast detector in the modulation frequency band to 4 GHz. The laser radiation was focused by an optical system and was directed at the sample through an optical fiber with a diameter of 50 μm. The signal from the sample at frequencies to 50 MHz was recorded by a lock-in amplifier from the EGG company (model 5202) and at frequencies up to 4 GHz by an SK4-60 spectrum analyzer.

In Fig. 1 we present the signal voltage for two samples at different temperatures as functions of the modulation frequency f. The signal amplitude is well approximated by the function

$$\Delta U(f) = \frac{U_0 \cdot 2\pi f \tau}{\sqrt{1 + (2\pi f \tau)^2}}. \tag{1}$$

The values of τ are shown by the arrows in Fig. 1. For a

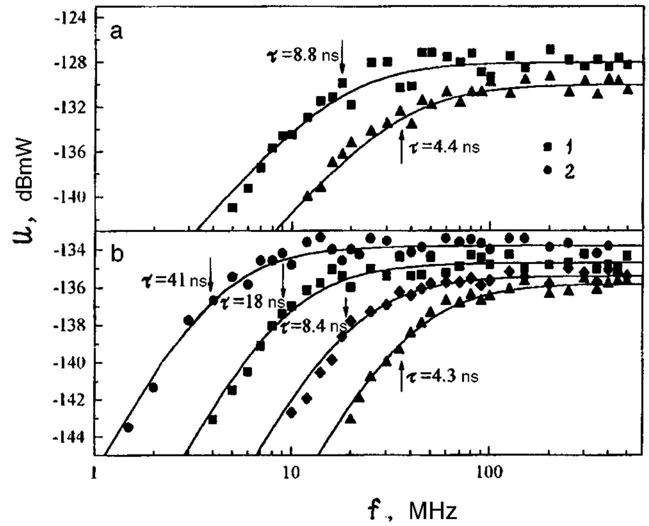

FIG. 1. Dependence of the kinetic inductance signal ΔU on the modulation frequency for film thickness 5 nm (a) and 10 nm (b). The arrows indicate the values of τ corresponding to formula (1).

constant reduced temperature T/T_c the values of τ are proportional to the film thickness. At low temperatures, τ for each sample depends exponentially on the temperature. The magnitude of the signal on the plateau of the frequency dependence increases slowly, as $T^{-1/2}$, with decreasing temperature.

The experimental results presented here can be accounted for in terms of the following model based on the Owen–Scalapino scheme.[6] The absorption of photons of energy $h\nu$ greater than the gap Δ breaks up the Cooper pairs with the formation of quasiparticles, which causes a change in the kinetic inductance L of the film, and consequently gives rise to a voltage IdL/dt. The rate of change of the inductance is determined by the modulation frequency of the radiation and the relaxation processes in the film At first the photoexcited quasiparticles lose energy and emit phonons with an energy higher than 2Δ, which in turn break up the Cooper pairs and create new quasiparticles. If the quasiparticle energy is below 3Δ, then further multiplication of quasiparticles is not possible. Then the nonequilibrium quasiparticles cool, radiating low-energy phonons, and accumulate at the level with the energy Δ. At this stage, which takes no more than 1 ps, the development of the electron avalanche terminates, and the subsequent, slower evolution leads to a decrease in the concentration of nonequilibrium quasiparticles. In the recombination of two particles a phonon with an energy 2Δ is emitted, which can either enter the film in a time $\tau_{es}=4d/\alpha v_s$ (here v_s is the speed of sound and α is the film-substrate transmission coefficient), or in a time τ_B can break up a Cooper pair. As a result, the effective lifetime of a quasiparticle is

$$\tau_l=\tau_R\left(1+\frac{\tau_{es}}{\tau_B}\right). \tag{2}$$

Following the work of Sergeev *et al.*,[7] we can write the power-voltage sensitivity as

$$S=\frac{LI\exp(-\Delta/k_BT)}{n_{eqv}V\Delta}\,\frac{2\pi f\tau_l}{\sqrt{1+(2\pi f\tau_l)^2}}\,\frac{1}{\sqrt{1+(2\pi f\tau^*)^2}}, \tag{3}$$

where τ^* is the time of development of the electron avalanche.

Let us estimate the numerical values of the characteristic times that enter into Eqs. (2) and (3) for the thinnest film The recombination time at a temperature much lower than T_c can be expressed in terms of the electron-phonon relaxation at the critical temperature, $\tau_{eph}(T_c)$:

$$\frac{\tau_R(T)}{\tau_{eph}(T_e)}=0.1\left(\frac{T_c}{T}\right)^{1/2}\exp\left(\frac{\Delta}{k_BT}\right). \tag{4}$$

Using the data on the resistive response of NbN thin films[8] we find for a sample with a thickness of 5 nm the times $\tau_{es}=40$ ps and $\tau_{eph}(T_c)$ = 5 ps, which for a temperature $T=4.2$ K gives τ_R = 50 ps. The time τ_B does not depend on the temperature and can be estimated from the relation

$$\tau_B=\frac{v_s}{v_F}\,\frac{h}{2\pi\Delta}, \tag{5}$$

which gives a value $\tau_B=2$ ps. Thus $\tau_{es}/\tau_B\approx 20$, which indicates strong reabsorption of the nonequilibrium high-energy phonons by the quasiparticles. The lifetime of the quasiparticles calculated by formula (2) with the value of τ_R (formula (4)) is in good agreement with the experimental values of τ given in Fig. 1. We note that the strong reabsorption of the phonons improves the characteristics of the detector, since in this case, as a result of the electron avalanche, the maximum value of the multiplication coefficient of quasiparticles, $K=h\nu/2\Delta$ is attained.

Let us now consider the parameters of the nonequilibrium inductance detector. We assume that for operation of the detector we will use the plateau of the frequency dependence in Fig. 1. Then the detector has an output frequency pass band Δf from the inverse quasiparticle lifetime to the inverse time of development of the electron avalanche. The time of development of the avalanche was estimated in optical experiments on the modulation of the transmission coefficient,[9] which showed that τ^* was shorter than 0.5 ps.

The power-voltage sensitivity on the plateau is

$$S=\frac{LI\exp(-\Delta/T)}{\Delta n_{eqv}}\propto T^{-1/2}, \tag{6}$$

where n_{eqv} is the equilibrium quasiparticle concentration, which decreases exponentially with lowered temperature.

The main noise source of the detector is the generation-recombination noise, and the corresponding detectivity, and is equal to

$$D^*=\sqrt{\frac{\tau_l}{4\Delta^2 n_{eqv}d}}. \tag{7}$$

Using an electron concentration $\sim 10^{22}$ cm^{-3}, we obtain a concentration of equilibrium quasiparticles at 4.2 K of $n_{eqv}\approx 10^{17}$ cm^{-3} and correspondingly a value of D^* equal to 10^{12} W$^{-1}\cdot$cm$\cdot$Hz$^{1/2}$.

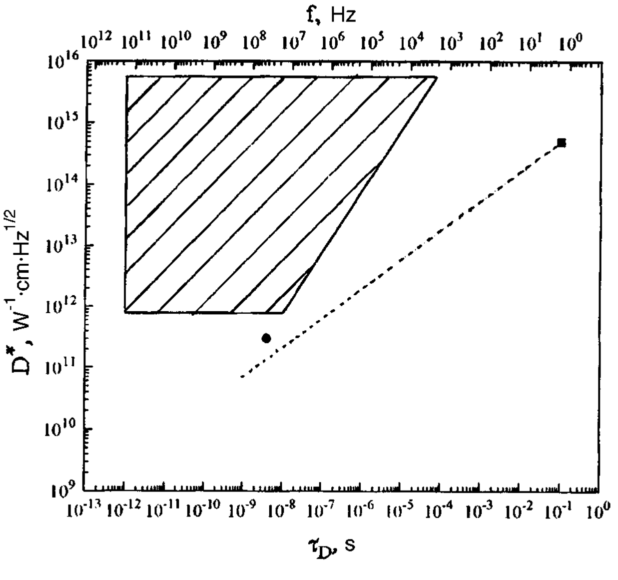

FIG. 2. Comparison of the characteristics of various superconducting bolometers plotted as the detectivity versus the time constant *1* — Al bolometer, *2* — resistive electronic bolometer made of Nb; the dashed line indicates the relation of the detectivity to the time constant used for the superconducting resistive bolometers. The hatched region shows the detectivity and the output frequency pass band of a NbN detector based on the kinetic inductance for various temperatures (the upper boundary corresponds to $T=1.6$ K and the lower boundary to $T=4.2$ K.

A comparison of the inductance detector with other superconducting detectors is shown in Fig. 2. For an inductance detector the time constant is equal to the time of development of an avalanche, which is nearly independent of the temperature. The detectivity increases with decreasing temperature (formula (7)) and is $D^*=10^{12}$ $\mathrm{W}^{-1}\cdot\mathrm{cm}\cdot\mathrm{Hz}^{1/2}$ at $T=4.2$ K and $D^*=10^{16}$ $\mathrm{W}^{-1}\cdot\mathrm{cm}\cdot\mathrm{Hz}^{1/2}$ at $T=1.6$ K. In Fig. 2 the left-hand boundary of the hatched region corresponds to this increase in D^*. In addition, for a fixed temperature the output frequency band is bounded from below by the quantity τ_l^{-1}, which depends on the temperature and is shown in Fig. 2 on the right-hand boundary of the hatched region. The upper boundary corresponds to the operating temperature of 1 K, and the lower boundary to 4.2 K. For comparison we have chosen the sensitive membrane-type Al bolometer with a record value of D^*, and also a fast nonequilibrium resistive NbN detector operating near the transition point. As one can see, the nonequilibrium inductance detector has a high detectivity because of the low concentration of quasiparticles and a record speed of response. A deficiency of this detector is the low power-voltage sensitivity, which demands very stringent requirements on the amplifier in the detection system.

The authors of this paper extend their thanks to B. M. Voronov for making the samples and A. L. Dzardanov for preparing the low-noise amplifier.

The work was supported by the State Program ''Important Problems in the Physics of Condensed Media,'' ''Superconductivity'' section, in the Project No. 96128, ''Gorizont III.''

[1] E. M. Gershenzon, M. E. Gershenzon, G. N. Goltsman *et al.*, Zh. Tekh. Fiz **59**(2), 111 (1989) [Sov. Phys. Tech. Phys. **34**, 195 (1989)].

[2] E. N. Grossman, D. G. McDonald, and J. E. Sauvaeau, IEEE Trans. Magnetics **MAG-27**, 2677 (1991).

[3] N. Bluzer, J. Appl. Phys. **78**, 7340 (1995).

[4] G. N. Gol'tsman, A. D. Semenov, Yu. P. Gousev *et al.*, Supercond. Sci. Technol. **4**, 453 (1991); B. M. Voronov, E. M. Gershenzon, G. N. Gol'tsman, *et al.*, Sverkhprovodimost' (KIAE) **5**, 955 (1992) [Superconductivity **5**, 960 (1992)].

[5] B. M. Voronov, E. M. Gershenzon, L. A. Seĭdman *et al.*, Sverkhprovodimost' (KIAE) **7**, 1097 (1996).

[6] C. S. Owen and D. J. Scalapino, Phys. Rev. Lett. **28**, 1559 (1972).

[7] A. V. Sergeev and M. Yu. Reizen, Int. J. Mod. Phys. B **10**, 635 (1996).

[8] A. D. Semenov, R. S. Nebosis, Yu. P. Gousev *et al.*, Phys. Rev. B **52**, 581 (1995).

[9] A. D. Semenov, M. A. Heusinger, K. F. Renk *et al.*, IEEE Trans. Applied Superconductivity (1997) (accepted IEEE Trans. Appl. Supercond.); D. W. Face, S. D. Brorson, A. Kazeroonian *et al.*, IEEE Trans. Magnetics **MAG-27**, 1556 (1991).

Translated by J. R. Anderson

Simulation of impact-induced generation of hypersonic phonons and the resonance principle of activation of the compaction of nanopowders

V. V. Pokropivnyĭ, V. V. Skorokhod, A. V. Pokropivnyĭ, and Yu. G. Krasnikov

I. N. Frantsevich Institute of Problems in Materials Science, Ukrainian National Academy of Sciences, Kiev
Moscow Physico-Technical Institute, Dolgoprudnyĭ

(Submitted January 24, 1997)
Pis'ma Zh. Tekh. Fiz. **23**, 81–88 (June 26, 1997)

Computer simulation is used to study the generation of induced hypersonic phonon oscillations at the instant of impact of α-Fe nanoparticles. A principle is proposed for the resonance amplification of these oscillations and the activation of the compaction of the nanoparticles by means of selective ultrasonic/hypersonic action or infrared/microwave radiation synchronous with the impact. © *1997 American Institute of Physics.* [S1063-7850(97)03006-1]

It is well known that mechanical, ultrasonic, and microwave treatment activates the sintering of powders. In mechanical activation in a ball mill the energy of deformation is converted into the energy of surface defects and elastic energy, whose increase during sintering promotes local heating, accommodation, and joining of the surfaces. More recently explosive technology has been rapidly developed for the compaction of ultradisperse superhard particles, particularly diamond particles.[1,2] It is believed that the union of the particles in these cases occurs through a mechanism of surface melting. According to the theory of Koenig, after an inelastic collision of particles in the absence of external forces the relative motion of the particles of the system ceases, i.e., the two particles move as a unit, and part of the kinetic energy is converted into internal energy. In the real case the particle is acted on by both the external deformation force and the variable-sign adhesion force, which depends on the thickness of the gap between the particles. This must generate induced oscillations of both particles. Thölen[3] has shown theoretically that the balance between the surface and elastic energy results in high-frequency longitudinal vibrations of the two small contacting particles with a frequency $\omega=(3ES/m)^{1/2}$, where E is Young's modulus, S is the radius of the contact area, and m is the mass of the particles. These are acoustic phonon oscillations in the frequency range $0\leqslant\omega\leqslant\omega_D$ where ω_D is the Debye frequency, which is 7.77 THz for Fe and 38.75 THz for diamond. The vibrational frequency of 30 nm Ni particles is $\omega=5.7$ GHz. However, because of the surface roughness of the initial particles, the real contact area of the particles is indeterminate, and therefore it is in practice not possible to calculate the frequency by this means. High-frequency tip oscillations of this type also occur in the atomic-force microscope.[4] V. F. Anisichkin first called attention to the effect of resonance solid-phase coalescence of small diamond particles in an explosion.[5] He calculated qualitatively the ''magic'' particle size at which a dip and a maximum appear in the particle size distribution in the explosion products. However, the mechanism for this resonance avalanche-like union of the lattices was not established.

In this investigation we have used computer simulation to study the effect of induced acoustic hypersonic phonon oscillations in the impact of α-Fe nanoparticles and find justification for a resonance principle for the ultrahypersonic and complex impact-microwave compaction of a nanopowder.

For the simulation of the inelastic impact of nanoparticles by the method of molecular dynamics we used the SIDEM/ASMIT software.[6] Flexible boundary conditions were used, which corresponds to the collision of free nanoparticles. The beam particle is cubic or conical, and the target particle is cubic. The planar cross section of the structure of the particles was imaged by a visualization program on the

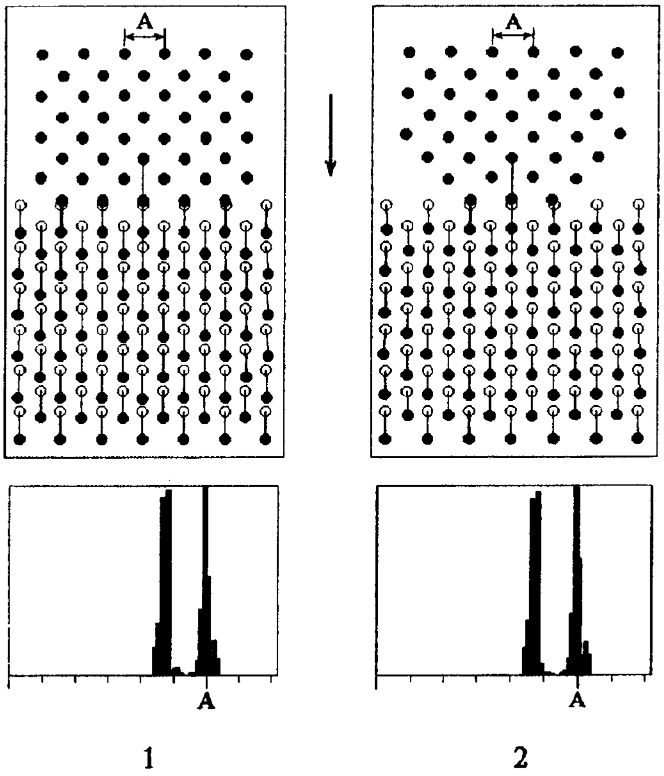

FIG. 1. Configurations of atomic displacements and radial distribution functions of the upper beam particle and the lower target particle at the instant of impact. The dark circles show the atoms of the plane of a (100) cross section. The open circles below the dark circles are the starting position of the atom before relaxation. The lines connecting the atoms are the adhesive bonds between the two particles. The arrow indicates the direction of the impact.

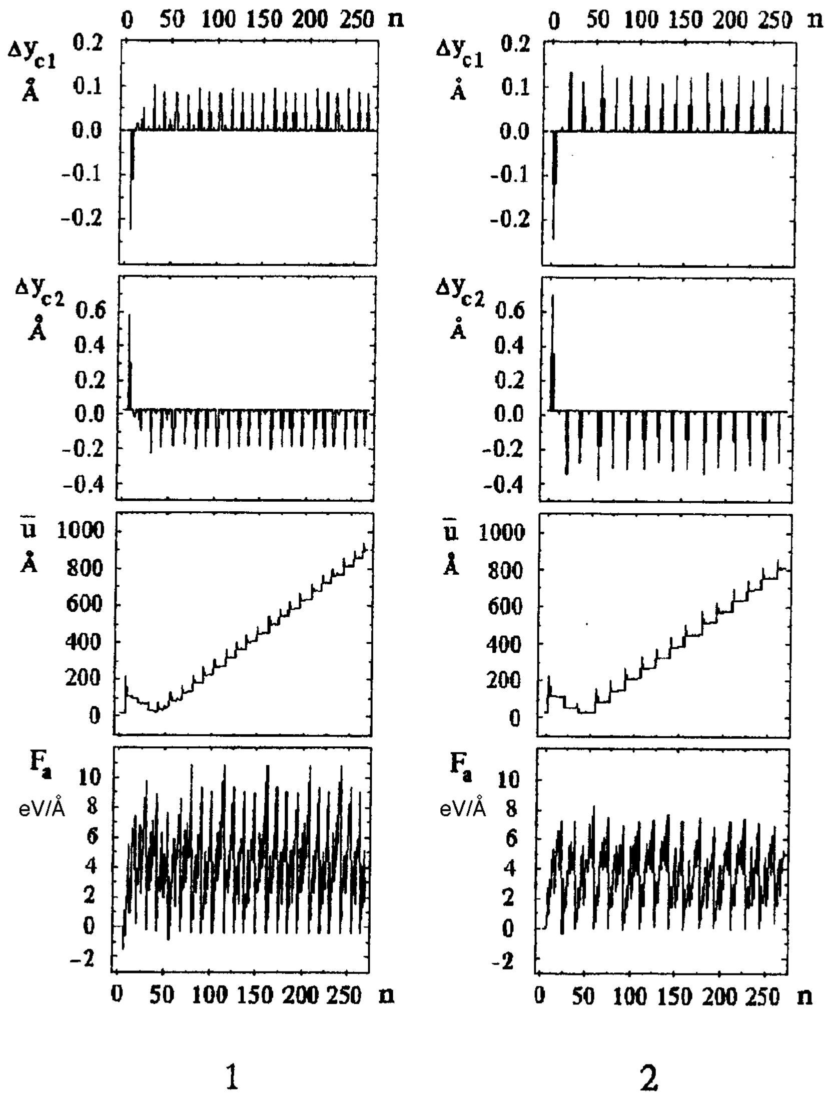

FIG. 2. Oscillations of the center of mass of the beam particle, Δy_{c1}, and the target particle, Δy_{c2}, the sum of the rms displacements u of all the atoms, and the adhesive force F_a at the nth step of the impact 1 Å = 10^{-10} m, 1 eV/Å = 1.602 nN.

computer monitor, and is shown in Fig. 1. Also shown is the radial distribution function, which shows the relative number of atomic pairwise bonds as a function of the bond length. We use the regime of alternate impact and relaxation — after the relaxation is completed all the atoms of the beam particle are displaced along the normal to the target particle with a step $\Delta y = 0.01$ A (the quantity $A = 0.28665$ nm is the lattice constant of α-Fe) and an initial velocity $v \sim 1430$ m/s. At each n-th step the displacement of the center of mass of the beam particle, Δy_{c1}, and of the target particle, Δy_{c2}, along the y-axis of the impact, and also the sum of the rms displacements of all the atoms of the crystal, $\overline{u} = \Sigma \sqrt{\overline{u^2}}$ are calculated. The interatomic interactions were calculated for a short-range nonlocal surface potential $\varphi(r)$ (Ref. 7). By summing the pair-wise bonds between the beam particle i and the target particle j we calculated the adhesive force $F_a = -\Sigma d\varphi(r_{ij})/dr_{ij}$. The variation of the numerical characteristics is shown in Fig. 2. For the calculation of the induced oscillations of the nanoparticles we have applied for the first time a spectral-time analysis with the use of the VRN software.[8] We calculated the spectral-time diagram (‘‘svan’’), which shows the frequency ω and the relative amplitudes of the Fourier spectrum of oscillations at each instant of time t, and also the time-averaged spectrum amplitude, showing the average density of phonon oscillations $g(\omega)$ (Fig. 3). This is in fact a new method of computer calculation of the phonon spectrum. To reveal the dependence of the frequency on the mass we carried out two experiments: in the first the projectile and the target contained, respectively 192 and 474 atoms; in the second these numbers were 178 and 280.

The results of the simulation are shown in Fig. 1–3, where the labels 1 and 2 correspond to the first and second computer experiment, respectively. Before the impact, the outer surface layer relaxes inward.[7] At the first instant of the interaction the atoms of the first, second, third, and fourth surface layers of both particles are displaced so sharply in opposite directions to one another, that large jumps appear in the displacements and the displacements of the centers of mass of the particles in Fig. 2. This is the well-known phenomenon of cohesive collapse.[9–11] It is remarkable that after a short transition period of chaotic oscillations, the oscillations become strictly periodic (Fig. 2). Stable oscillatory-translational motion of both particles as a unit begins, which

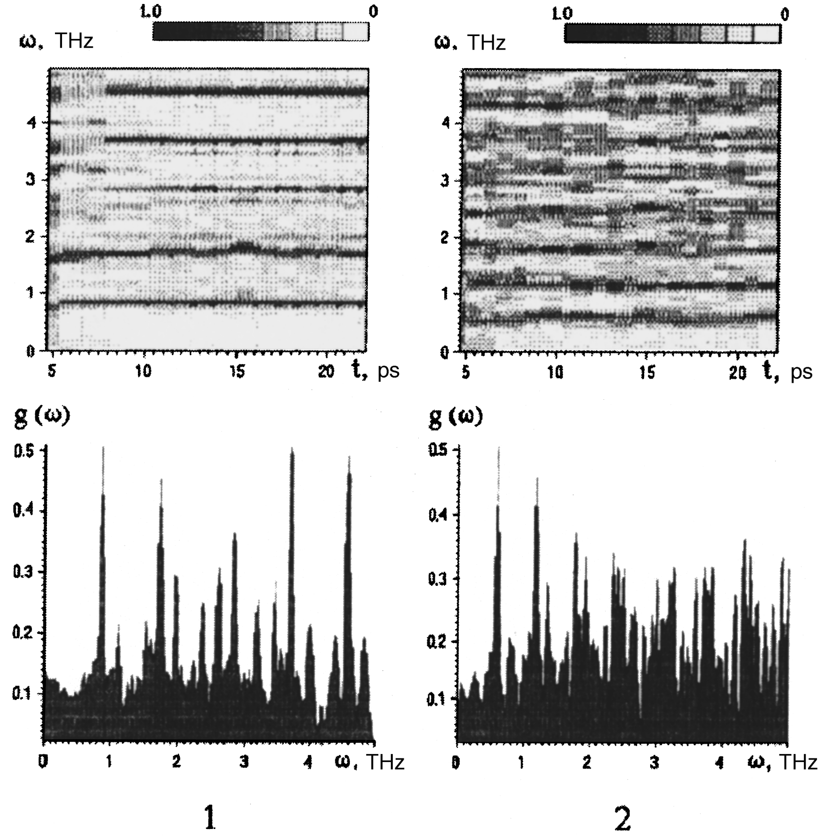

FIG. 3. Spectral-time diagram and phonon spectrum of the induced oscillations of the center of mass of the target particle. On this ''svan'' diagram the dark shadowing corresponds to a large amplitude of the spectrum in relative units. The length of the darkened bands corresponds to stable oscillatory modes.

can last for an infinite time by virtue of the external energy of the impact pulses. The first coordination sphere in the radial distribution function splits. We note that this same effect of generation of induced mechanical oscillations also appears when the direction of the external momentum is reversed, i. e., with impact elongation. We note also that the momentum from the projectile is transferred to the target particle in the second experiment through a relatively narrow adhesion contact. Consequently the nanoparticles transfer pressure through the contact just as a liquid does, in accordance with Pascal's law.

In Fig. 3 we show the spectral-time diagram and the spectrum of the oscillations of the center of mass of the target particle. Compared with the spectrum of free oscillations of an ideal lattice in the Debye theory, the phonon spectrum of the induced oscillations on top of the general background shows a number of peaks at frequency multiples. In the first experiment these frequencies were $\omega_k \simeq 0.9$ THz $(k=1,2,3,4,5)$, with the peak split for $k=3$, and in the second experiment $\omega_k \simeq 0.6$ THz $(k=1-8)$, with the peaks $k=4-8$ split. The frequency of these oscillations falls in the hypersonic range and below the Debye frequency ω_D. Consequently these are induced acoustic phonon oscillations. We note that these oscillations are like surface oscillations, and therefore they are erroneously perceived as surface melting. The oscillation frequency is determined by the type of material and the particle size, and in the present case falls in the hypersonic range. This frequency should decrease as $\omega_k \propto 1/m^{1/2}$ with increasing size (mass) of the particle (the disperseness of the powder), but also increase with increasing real contact area of the particles as $\omega_k \propto S^{1/2}$. Starting with the first harmonic at $\omega_0 \simeq 900$ GHz for a cubic particle with an edge of $d_0 \simeq 6$ A, we can obtain an approximating relation for the dependence of the frequency on the particle size, $\omega \simeq \omega_0 (d_0/d)^{3/2}$. From this relation it follows that for α-Fe particles of dimensions $d \geqslant 100$ nm the oscillation frequency decreases and falls in the ultrasonic range $\omega \leqslant 1$ GHz.

The effect of impact generation of phonons can be used for activation of the dynamic compaction of ultradisperse powders. Indeed, the hypersonic or ultrasonic treatment increases the amplitude of the oscillations. These oscillations of the particles cause a reduction in the effective gap between them, which promotes the formation of intergrain interatomic adhesive bonds. After contact, the bonds are spontaneously strengthened and a strong adhesive contact is formed. This effect is most conspicuous for resonance conditions, where the frequency of the external ultrasonic interaction, ω_s, coincides with the frequency of the induced dynamic oscillations of the particles, $\omega_s = \omega_k$. In the case of non-impact, non-dynamic ultrasonic/hypersonic action, its frequency must coincide with the frequency of normal vibrations of the particles, which depends on their size, $\omega_s = \omega_n(d)$.

This sort of effect can occur also for electromagnetic irradiation. Taking into account the ability of dielectric materials to scatter and absorb electromagnetic radiation, we propose that at the instant of impact the compressed powder is a time-dependent dissipative structure, which is capable of resonant absorption in the infrared or the microwave range. The resonance frequency ω_e is dictated by the Mandel'shtam-Brillouin relation $\omega_e = \omega_k c'/2v_s \sin(\theta/2)$, where c' and v_s are the speed of light and the speed of sound, respectively, and θ is the scattering angle. As Townes and others have shown,[12] stimulated Mandel'shtam-Brillouin scattering and coherent generation of hypersonic waves is possible because of electrostriction. Therefore, selective laser or magnetron radiation synchronous with the impact action is able to amplify the oscillation amplitude of the particles, decrease the effective gap, and ultimately activate the dynamic compaction of the powder. As sources we can use various devices, from gas lasers for nanoparticles of dimensions $\propto 10$ nm to magnetrons for particles $\propto 1$ μm in size, and rf generators for particles $\propto 1$ mm in size. The practical realization of this principle requires further systematic investigations.

[1] S. S. Batsanov, V. A. Vazyulin, L. I. Kopaneva *et al.*, Fiz. Goreniya Vzryva **27**(4), 139 (1991).
[2] É. É. Lin, S. A. Novikov, V. G. Kuropatkin *et al.*, Fiz. Goreniya Vzryva **31**(5), 136 (1995).
[3] A. R. Thölen, in *Fundamentals of Friction: Macroscopic and Microscopic Processes*, edited by I. L. Singer and H. M. Pollock (Kluwer Academic Publisher, 1992), pp. 95–110.
[4] O. Kolosov and K. Yamanaka, Jpn. J. Appl. Phys. **32**, Part 2, L1095 (1993).
[5] V. F. Anisichkin, Khim. Fiz. **12**(5), 605 (1993).
[6] V. V. Pokropivnyĭ and V. V. Skorokhod, Pis'ma Zh. Tekh. Fiz. **22**(9), 70 (1996) [Tech. Phys. Lett. **22**, 374 (1996)].
[7] V. V. Pokropivnyĭ, Metallofizika **18**(2), 38 (1996).
[8] *Atlas of Time Variations of Natural Processes. Order and Chaos in the Lithosphere and Other Spheres* [in Russian], edited by A. G. Gamburgtsev, S. I. Aleksander, A. S. Belyakov *et al.* (OIFZ, Russian Academy of Sciences, Moscow, 1994).
[9] J. R. Smith, G. Bozzolo, A. Banerjera, and J. Ferrante, Phys. Rev. Lett. **63**, 1269 (1989).
[10] J. S. Nelson, B. W. Dodson, and P. A. Taylor, Phys. Rev. B **45**, 4439 (1992).
[11] L. P. Pethica and A. P. Sutton, J. Vac. Sci. Technol. A **6**, 2490 (1988).
[12] R. Y. Chiao, C. H. Townes, and B. P. Stoicheff, Phys. Rev. Lett. **12**, 592 (1964).

Translated by J. R. Anderson

Effects of nonlocality on the dynamics of streamers in positive corona discharges

G. V. Naĭdis

Joint High-Temperature Institute, Moscow

(Submitted March 13, 1997)
Pis'ma Zh. Tekh. Fiz. **23**, 89–94 (June 26, 1997)

Computer simulation is used to study the effect on the parameters of the streamer plasma due to the nonlocality of the electron energy distribution near the head of a streamer in air. Taking into account the nonlocality increases the electron field strength in the head and the electron density in the channel. The streamer radius decreases, while the streamer velocity and current as well as the efficiency of generating chemically active particles remain essentially the same as in the local approach. *© 1997 American Institute of Physics.* [S1063-7850(97)03106-6]

The development of high-pressure gas discharges frequently is accompanied by the formation of ionization waves in the form of thin plasma channels — streamers. Numerical methods have been widely used to study the dynamics of these streamers. In the simulations, the transport of charged particles is generally analyzed in the diffusion approximation, with the use of a local relation between the kinetic coefficients and the reduced field E/n. Since the electric field in the region of the ionization front (the head of the streamer) changes rapidly in space and time during the propagation of the streamer, it is of interest to take into account nonlocal effects. They can be taken into account most correctly by use of the Monte Carlo method. However, this approach requires large amounts of computing time, which greatly limits the possibilities of its utility. The Monte Carlo method has been used[1,2] to study the dynamics of streamer formation in a strong uniform field (in the plane-parallel gap), and in Ref. 3 this method was used in analyzing the structure of a streamer front in a quasi-two-dimensional model (with a fixed streamer radius). The results were compared with the calculations in the diffusion-drift approximation and also with the results of a hydrodynamic approximation. The latter includes the transport equations for the electron density and also their average velocity and energy in the approximation where the kinetic coefficients are determined by the average electron energy. This approach is justified only for a fairly high degree of ionization of the gas, where the frequent electron–electron collisions establish the Maxwellian electron energy distribution. For a slightly ionized plasma, in particular, under typical conditions of a streamer discharge, it is more correct to use the approximation[4,5] based on taking into account the corrections to the electron energy distribution, proportional to the space and time derivatives of the reduced electric field and electron density. This approximation is used in the present work in the simulation of streamer propagation in a positive corona discharge in an air atmosphere.

The model of streamer propagation in the gap between a spherical anode and a planar cathode along the symmetry axis (passing through the center of the sphere perpendicular to the plane) is similar to the model used previously.[6–8] It includes the Poisson equation for the electric potential

$$\mathbf{E}=-\nabla U, \quad \nabla^2 U=-4\pi\rho, \tag{1}$$

where $\rho=e(n_p-n_n-n_e)$ is the volume charge density (n_p, n_n, and n_e are the densities of positive and negative ions and of electrons), and the transport equation for the charged particle density

$$\partial n_j/\partial t+\nabla\cdot(n_j\mathbf{V}_j)=F_j+S_j, \quad \mathbf{V}_j=\mu_j\mathbf{E}-D_j\nabla\ln(n_j). \tag{2}$$

Here μ_j and D_j are the mobility and the diffusion coefficient of particles of species j, the terms F_j correspond to the sums of the contributions of local kinetic processes of the formation and loss of particles (ionization, attachment, electron and ion–ion recombination), and the terms S_j describe the formation of bare charged particles ahead of the streamer front through bulk photoionization.

Unlike the previous model[6–8] in which the rate constants of the processes entering into F_j were taken to correspond to the local values of the electric field, in the present analysis in calculating the ionization rate constants (depending very strongly on the form of the electron energy distribution function) we used the expression[4,5]

$$K_iK_{i0}=1+k_1\mathbf{e}\cdot\nabla\ln n_e+k_2\frac{n}{E}\nabla\cdot(\mathbf{E}/n)+k_3\mathbf{e}\cdot\nabla\ln(E/n)+k_4\frac{\partial\ln(E/n)}{\partial t}, \tag{3}$$

where the ionization rate constants K_{i0} correspond to steady-state uniform conditions, and $\mathbf{e}=\mathbf{E}/E$. The coefficients k_1–k_4, which depend on E/n, were calculated in Refs. 4 and 5 for a nitrogen plasma. Expressions similar to (3) also describe the corrections to the rate constants for the excitation of electron states and dissociation. According to the calculations of Refs. 4 and 5, the coefficients k_1–k_4 for the processes with high thresholds are close to the ionization coefficients. This circumstance, as well as the proximity of the electron energy distribution function in air and in nitrogen (for values of E/n characteristic of streamer propagation) makes it possible to use the coefficients calculated for nitrogen for simulation of a streamer in air. It might be remarked that taking into account nonlocality according to expression (3) does not greatly complicate the calculational scheme used previously[6–8] for the local model.

1063-7850/97/060493-02$10.00

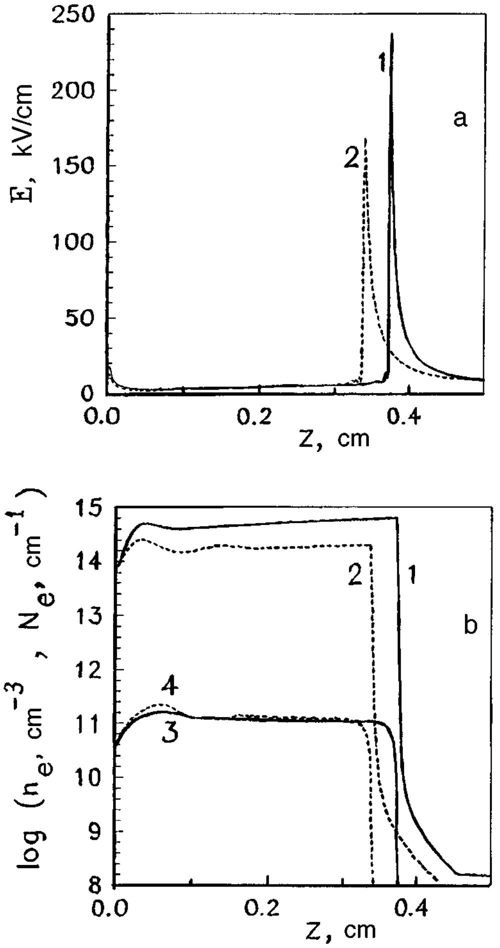

FIG. 1. Electric field distribution and electron density on the streamer axis; a — Electric field E: *1* — with, and *2* — without allowance for nonlocality; b — volume electron density n_e (*1, 2*) and linear electron density N_e (*3, 4*); *1, 3* — with, and *2, 4* — without nonlocality.

In Fig. 1 we present the distribution of the plasma parameters on the streamer axis (calculated with and without the correction (3) for nonlocality), corresponding to the anode radius $R_{sp}=0.05$ cm, an electrode spacing $d=0.5$ cm, and an applied voltage $U=6$ kV for the time $t=5.6$ ns after the start of the streamer. It can be seen that the field E at the streamer head and the electron density n_e in the channel, calculated with allowance for nonlocality, lie above the corresponding values calculated in the local approximation. However, the linear electron density N_e (the integral of the density over the cross section of the streamer) in which nonlocality is taken into account is nearly unchanged compared to the results of the local approach. This means that when nonlocality is included, the characteristic streamer radius decreases (the decrease can be estimated, for example, as $(N_e/\pi n_e)^{1/2}$). The decrease in the streamer radius is also indicated by a comparison (Fig. 2) between the radial distributions of the electric field (for the conditions of Fig. 1) over the cross section of the streamer channel, $z=0.2$ cm, obtained with and without allowance for nonlocality.

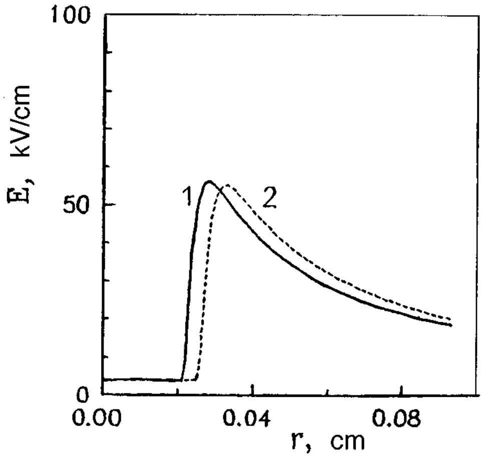

FIG. 2. Electric field distribution over the streamer radius: *1* — with, and *2* — without nonlocality.

The streamer velocity, as shown in Fig. 1, is somewhat higher when the nonlocal corrections are used (as in Ref. 2, where the authors pointed out the small increase in the streamer velocity calculated by the Monte Carlo method as compared with the results of the local approach). The change in the streamer current due to nonlocality is small. In addition, the energy cost[9] of producing the chemically active particles, nitrogen and oxygen, is scarcely different from that calculated in the nonlocal approach. Hence, one can calculate with practical accuracy the main characteristics of a streamer of applied interest within the framework of the local approach.

This work was performed with the support of the Russian Fund for Fundamental Research (Grant No. 96-02-16801) and INTAS (Grant 94-4207).

[1] E. E. Kunhardt and Y. Tzeng, Phys. Rev. A **38**, 1410 (1988).
[2] J. Guo and C. Wu, IEEE Trans. Plasma Sci. **PS-21**, 684 (1993).
[3] V. A. Shveĭgert, Teplofiz. Vys. Temp. **29**, 227 (1991).
[4] N. L. Aleksandrov, N. A. Dyatko, and I. V. Kochetov, Fiz. Plazmy **21**, 806 (1995) [Plasma Phys. Rep. **21**, 763 (1995)].
[5] N. L. Aleksandrov and I. V. Kochetov, J. Phys. D **29**, 1476 (1996).
[6] G. V. Naĭdis, Zh. Éksp. Teor. Fiz. **109**, 1288 (1996) [JETP **82**, 694 (1996)].
[7] N. Yu. Babaeva and G. V. Naidis, Phys. Lett. A **215** 187 (1996).
[8] N. Yu. Babaeva and G. V. Naidis, J. Phys. D **29**, 2423 (1996).
[9] G. V. Naidis, *Proceedings of the 13th European Conference on Atomic and Molecular Phenomena and Ionization of Gases*, Poprad, Slovakia, 1996, pp. 127–128.

Translated by J. R. Anderson